

Copyright

by

Nadege Pie

2008

**The Dissertation Committee for Nadege Pie
certifies that this is the approved version of the following dissertation:**

**Mission Design Concepts for Repeat Groundtrack
Orbits and Application to the ICESat Mission**

Committee:

Bob E. Schutz, Supervisor

Srinivas V. Bettadpur

George H. Born

Wallace T. Fowler

David G. Hull

**Mission Design Concepts for Repeat Groundtrack Orbits
and Application to the ICESat Mission**

by

Nadege Pie, Diplôme d'Ingénieur, M.S.

Dissertation

Presented to the Faculty of the Graduate School of

The University of Texas at Austin

in Partial Fulfillment

of the Requirements

for the Degree of

Doctor of Philosophy

The University of Texas at Austin

December 2008

A ma Maman,
pour ses sacrifices, sa patience,
sa confiance et son amour ...

Acknowledgements

I want to thank Dr. Bob E. Schutz for taking me under his wing exactly six years ago when I stepped into his office in search of an advisor. I have learned so much under his supervision, as a scientist but also as a person, that I know these six years will always stand out as a corner stone in my professional and personal life. I also want to express my deep gratitude to all my committee members for their support and encouragements. I knew I could always count on them when I needed their help, even when I lacked the discernment to ask for it. I also want to thank Charles Webb, Dr. Giacaglia, Dr. Lara and Dr. Klokočník for the invaluable discussions we had. And above all I want to thank my mother Monique, my family, my friends and all those who gave me love and the courage not to give up.

Mission Design Concepts for Repeat Groundtrack Orbits and Application to the ICESat Mission

Nadège Pie, PhD.

The University of Texas at Austin, 2008

Supervisor: Bob E. Schutz

The primary objective of the NASA sponsored ICESat mission is to study the short and long term changes in the ice mass in the Greenland and Antarctica regions. The satellite was therefore placed into a frozen near-polar near-circular repeat groundtrack to ensure an adequate coverage of the polar regions while keeping the groundtrack periodic and reducing the variations in the orbital elements, and more specifically the semi-major axis of the ICESat orbit. After launch, a contingency plan had to be devised to compensate for a laser that dangerously compromised the lifetime of the ICESat mission. This new plan makes an intensive use of the ICESat subcycles, a characteristic of the repeat groundtrack orbits often over-looked. The subcycle of a repeat groundtrack orbit provide global coverage within a time shorter than the groundtrack repetition period. For a satellite with an off-nadir pointing capacity, the subcycles provide near-repeat tracks

which represents added opportunity for altimetry measurement over a specific track. The ICESat subcycles were also used in a very innovative fashion to reposition the satellite within its repeat cycle via orbital maneuvers called *phasing maneuver*. The necessary theoretical framework is provided for the subcycle analysis and the implementation of phasing maneuvers for any future repeat orbit mission. In the perspective of performing cross-validation of missions like CryoSat using the ICESat off-nadir capacity, a study was conducted to determine the geolocations of crossovers between two different repeat groundtrack Keplerian orbits. The general analytical solution was applied to ICESat vs. several other repeat groundtrack orbit mission, including the future ICESat-II mission. ICESat's repeat groundtrack orbit was designed using a disturbing force model that includes only the Earth geopotential. Though the third body effect from the Sun and the Moon was neglected in the orbit design, it does in fact disrupt the repeatability condition of the groundtrack and consequently implies orbit correction maneuvers. The perturbations on ICESat orbit due to the third body effect are studied as a preliminary work towards including these forces in the design of the future ICESat-II repeat groundtrack orbit.

Table of Contents

Acknowledgments	v
Abstract	vi
List of Figures	xii
List of Tables	xvii
CHAPTER 1: The ICESat Missions	1
1.1 The first ICESat Mission.....	1
1.1.1 Mission Description.....	1
1.1.2 Orbit Requirements.....	3
1.2 Future ICESat Missions.....	4
1.2.1 Mission Objectives.....	4
1.2.2 Orbit Considerations.....	5
CHAPTER 2: Repeat groundtrack Orbits: Concept and Generation	7
2.1 Background of Repeat Groundtrack Orbit Missions.....	7
2.2 General Characteristics of Repeat Groundtrack Orbits.....	10
2.3 Generation of Repeat Groundtrack Orbits in Full Geopotential.....	12
2.3.1 SADSaM.....	13
2.3.2 Alternate Method.....	16

2.4	ICESat Repeat Groundtrack Orbits.....	21
2.5	Motivation and Outline of Work.....	23
CHAPTER 3: Subcycles.....		26
3.1	Definitions.....	27
3.1.1	Repeat Cycle.....	27
3.1.2	Near-Repeat Groundtracks.....	30
3.1.3	Subcycles.....	34
3.2	Subcycles of the Three ICESat Repeat Orbits.....	38
3.3	Properties of the Chart of Subcycles.....	42
3.3.1	Bounded Distribution.....	42
3.3.2	Symmetrical Distribution.....	43
3.3.3	Linear Distribution.....	44
3.3.4	Subcycle Combination.....	47
3.4	ICESat's Sequence of Subcycles.....	49
3.5	Influence of the Parameter N	51
3.5.1	ICESat-II Repeat Orbit.....	52
3.5.2	The Bezout Theorem.....	55
CHAPTER 4: Phasing.....		60
4.1	Definitions.....	61
4.1.1	Transition Orbit.....	62
4.1.2	Transition Opportunities.....	66

4.2	Number of Transition Opportunities.....	71
4.3	Advantages.....	74
CHAPTER 5: Crossovers.....		80
5.1	Crossover Location Between Two Orbits.....	83
5.1.1	Implicit Function.....	83
5.1.2	Explicit Function.....	87
5.2	Angle Between Tracks.....	92
5.3	Application to ICESat and CryoSat.....	93
5.4	Application to ICESat and ENVISAT.....	101
5.5	Application to ICESat and ICESat-II.....	109
CHAPTER 6: Third Body Perturbations.....		112
6.1	Single-Average Disturbing Function.....	113
6.2	Equations of Motion.....	122
6.3	Application to a Simplified Case.....	127
6.4	Double-Average Disturbing Function.....	138
6.5	Third Body in Inclined Orbital Plane	143
6.6	Application to Repeat Groundtrack Orbits	156
CHAPTER 7: Conclusions.....		160
7.1	Subcycles.....	161
7.2	Phasing.....	161
7.3	Crossovers.....	162

7.4 Third Body Perturbations.....	163
7.5 Future Work.....	164
BIBLIOGRAPHY	165
VITA	168

List of Figures

2.1	Flowchart of SADSam software.....	14
3.1	Close up of the groundtrack pattern at the equator in the case of ICESat’s 8-day repeat orbit.....	31
3.2	Close up of the groundtrack pattern at the equator in the case of ICESat’s 91-day repeat.....	32
3.3	Close up of the groundtrack pattern at the equator in the case of ICESat’s 183-day repeat orbit.....	33
3.4	Spacing pattern of the ascending nodes on the extended equatorial arc.....	36
3.5	Chart of subcycles for the ICESat 8-day repeat orbit with $N = 119$	39
3.6	Chart of subcycles for the ICESat 91-day repeat orbit with $N = 1354$	40
3.7	Chart of subcycles for the ICESat 183-day repeat orbit with $N = 2723$	41
3.8	Close-up of Figure (3.6). Linearity.....	44
3.9	Close-up of Figure (3.7). Linearity.....	45
3.10	Three-dimensional representation of the chart of subcycles for ICESat’s 91-day repeat orbit.....	46
3.11	Close-up of Figure (3.6). Combination of the 7-day subcycle and the 17-day subcycle.....	47
3.12	Combination of the 21-day subcycle and the 31-day subcycle.....	48
3.13	Close-up of Figure (3.6). Sequence of subcycles 33-25-33.....	50
3.14	Chart of subcycles for a 91-day repeat orbit with $N = 1353$	53
3.15	Chart of subcycles for a 91-day repeat orbit with $N = 1355$	54

3.16	Chart of subcycles for a future ICESat-II mission with $N = 1376$	58
3.17	Chart of subcycles for a future ICESat-II mission with $N = 1367$	59
4.1	Resonance map for 1-day to 91-day repeat orbits with a <i>sma</i> comparable to ICESat 91-day repeat orbit semi-major axis.....	64
4.2	Resonance map for 1-day to 91-day repeat orbits with redundant orbits.....	65
4.3	Longitudes of the 91-day orbit's ascending nodes compared to the longitudes of the 8-day repeat orbit's ascending nodes.....	68
4.4	Correspondence of the transition opportunities between the 8-day and the 91-day repeat orbits.....	70
4.5	Longitudes of the 91-day orbit's ascending nodes compared to the longitudes of the 9-day repeat orbit's ascending nodes.....	71
4.6	Longitudes of the 91-day orbit's ascending nodes compared to the longitudes of the 25-day repeat orbit's ascending nodes.....	72
4.7	Longitudes of the 91-day orbit's ascending nodes compared to the longitudes of the 58-day repeat orbit's ascending nodes.....	73
4.8	Fuel cost for a direct maneuver and a phasing maneuver between the 91-day repeat orbit and the 8-day repeat orbit.....	77
4.9	Fuel cost comparison between a direct maneuver and a phasing maneuver....	78
5.1	3-dimensional plot giving the latitude at the crossover as a function of the difference of the equatorial crossings' longitudes and the angle between the tracks at the crossover.....	95
5.2	Off-nadir pointing.....	96
5.3	ICESat vs. CryoSat case. Selecting a solution for an altitude of 70°N and an angle between tracks less than 17.6°.....	98
5.4	Projections of Figure (5.3).....	99
5.5	Crossover between ICESat and CryoSat tracks over Greenland at latitude 70°N.....	100
5.6	Close-up of ICESat and CryoSat crossover at latitude 70°N.....	101

5.7	ICESat vs ENVISAT case. Selecting a solution for an altitude of 70°N and an angle between tracks less than 17.6°.....	104
5.8	Projections of Figure (5.7).....	105
5.9	Locations of crossovers between ICESat and ENVISAT tracks at latitude 70°N.....	106
5.10	Close-up of Figure (5.9) over the Greenland region for ICESat and ENVISAT crossovers.....	108
5.11	3-dimensional plot for ICESat vs. ICESat-II.....	109
5.12	Projections of Figure (5.11).....	111
6.1	Perturbations of ICESat eccentricity vector due to the Sun over 365 days with a disturbing function expanded to the 2 nd degree.....	130
6.2	Perturbations of ICESat inclination due to the Sun over 365 days with a disturbing function expanded to the 2 nd degree.....	130
6.3	Perturbations of ICESat line of node due to the Sun over 365 days with a disturbing function expanded to the 2 nd degree.....	131
6.4	Perturbations of ICESat eccentricity vector due to the Sun over 365 days: comparison between the 4 th degree and 2 nd degree.....	131
6.5	Perturbations of ICESat inclination due to the Sun over 365 days: comparison between the 4 th degree and 2 nd degree.....	132
6.6	Perturbations of ICESat line of node due to the Sun over 365 days: comparison between the 4 th degree and 2 nd degree.....	132
6.7	Perturbations of ICESat eccentricity vector due to the Moon over 28 days with a disturbing function expanded to the 2 nd degree.....	135
6.8	Perturbations of ICESat inclination due to the Moon over 28 days with a disturbing function expanded to the 2 nd degree.....	135
6.9	Perturbations of ICESat line of node due to the Moon over 28 days with a disturbing function expanded to the 2 nd degree.....	136
6.10	Perturbations of ICESat eccentricity vector due to the Moon over 28 days: comparison between the 4 th degree and 2 nd degree.....	136

6.11	Perturbations of ICESat inclination due to the Moon over 28 days : comparison between the 4 th degree and 2 nd degree.....	137
6.12	Perturbations of ICESat line of node due to the Moon over 28 days : comparison between the 4 th degree and 2 nd degree.....	137
6.13	ICESat eccentricity vector due to the Sun over 21552 years in the hypothetical case of the Sun in the equatorial plane.....	140
6.14	ICESat inclination due to the Sun over 21552 years in the hypothetical case of the Sun in the equatorial plane.....	140
6.15	ICESat line of node due to the Sun over 21552 years in the hypothetical case of the Sun in the equatorial plane.....	141
6.16	ICESat eccentricity vector due to the Moon over 10091 years in the hypothetical case of the Moon in the equatorial plane.....	141
6.17	ICESat inclination due to the Moon over 10091 years in the hypothetical case of the Moon in the equatorial plane.....	142
6.18	ICESat line of node due to the Moon over 10091 years in the hypothetical case of the Moon in the equatorial plane.....	142
6.19	ICESat eccentricity vector due to the Sun over 21552 years with the Sun in the ecliptic plane.....	145
6.20	ICESat inclination due to the Sun over 21552 years with the Sun in the ecliptic plane.....	145
6.21	ICESat line of node due to the Sun over 21552 years with the Sun in the ecliptic plane.....	146
6.22	ICESat eccentricity vector due to the Moon over 10091 years with the Moon in the ecliptic plane.....	146
6.23	ICESat inclination due to the Moon over 10091 years with the Moon in the ecliptic plane.....	147
6.24	ICESat line of node due to the Moon over 10091 years with the Moon in the ecliptic plane.....	147
6.25	Perturbations of ICESat eccentricity vector due to the Sun over 365 days with the Sun in the ecliptic plane.....	150

6.26	Perturbations of ICESat eccentricity vector due to the Sun over 5 years with the Sun in the ecliptic plane: comparison between single- and double-average.....	150
6.27	Perturbations of ICESat inclination due to the Sun over 365 days with the Sun in the ecliptic plane.....	151
6.28	Perturbations of ICESat inclination due to the Sun over 5 years with the Sun in the ecliptic plane: comparison between single- and double-average.....	151
6.29	Perturbations of ICESat line of node due to the Sun over 365 days with the Sun in the ecliptic plane.....	152
6.30	Perturbations of ICESat line of node due to the Sun over 5 years with the Sun in the ecliptic plane: comparison between single- and double-average....	152
6.31	Perturbations of ICESat eccentricity vector due to the Moon over 28 days with the Moon in the ecliptic plane.....	153
6.32	Perturbations of ICESat eccentricity vector due to the Moon over 365 days with the Moon in the ecliptic plane: comparison between single- and double-average.....	153
6.33	Perturbations of ICESat inclination due to the Moon over 28 days with the Moon in the ecliptic plane.....	154
6.34	Perturbations of ICESat inclination due to the Moon over 365 days with the Moon in the ecliptic plane: comparison between single- and double-average.	154
6.35	Perturbations of ICESat line of node due to the Sun over 28 days with the Sun in the ecliptic plane.....	155
6.36	Perturbations of ICESat line of node due to the Moon over 365 days with the Moon in the ecliptic plane: comparison between single- and double-average.....	155

List of Tables

2.1	Main characteristics of ICESat's repeat orbits.....	23
3.1	Spacing between time-consecutive and space-consecutive ascending nodes..	29
3.2	Solutions of the Bezout equation for the ICESat-II 91-day repeat orbit.....	56
4.1	Transition opportunities between the 8 day and the 91-day repeat orbits.....	69
5.1	Characteristics of ICESat and CryoSat orbits.....	94
5.2	Summary of the parameters for the off-nadir maneuver over Greenland at latitude 70°N.....	100
5.3	Characteristics of ICESat and ENVISAT orbits.....	102
5.4	Detailed information of the crossovers between ICESat and ENVISAT occurring over the Greenland region.....	107
6.1	Initial conditions for the propagation of ICESat's orbital elements in the simplified case of the third in the equatorial plane.....	128
6.2	Initial conditions for the propagation of ICESat's orbital elements in the case of the third in an inclined plane.....	149

CHAPTER 1

THE ICESAT MISSIONS

1.1 THE FIRST ICESAT MISSION

1.1.1 MISSION DESCRIPTION

NASA's Ice Cloud and land Elevation Satellite was launched on January 12, 2003 on a Boeing Delta-2 rocket from Vandenberg Air Force Base in California. ICESat's primary objective is to determine the seasonal and long-term changes of the ice mass in the polar regions, more specifically in the Greenland and Antarctica regions. The ice mass contained at the poles is equivalent to a 65 m rise of the global sea level. Each year, the Earth's ice sheets exchange with the oceans a volume of water equivalent to 8 mm of global sea level. This exchange is the main contribution to the global sea level changes. The other two contributions come from the melting of land glaciers around the world and the thermal expansion of the oceans. Though these contributions shouldn't be ignored, they remain marginal compared to the polar ice sheets contribution. It has been shown that the ice sheets react much faster to the environmental and climate changes than

initially thought. However, the complexity of the dynamic of the ice mass changes and distribution makes it difficult to generate accurate projections. It is therefore critical to get a better understanding of the dynamics behind the interaction between the oceans and the polar ice sheets. By observing the seasonal and long-term changes of the ice sheets mass, ICESat provides valuable clues toward a better understanding of their change as well as the contribution to the global sea level.

Other applications include land topography, cloud heights and vertical distribution, as well as atmospheric aerosol distribution. ICESat's measurements of the vegetation canopy heights were also used to map the distribution of the biomass above ground but with an accuracy lower than required by the ecosystem science community.

The precise measurements are obtained using the Geoscience Laser Altimeter System (GLAS). GLAS comprises three identical lasers used successively throughout the mission lifetime. The lasers pulse at two wavelengths: the near infrared channel is used for altimetry and thick cloud height measurements; the channel in the green spectrum is used for aerosol and more sensitive measurements of cloud distribution. The lasers were designed with a laser spot size of 70 m in diameter and a Pulse Repetition Frequency (PRF) of 40 Hz, which translates into a distance of 170 m between consecutive spots at ICESat's altitude. The satellite off-nadir pointing capacity allows the laser to point at targets off the nominal groundtrack (up to 5°). For example, the off-pointing capacity has been successfully used to monitor the elevation of land elevation on specific sites that are not located along ICESat's ground track, like the volcanic dome growth of Mt. Saint

Helens (Washington State). The off-nadir pointing is also used to compensate the orbit drift while pointing at the reference groundtrack.

1.1.2 ORBIT REQUIREMENTS

The ICESat satellite was launched in a low Earth orbit, at an altitude of approximately 600 km. Due to the nature of the mission, it was important that the orbit allowed for an optimum observation of the polar ice sheets. An inclination of 90° would guarantee a complete coverage at the pole. However, such an inclination does not provide a dense distribution of crossovers, or groundtrack intersections, which is an important method of analyzing the measurements for surface change. Another constraint for the choice of the inclination was to ensure the coverage of the major ice streams in the West Antarctica Ice Sheet which extend to 86° South. With an inclination of 94° , ICESat's groundtrack provides a global coverage between the latitudes 86° South and 86° North. The narrow regions at the poles not covered by the groundtrack can be mapped using airborne laser altimetry.

Because the ICESat mission is above all a laser altimetry mission, a very accurate knowledge of the satellite position is mandatory. This knowledge is rendered easier with the use of a near-circular frozen orbit. Indeed, a frozen orbit limits the variations of the orbital elements in the average sense. The argument of perigee of the ICESat orbit is set to 90° in average and does not circulate. The frozen eccentricity is then equal to 0.0013 in average.

Finally, to be able to observe the evolution of the ice mass and make comparisons between measurements taken at different times it is required to fly over the same geolocations. The crossovers provide the opportunity to compare measurement. However for the density and accuracy of the information desired, it is necessary for the satellite to be put in a repeat groundtrack orbit. Only with a repeat groundtrack orbit are along-track measurements comparisons possible throughout the entire mission lifetime. When in a repeat groundtrack orbit, the time between two consecutive measurements over the same site depends on the value of the semi-major axis. Three different repeat groundtrack orbits were designed for the ICESat mission (only one is used for the operation mode). To these three orbits correspond three different altitudes, all in the vicinity of 600 km.

1.2 FUTURE ICESAT MISSIONS

1.2.1 MISSION OBJECTIVES

ICESat-II is scheduled for launch in 2015 as the ICESat follow-on mission. It has been identified as a top-priority mission by NASA's New Decadal Survey issued in January 2007. The main purpose of the mission will therefore be similar to the ones of ICESat while providing additional and improved information. The mission objectives fall under five main directions: ice sheets, sea ice, vegetation, solid earth/hydrology and atmosphere:

- The ice sheets study should improve the predictive capabilities of the ice sheets and glaciers numerical model while determining the contribution of the ice sheets to the sea level rise.

- The changes in thickness of sea ice are still not well understood. Combining laser altimetry and radar altimetry would greatly benefit the measurement of sea ice thickness.
- By reducing the size of the laser footprint to a diameter less than 25 m, the error on the vegetation height would be greatly reduced which, in turn, would improve the estimation of the global distribution of the carbon stored in the above-ground biomass.
- Better agility and pointing accuracy should enable the satellite to observe land elevation changes due to natural hazard like volcano eruptions or tectonic activity. For hydrology, a smaller footprint and a higher frequency of the pulse repetition would improve the information on the water level in smaller rivers.
- The goal for the atmospheric study is to continue the observation of the cloud and aerosol distribution, especially at high altitudes, as the ICESat, CloudSat and CALYPSO missions are approaching the end of their lifetime.

1.2.2 ORBIT CONSIDERATIONS

At the time this dissertation is being written, the operation and calibration orbits for the ICESat-II mission have not been decided yet. The successes and the lessons learned during the first ICESat mission provided, and still provide, a valuable heritage on which to build the follow-on mission. To take full advantage of this heritage it was suggested that the ICESat-II orbit should be identical to the one of the first ICESat (with the exception of the line of node that should be adjusted in order to obtain the exact same

groundtrack as the ICESat groundtrack). However, it was also suggested at some point that the orbit be at a lower altitude, around 500 km instead of 600 km. It was also suggested that the new orbit should provide a denser spacing for the DEM mapping. This would translate into a longer repeat groundtrack orbit and consequently a different semi-major axis. Other changes in terms of orbital period have also been proposed but the currently preferred strategy would be to keep the same identical orbit as the first ICESat mission. Nevertheless, different orbits that have been suggested for ICESat-II will be analyzed in this study.

CHAPTER 2

REPEAT GROUNDTRACK ORBITS: CONCEPT AND GENERATION

2.1 BACKGROUND OF REPEAT GROUNDTRACK ORBIT MISSIONS

Satellite missions devoted to the observation of the Earth and its climate, as well as constellations of navigation satellites, commonly use repeat groundtrack orbits. In the case of Earth observation, the repeat groundtrack configuration is particularly useful as it allows a satellite to fly over the same site at the surface of the Earth after some interval of time. The periodicity of the groundtrack enables comparison measurements at specific observation sites for calibration or validation purposes, as well as the monitoring of the evolution of climatic and geologic phenomenon. Repeat groundtrack orbits were used as early as 1978 with the launch of the first Block-I GPS satellite. That same year, the satellite SeaSat was launched and put into a 17-day repeat groundtrack orbit. The mission ended prematurely after a massive short circuit in the solar array drive assembly. The GeoSat mission was then designed to complete the geoid mapping started with SeaSat. The GeoSat satellite was launched in 1985 into a SeaSat-similar orbit. In 1998, GFO

(GeoSat Follow-On) succeeded to GeoSat and the 17-day repeat groundtrack orbit was retained. The European Remote Sensing satellites (ERS-1 and ERS-2) were launched in 1991 and 1995 and put into comparable 35-day repeat groundtrack orbit, with different right ascension of the ascending node. From 1995 to 1996 (end of the ERS-1 mission), the two satellites operated in tandem mode, with ERS-2 flying over the same groundtrack as ERS-1, but 24 hours after ERS-1. In 1992, the satellite Topex/Poseidon was launched in 1992 as a joint effort from CNES and NASA. Its successor, Jason-1, was launched in 2001 (Jason-2 is scheduled for launch mid-2008). Both satellites were put in a 10-days repeat groundtrack orbit. In 2002, ESA launched the satellite ENVISAT into a 35-day repeat orbit using the same repeat pattern as the one established for ERS-1 and ERS-2. The ICESat (Ice, Cloud and land Elevation Satellite) was launched in 2003. Like all the missions previously mentioned, the main objective of the ICESat mission is Earth observation. More specifically, the mission goals are to measure the ice sheet mass evolution, cloud and aerosol heights, land topography and vegetation. The primary ICESat science objectives are addressed with a 91-day frozen repeat groundtrack orbit designed with a near-polar inclination of 94° in order to provide coverage of the polar ice sheets while respecting other mission requirements. Moreover, ICESat has used an 8-day repeat groundtrack orbit to support calibration activities.

Repeat groundtrack orbits (which we will simply call *repeat orbits* from now on), frozen and non-frozen, have been extensively studied. A frozen orbit is an orbit for which the secular drift and the long-periodic oscillations of both the eccentricity and the argument of perigee are nullified. Therefore, with such an orbit, the altitude variations

can be described as a function of the latitude. Frozen orbits in the zonal problem, their stability and their classification into families have been the subject of studies (Rosborough and Ocampo, 1991), (Coffey, 1994) that form the basis of frozen repeat orbit dynamics. Repeat orbits are periodic in longitude and latitude and are therefore considered to be 2-D periodic in a rotating frame attached to the Earth. An orbit is frozen in the mathematical sense when the orbit is periodic in the orbital plane. The immediate consequence is that the orbit is also frozen in the mean (or averaged) sense, which is the definition most commonly used for frozen orbits. Therefore, a repeat orbit that is frozen in the mathematical sense is 3-D periodic in a rotating frame attached to the Earth. However, the frozen condition does not necessary ensure the periodicity of the groundtrack. General methods have been developed to identify 3-D periodic frozen repeat orbits (Lara, 1999) and 2-D periodic frozen repeat orbits (Lim, 1995), as well as polar repeat orbits (Lara, 1997). The problem of the 3-D periodicity has also been studied through an orbit maintenance approach. This work has been achieved by Rim et al. (2000) where the perturbed repeat orbit for a proposed LightSAR mission is maintained within a 125m diameter tube about the reference orbit. The perturbing forces model used by Rim include the Joint Gravity Model 3 with geopotential harmonics up to degree 70 and order 70 (JGM3 70×70), luni-solar effect, drag and radiation pressure. More specific studies have been conducted to analyze practical cases and missions. Uphoff et al. (1992) investigated the RadarSat sun-synchronous frozen repeat orbit and its groundtrack stability. Mission design work done by Lim and Schutz (1996) for the ICESat mission

provided numerical tools to design frozen orbits with exact repeat groundtracks in the Joint Gravity Model 3 with zonal harmonics up to degree 31 (JGM3 31×0).

2.2 GENERAL CHARACTERISTICS OF REPEAT GROUNDTRACK ORBITS

We consider an intersection of a satellite's ascending groundtrack and the equator. We label AN_1 the longitude corresponding to the intersection site, also known as an ascending node. After one orbital period, T_{sat} , the nadir trace of the satellite crosses the equator a second time in the ascending direction. The longitude of this second intersection is labeled AN_2 . Without the Earth rotation, or if the satellite's orbit plane was fixed in an Earth centered fixed frame, the two equatorial crossings would occur over the same site and we would have $AN_1 = AN_2$. Since neither the Earth rotation nor the precession of the orbital plane can be neglected, the longitude difference between the two ascending nodes, or longitude shift, is determined by

$$\Delta\lambda = AN_2 - AN_1 = \omega'_{\oplus} T_{sat} \quad (2.1)$$

where $\omega'_{\oplus} = \omega_{\oplus} - \dot{\Omega}$ is the Earth rotation rate relative to the satellite's orbit plane. The term ω_{\oplus} represents the Earth rotation rate in the inertial frame and $\dot{\Omega}$ represents the rotation rate of the satellite's line of node. Since the Earth is rotating eastward and $\omega_{\oplus} > \dot{\Omega}$ for a Low Earth Orbit (LEO), an equatorial crossing will be located west of the previous crossing in the case of a LEO.

The term ω'_{\oplus} allows introducing a new definition of a day. We already can differentiate several definition of a day. For example, a sidereal day is defined as the time required for the Earth to complete one revolution with respect to the axes of an Earth Centered Inertial frame (ECI). A solar day corresponds to the time required for the Earth to complete one revolution with respect to the rotating Sun-Earth line. Using the relative rotation rate of the Earth with respect to the satellite's orbit plane ω'_{\oplus} , we can define a nodal day, also called nodal period of Greenwich (Vallado, 1997), T_{GW} . One nodal day corresponds to the time the Earth takes to complete one revolution with respect to the orbit plane. The notion of nodal day is therefore 'orbit-dependent' and is computed as follows:

$$T_{GW} = \frac{2\pi}{\omega'_{\oplus}} = \frac{2\pi}{\omega_{\oplus} - \dot{\Omega}} \quad (2.2)$$

A repeat groundtrack orbit is a two dimensional periodic orbit in a rotating frame attached to the Earth. Indeed, if we consider the orbit in the spherical coordinates of the rotating Earth Centered Earth Fixed frame (ECEF) defined by the triplet (ρ, λ, φ) , respectively radius, longitude and latitude, the periodicity of λ and φ suffices to ensure the periodicity of the groundtrack. The periodicity of the groundtrack, that is the groundtrack retraces itself exactly after a certain time, is achieved when the nodal period of the satellite and the nodal period of Greenwich are commensurate. This translates into the following synchronicity equation:

$$D \cdot T_{GW} = N \cdot T_{sat} \quad (2.3)$$

where D and N are integers relatively prime. T_{sat} is the ‘node-to-node’ period of the satellite. In the absence of perturbations, the nodal period is equal to the Keplerian period. However, in a perturbed model, it is necessary to take into account the rotation rate of the perigee of the satellite. Recombining Eq.(2.2) and Eq.(2.3) leads to the following constraint to design a repeat orbit:

$$D \cdot \frac{2\pi}{\omega_{\oplus} - \dot{\Omega}} = N \cdot \frac{2\pi}{\dot{M} + \dot{\omega}} \quad (2.4)$$

where $\dot{M} + \dot{\omega}$ is the rate of the mean argument of latitude, \dot{M} is the satellite’s mean motion and $\dot{\omega}$ the rate of its argument of perigee. Eq. (2.4) establishes the synchronicity between the Earth rotation and the satellite rotation. The satellite completes N nodal revolutions while the Earth performs D rotations with respect to the satellite’s orbital plane. In other words, the satellite completes N nodal revolutions in D nodal days.

2.3 GENERATION OF REPEAT ORBITS IN FULL GEOPOTENTIAL

Looking at Eq. (2.4), it is obvious that the design of a repeat orbit will depend on the perturbing forces included in the calculation of the time rate of the satellite orbital elements. The gravitational potential of the Earth, or geopotential, is by far the main disturbing force to consider when trying satisfying the synchronicity condition of Eq. (2.4). The geopotential can be accounted for to a high degree and order of the

gravitational potential. The higher terms of the gravitational potential expansion becomes more relevant as the duration of the repeat orbit to be designed gets longer, i.e. the value of D gets greater. Several approaches can be chosen to obtain a precise reference repeat orbital in the full geopotential. We review two different methods: the first one developed by Martin Lara which leads to frozen repeat orbits that are 3-D periodic using a full zonal potential; a second method was developed by Samsung Lim and applied at the Center for Space Research (CSR) to design the ICESat mission's various repeat orbits. Those orbits are frozen (2-D periodic) in the full geopotential, including the zonal, sectoral and tesseral terms.

2.3.1 SADSaM

The Software Assistant for Designing Satellite Missions (SADSaM) was developed by Martin Lara for the Real Instituto y Observatorio de la Armada. Unlike most of the procedures used by aerospace engineers that consist in an iterative trial and error based on the refinement of the eccentricity and the semi-major axis, SADSaM searches for the periodic solutions of the zonal gravitational problem, that is to say orbits that are 3-D periodic in the ECEF frame. These orbits naturally repeat their groundtrack exactly and can therefore be used as reference orbits for missions requiring repeat groundtrack orbits. Fig. (2.1) is a reproduction of the flowchart of the SADSaM algorithm as given in the SADSaM user's manual (Lara, 1999).

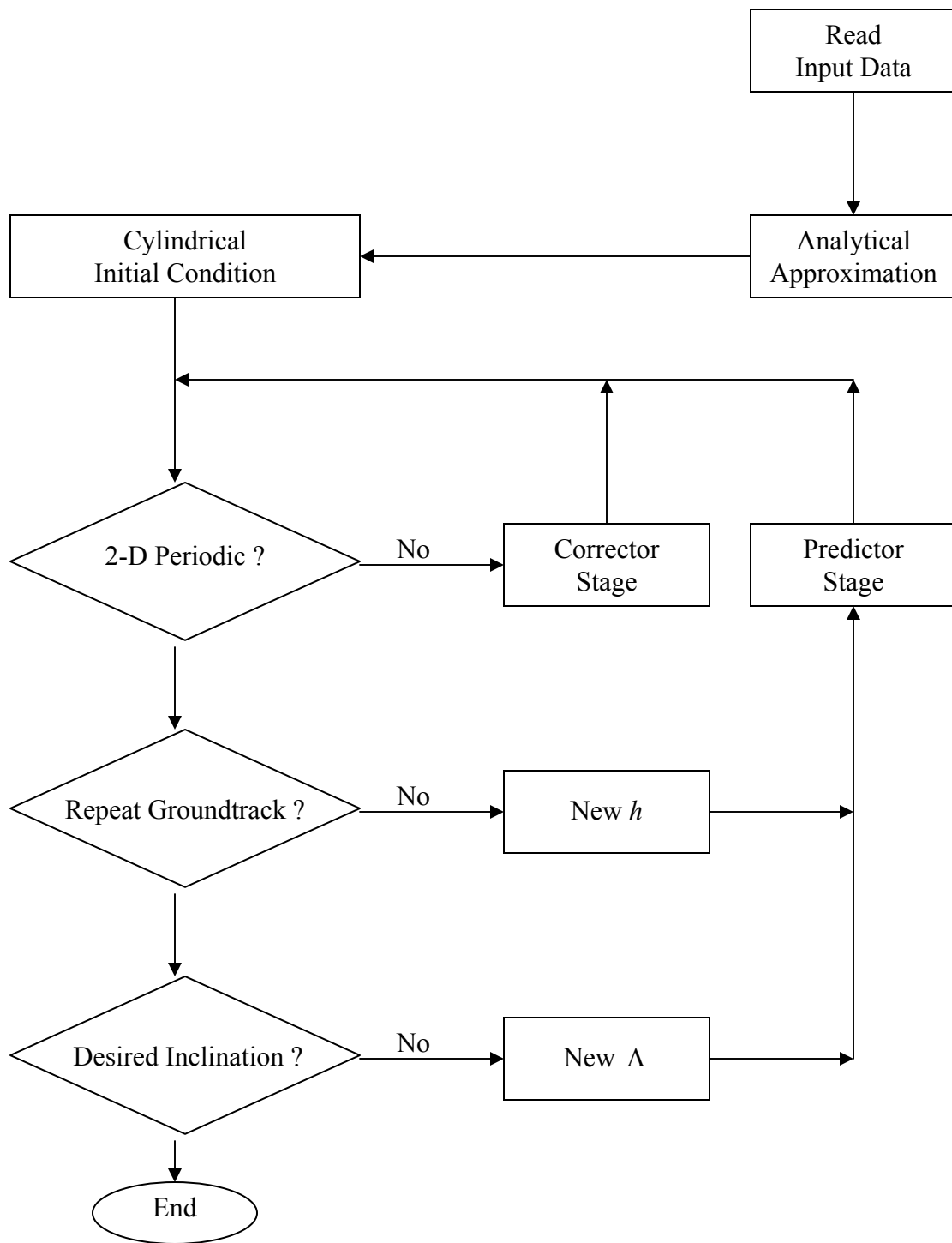


Figure 2.1: Flowchart of SADSaM software to compute repeat groundtrack frozen orbits. (taken from SADSaM handbook – Martín Lara – CNES)

Starting with the value of D , N and i (respectively the number of nodal days, the number and the inclination of satellite revolution of the repeat orbit), a first analytical approximation is computed. In the computation, only the J_2 term of the zonal potential expansion is used in the expression of the time rates of the orbital elements appearing in Eq. (2.4), which are given by the Lagrangian Planetary Equations (LPE).

$$\dot{\Omega} = -\sqrt{\frac{\mu}{a^3}} \left(\frac{a_{\oplus}}{a}\right)^2 \frac{3J_2}{2(1-e^2)^2} \cos i \quad (2.5)$$

$$\dot{\omega} = -\sqrt{\frac{\mu}{a^3}} \left(\frac{a_{\oplus}}{a}\right)^2 \frac{3J_2}{2(1-e^2)^2} \left(\frac{5}{2} \sin^2 i - 2\right) \quad (2.6)$$

$$\dot{M} = -\sqrt{\frac{\mu}{a^3}} \left[1 - \left(\frac{a_{\oplus}}{a}\right)^2 \frac{3J_2}{2(1-e^2)^{3/2}} \left(\frac{3}{2} \sin^2 i - 1\right) \right] \quad (2.7)$$

The approximation obtained is nearly periodic in the full zonal potential. This approximate solution is refined using an iterative procedure aiming at achieving successively:

- The periodicity of the orbit in its orbit plane (2-D periodicity)
- The periodicity of the groundtrack
- The correction of the inclination to match its desired value.

This is done by implementing three interactive steps. The first step achieves the 2-D periodicity of the orbit in the full zonal potential by adjusting the cylindrical coordinates of the satellite at the ascending node. Since the 2-D periodic orbit obtained at the end of

the first step will generally not repeat its groundtrack (nor match the desired value for the eccentricity), a correction is computed in the second step to achieve the periodicity of the groundtrack. The Secant method is used to converge to the desired repeat orbit with a first guess computed using the Newton-Raphson method. The convergence is performed by adjusting the energy h of the orbit until Eq. (2.3) is satisfied. In the third step, the Secant method is used again to converge to the desired value for the inclination. This is done indirectly using the polar component of the orbit's angular momentum:

$$\Lambda = -\sqrt{\mu a(1 - e^2)} \cos i \quad (2.8)$$

2.3.2 ALTERNATE METHOD

The procedure proposed by Lara for the generation of frozen repeat groundtrack orbits leads to 3-D periodic orbits in the ECEF frame, i.e. to orbits that are frozen in the mathematical sense in the ECEF frame. Though these orbits are perfect candidates for the design of reference repeat orbits, the only necessary constraints to satisfy are the frozen condition in the mean sense and the synchronicity condition given by Eq. (2.4). Therefore, it suffices to find the set of mean orbital elements that satisfies simultaneously the three following differential equations to design a *good* reference frozen repeat orbit:

$$\dot{e} = 0 \quad (2.9)$$

$$\dot{\omega} = 0 \quad (2.10)$$

$$D \cdot \dot{M} + N \cdot (\dot{\Omega} - \omega_{\oplus}) = 0 \quad (2.11)$$

The time rate of the orbital elements can be expressed using the LPEs, where \bar{U} represents the averaged zonal potential and $n = \sqrt{\mu/a^3}$ is the mean motion of the satellite in the two body problem.

$$\dot{e} = -\frac{\sqrt{1-e^2}}{na^2e} \frac{\partial \bar{U}}{\partial \omega} \quad (2.12)$$

$$\dot{\omega} = \frac{\sqrt{1-e^2}}{na^2e} \frac{\partial \bar{U}}{\partial e} - \frac{\cos i}{na^2\sqrt{1-e^2}\sin i} \frac{\partial \bar{U}}{\partial i} \quad (2.13)$$

$$\dot{M} = n - \frac{2}{na} \frac{\partial \bar{U}}{\partial a} - \frac{1-e^2}{na^2e} \frac{\partial \bar{U}}{\partial e} \quad (2.14)$$

$$\dot{\Omega} = \frac{1}{na^2\sqrt{1-e^2}\sin i} \frac{\partial \bar{U}}{\partial i} \quad (2.15)$$

A first approximation of the solution of Eq. (2.9) to (2.11) can be found by looking at the dominant terms of Eq. (2.12) through (2.15). First, the semi-major axis can be approximated by finding the solution of Eq. (2.4) considering only the J_2 effect in the series expansion of \bar{U} and neglecting the eccentricity. Consequently, Eq. (2.4) becomes:

$$C_2 a^{7/2} + C_1 a^2 + C_0 = 0 \quad (2.16)$$

where the coefficients C_0 , C_1 and C_2 are defined by:

$$C_0 = \frac{3}{2} \sqrt{\mu} J_2 R_{\oplus}^2 \left[\frac{D}{N} (4 \cos^2 i - 1) - \cos i \right] \quad (2.17)$$

$$C_1 = \frac{D}{N} \sqrt{\mu} \quad (2.18)$$

$$C_2 = -\omega_{\oplus} \quad (2.19)$$

An acceptable approximation of the solution to Eq. (2.16) axis is given below. This approximate value of the semi-major axis can in turn be used in Eq. (2.12) to (2.15).

$$a = -\left(\frac{C_1}{C_2}\right)^{2/3} \quad (2.20)$$

Considering only the terms J_2 and J_3 in the series expansion of \bar{U} , the LPEs for the time rate of the eccentricity and the argument of perigee can be written as follows:

$$\dot{e} = \frac{3}{2} n \left(\frac{R_{\oplus}}{a}\right)^3 \frac{J_3}{(1-e^2)^2} \sin i \cos \omega \left(\frac{5}{4} \sin^2 i - 1\right) \quad (2.21)$$

$$\begin{aligned} \dot{\omega} = & -\frac{3}{4} n \left(\frac{R_{\oplus}}{a}\right)^2 \frac{J_2}{(1-e^2)^2} (1-5 \cos^2 i) \\ & - \frac{3}{2} n \left(\frac{R_{\oplus}}{a}\right)^3 \frac{J_3}{e(1-e^2)^3} \frac{\sin \omega}{\sin i} \\ & \left\{ \left(\frac{5}{4} \sin^2 i - 1\right) \sin^2 i + e^2 \left(1 - \frac{35}{4} \sin^2 i \cos^2 i\right) \right\} \end{aligned} \quad (2.22)$$

The constraint on the time rate of the eccentricity and the argument of perigee can be satisfied in the J_2+J_3 by choosing the mean value of the argument of the perigee equal to $\pm \pi/2$ which nullifies Eq. (2.21) and the mean eccentricity equal to the value given in Eq. (2.23) where the minus sign corresponds to $\omega = \pi/2$ and the plus sign corresponds to $\omega = -\pi/2$:

$$e = \mp \frac{1}{2} \frac{R_{\oplus}}{a} \frac{J_3}{J_2} \sin i \quad (2.23)$$

Once the approximate solution is found for the zonal potential including only the dominant terms, an iterative procedure allows the refinement of the mean orbital elements to account for higher degrees of the averaged zonal potential. The iteration are performed through trial and error on the values of both the eccentricity and the semi-major starting with the initial values given by Eq. (2.19) and Eq. (2.23), keeping the value of the argument of the perigee equal to $\pm \pi/2$. For each iteration, the new value for a and e is computed using the Jacobian matrix of the system of equations (2.10) and (2.11):

$$\begin{bmatrix} a \\ e \end{bmatrix}_{new} = \begin{bmatrix} a \\ e \end{bmatrix} - \begin{bmatrix} \frac{\partial \dot{\omega}}{\partial a} & \frac{\partial \dot{\omega}}{\partial e} \\ D \frac{\partial \dot{M}}{\partial a} + N \frac{\partial \dot{\Omega}}{\partial a} & D \frac{\partial \dot{M}}{\partial e} + N \frac{\partial \dot{\Omega}}{\partial e} \end{bmatrix}^{-1} \begin{bmatrix} \dot{\omega} \\ D \cdot \dot{M} + N \cdot (\dot{\Omega} - \omega_{\oplus}) \end{bmatrix} \quad (2.24)$$

The next step is to determine the initial osculating orbital elements corresponding to the mean values previously found. The correction to apply to the mean orbital elements to get the osculating value is computed using the part of the zonal geopotential that includes only the short period perturbations. This potential is called U^* .

$$U^* = U - \bar{U} \quad (2.25)$$

where U is the non averaged zonal potential. The corrections to the orbital elements are obtained as functions of the mean values after the integration of the LPEs applied to the

potential U^* . Though these initial osculating orbital elements should lead to a near-repeat groundtrack after D days, the exact closure of the groundtrack is not ensured.

The purpose of the next step is to refine the value of the initial osculating elements to achieve an exact closure of the groundtrack. Lim (1995) showed that out of the six orbital elements, the ones experiencing the greatest variation between their initial value and their value at D days were the semi-major axis a and the argument of perigee ω . Therefore, a new trial and error procedure is performed to refine the initial values of the eccentricity and the semi-major axis in order to satisfy the following final conditions:

$$a_f(a_0, e_0, t_f) - a_0 = 0 \quad (2.26)$$

$$\omega_f(a_0, e_0, t_f) - \omega_0 = 0 \quad (2.27)$$

For each iteration, the new value for a and e is computed as follows:

$$\begin{bmatrix} a_0 \\ e_0 \end{bmatrix}_{new} = \begin{bmatrix} a_0 \\ e_0 \end{bmatrix} - \begin{bmatrix} \frac{\partial a_f}{\partial a_0} - 1 & \frac{\partial a_f}{\partial e_0} \\ \frac{\partial \omega_f}{\partial a_0} & \frac{\partial \omega_f}{\partial e_0} \end{bmatrix}^{-1} \begin{bmatrix} a_f - a_0 \\ \omega_f - \omega_0 \end{bmatrix} \quad (2.28)$$

As the value of the semi-major axis of the orbit is being modified, so is the nodal period of the satellite and the duration of a nodal day which is orbit-dependent. It is therefore necessary to adjust for the final time t_f along with the initial semi-major axis and eccentricities. This is done using the difference in longitude λ (in ECEF) of the node at the initial time and final time:

$$t_{f_{new}} = t_f - \frac{\lambda_f - \lambda_0}{\dot{\lambda}} \quad (2.29)$$

At this point of the procedure, only the zonal terms of the geopotential have been accounted for in the refinement of the initial osculating elements. A new set of initial osculating orbital elements can be estimated via a least square fit procedure that includes the tesseral and sectoral terms of the geopotential force model, starting with the initial osculating orbital elements obtained at the end of the previous step. However, the exact repeat condition is lost at the end of the estimation procedure. A new adjustment of the orbital elements, similar to Eq.(2.26) through Eq.(2.29), is necessary to conclude the design of a frozen exact repeat groundtrack in the full geopotential.

2.4 ICESAT REPEAT GROUNDTRACK ORBITS

The ICESat satellite operates with two different repeat orbits. The altimeter measurements are made when the satellite is flying in 91-day repeat orbit. A second orbit is an 8-day repeat orbit into which ICESat was initially launched. The 8-day repeat orbit was used during the calibration phase of the ICESat mission since it enabled the flight over specific calibration site every 8 days. A third orbit was generated for the ICESat mission. It was designed to be the actual operational orbit, with the groundtrack repeating every 183 days. A malfunction in the first of the three lasers onboard of ICESat caused the lifetime of the laser to be greatly decreased. Since it was assumed that this malfunction would affect all three lasers, it was decided to switch to a shorter orbit, hence

	8-day repeat	91-day repeat	183-day repeat
Number of nodal days (D)	8	91	183
Number of satellite revs. (N)	119	1354	2723
Ratio N/D	14.875	14.879	14.880
Mean Semi-major axis (km)	6971.524	6970.239	6970.033
Inclination (deg)	94	94	94

Table 2.1: Main characteristics of ICESat's repeat orbits

the 91-day repeat orbit. The reference orbits used in the ICESat missions were generated at the Center for Space Research (CSR). The actual satellite orbit is forced to follow these reference orbits with an allowed East/West displacement from the reference orbit of ± 800 meters at the equator. These reference repeat orbits were designed by Charles Webb (personal communication) through a numerical method based on the work by Lim (1995, 1996) described previously. The main characteristics of the three repeat orbits are summarized in Table (2.1).

The first step in the numerical method described in the previous section was to compute the values of the mean semi-major axis and the frozen eccentricity for the desired values of the inclination, D , N , and an approximate value for the semi-major axis. The frozen eccentricity and mean semi-major axis were obtained for a geopotential which accounts for the first 31 averaged zonal terms. The short period perturbations were then added to find the initial osculating elements in the non-averaged zonal potential up to the 31st degree. The adjustment of the initial osculating orbital elements was performed with

a convergence criteria for the groundtrack closure error to be less than 1 meter at the equator. Once the groundtrack was closed in the 31×0 geopotential, a new set of initial osculating orbital elements was computed via a least square fit using a more complete the geopotential including all the harmonics up to 70th degree and 70th order (70×70). Finally, the new initial osculating orbital elements were adjusted to achieve the closure of the groundtrack in the 70×70 geopotential with the same convergence criteria as before.

Two different gravity models were used to generate the 8-day, 183-day and 91-day repeat orbits in the method described above. The 8-day and 183-day repeat orbit were generated using the Joint Gravity Model 3 (JGM3) as it was the most accurate model at the time. The 91-day repeat orbit was generated later in the mission using the more accurate Grace Gravity Model 01 (GGM01). For the three reference orbit designed, the position of the satellite was obtained for 1 second sampling frequency over the entire repeat interval.

2.5 MOTIVATION AND OUTLINE OF WORK

Following the failure of the first laser, it was decided that the remaining 2 lasers onboard of ICESat would not be fired continuously as it was initially planned. Instead, the lasers are fired during campaigns of 33 days at a time. The duration of these campaigns was chosen according to what was then known as one of ICESat 91-day repeat orbit's *subcycles*. *Subcycles* are a characteristic of repeat groundtrack orbits that has not been the subject of much research at the time this dissertation is written. By making great

use of its repeat orbit subcycles, the ICESat mission proved the importance of including considerations on the choice of adequate subcycles in the design of a repeat orbit. The question of the subcycles will be approached both in a theoretical context and through the example of ICESat 91-day repeat orbit in Chapter 3.

On one hand, the altimetry measurements provided by the GLAS altimeter onboard of ICESat are performed over a portion of its groundtrack that corresponds to the 33-day campaign. On the other hand, there exist seasonal and calendar mission constraints for the timing of these measurements. To reconcile these two constraints, the ICESat team devised a set of standardized maneuvers to reposition the ICESat satellite above the desired portion of the groundtrack at the desired time. These maneuvers are called *phasing maneuvers* and make use of the 8-day calibration orbit as an intermediary orbit. Though these maneuvers were designed specifically for the ICESat mission, they represent a fuel-efficient standardized contingency option for any repeat orbit mission. We will therefore provide in Chapter 4 the framework necessary to the design of such maneuvers for any repeat groundtrack orbit.

Another line of work on the ICESat repeat groundtrack orbit came from the off-nadir capacity of ICESat's laser. There has been a growing interest in the ICESat off-nadir capacity, especially for the cross-validation of a future CryoSat mission, placed into a repeat groundtrack orbit and which mission objectives are similar to the ones of ICESat. A cross-validation procedure for CryoSat using ICESat altimeter measurements as

reference requires the precise determination of the locations of the intersections, or crossovers, between CryoSat and ICESat repeat groundtracks. The results of the study on these crossovers are presented in Chapter 5.

Finally, a study of the third body effect on ICESat 91-day repeat orbit is conducted in Chapter 6. When generating a precise reference repeat orbit, it is necessary to account for as many perturbing forces as possible. Each perturbing force neglected can cause a drift from the ideal reference orbit, which will in turn require correction maneuvers. Forces like drag or solar pressure are difficult to predict and to include in the design of a precise repeat orbit. Other forces however, like third body perturbations, can be accurately represented via a disturbing potential that can be expressed in terms of the satellite orbital elements. In the ICESat mission, it has been observed that the third body forces due to the gravitation of the Moon and the Sun cause a drift of the satellite's groundtrack that exceed the acceptable drift defined in the mission requirements (namely 800 meters from the reference groundtrack). About every three months, a North-South correction maneuver is applied to compensate for the change in inclination due to the luni-solar effect. The change in the argument of the node is compensated by an East-West correction maneuver which also accounts for the groundtrack drift due to the drag. It seems therefore interesting to include the luni-solar effect in the orbit design of a future mission in order to reduce the amount of fuel required for correction maneuvers. The necessary derivatives to include the third body effect into Lim's procedure for the design of frozen repeat orbits are developed in Chapter 6.

CHAPTER 3

SUBCYCLES OF REPEAT ORBITS

Repeat orbits are commonly used in Earth and climate changes monitoring missions for the advantages they present in terms of multiple and periodic observation opportunities. Besides these obvious advantages, the subcycles of a repeat orbit also represents an important orbit characteristic for the observation of the Earth, though little study has been conducted on the subcycle aspect of the repeat orbits. Work has been done however on the pattern of the groundtracks of repeat orbits. As far as the geometry of the repeat groundtracks is concerned, some important results were established by King^[11] regarding the location of the ascending nodes and by Farless^[12] on the topic of the location of crossovers for the Topex mission. The dynamic behind the subcycles of a repeat orbit and how they govern the overall pattern of the groundtrack is less understood. The subcycles of a repeat orbit are however of great importance as they can help resolve conflicting requirements from satellite users that need frequent observation opportunities and dense coverage at the same time (Rees, 1992), especially when there

are multiple users, or multiple scientific communities making use of one satellite placed in a repeat orbit as it is the case for the ICESat mission. Using the theoretical framework developed by Lim (1995), we analyze ICESat's repeat orbits and subcycles as an example.

3.1 DEFINITIONS

3.1.1 REPEAT CYCLE

We consider a satellite in a repeat orbit made of N satellite revolutions and of duration D nodal days. We call *repeat cycle* the time interval that separates one arbitrary ascending node that represents the origin of the repeat cycle, AN_0 , from the ascending node that corresponds to the $N+1^{\text{th}}$ ascending node after AN_0 . This later ascending node represents the end of the repeat cycle and is designated as AN_N and the node AN_0 is called the *reference ascending node* of the repeat cycle. This implies that the duration of a repeat cycle is equal to D nodal days and that the repeat groundtrack starts retracing itself at the end of one repeat cycle. When defined in an Earth-fixed frame, the N ascending (respectively descending) equatorial crossings divide the equator into N equal segments of arc (King, 1976). The angle separating two ascending (respectively descending) nodes consecutive in space is called *nodal spacing* (Lim, 1995) and is referred to as σ . Since the distribution of the nodes is uniform throughout the 360° of the equator, one nodal spacing is equal to :

$$\sigma = \frac{2\pi}{N} \quad (3.1)$$

Each ascending (respectively descending) equatorial crossing is intersected along the ascending (respectively descending) direction once and only once throughout one repeat cycle. Finally, the angle separating two ascending nodes consecutive in time is called *longitude shift* and is equal to $D\sigma$ (King, 1976). The value given by Eq. (3.2) represents only the magnitude of the shift. Some considerations on the orbit need to be made to determination the direction of the longitude shift.

$$\Delta\lambda = D\sigma = \frac{2\pi D}{N} \quad (3.2)$$

Using the reference orbits generated at the CSR for the ICESat mission, we can obtain the average values for the longitude shift, $\Delta\lambda$, and the nodal spacing, σ over the repeat cycle. We can compare these values to the ones obtained with Eq. (3.1) and Eq. (3.2). The results are summarized in Table (3.1) for the three reference orbits. The negative values in the first column show that the track is shifting westward, which is consistent with the comment made in the previous chapter about Eq.(2.1).

We observe that Eq. (3.1) and Eq. (3.2) that characterize the spacing between tracks in a ideal model match the average values of the reference with an accuracy in the order of 10^{-6} degrees for the three repeat orbits and . Consequently, the standard deviations for the longitude shift and the nodal spacing of the reference orbits correspond to the quadratic errors between the simplified theoretical values from Eq. (3.1) and Eq. (3.2) and the nominal values. In the case of the 183-day repeat orbit, the error corresponds to a

	Longitude Shift, $\Delta\lambda$		Nodal Spacing, σ	
	Ref. Orbit: ~ average value ~ <i>std. deviation</i>	Eq. (3.2)	Ref. Orbit: ~ average value ~ <i>std. deviation</i>	Eq. (3.1)
8-day repeat (deg)	-24.2016815 $s = 7.26 \cdot 10^{-4}$	24.2016807	3.0252077 $s = 3.61 \cdot 10^{-4}$	3.0252101
91-day repeat (deg)	-24.1949770 $s = 7.20 \cdot 10^{-4}$	24.1949778	0.2658787 $s = 1.83 \cdot 10^{-4}$	0.2658789
183-day repeat (deg)	-24.1939032 $s = 3.17 \cdot 10^{-3}$	24.1939038	0.1322078 $s = 3.49 \cdot 10^{-3}$	0.1322071

Table 3.1: Spacing between time-consecutive, $\Delta\lambda$, and space-consecutive, σ , ascending nodes.

distance of 400 meters at the equator. For the 8-day and 91-day repeat orbits, this distance is between 20 and 80 meters. These errors, though too large to study the closure of the groundtracks or to determine the exact location of the sub-satellite nadir point, are acceptable for our study of the relative distribution of the tracks and the general overall groundtrack pattern throughout the repeat cycle.

We also observe that the longitude shifts of the three orbits are of the same order. As illustrated in Eq. (3.2), it is a direct consequence of the three ratios N/D being comparable which itself is a consequence of the semi-major axes also being comparable, as summarized in Table (2.1).

3.1.2 NEAR REPEAT GROUNDTRACKS

Although the groundtrack shifts are almost identical for the three ICESat repeat orbits, Fig. (3.1) and Fig. (3.2) show the consequence of the small difference in the shift on the overall layout of equatorial crossings. The two numbers appearing to the right of the crossing are the official node number (above) as used in the ICESat data processing and the longitude difference (below) with the reference ascending node AN_0 of the repeat cycle considered.

In the official ICESat data processing, the nodes are assigned a track number in a *chronological order*, i.e. the order in which the ICESat satellite flies over the nodes. The track number #1 is assigned to the node the closest to the Greenwich meridian. Since the choice of the reference ascending node of the repeat cycle is often chosen with considerations to the mission time line and required maneuvers, the reference ascending is not necessarily assigned the track number #1.

The reference ascending node of the 8-day repeat cycle represented on Fig. (3.1) is designated as the node #29. It can be observed that the next node, #30, which occurs one satellite revolution later, is not found immediately to the left of the node #29 (the direction of the longitude shift is westward). Indeed, in the case of repeat orbits for which $D > 1$, therefore $\Delta\lambda > \sigma$, the distribution of the ascending nodes along the equator is not consistent with the order in which they occur throughout the repeat cycle. Consequently, several other equatorial crossings will lie in between two time-consecutive equatorial

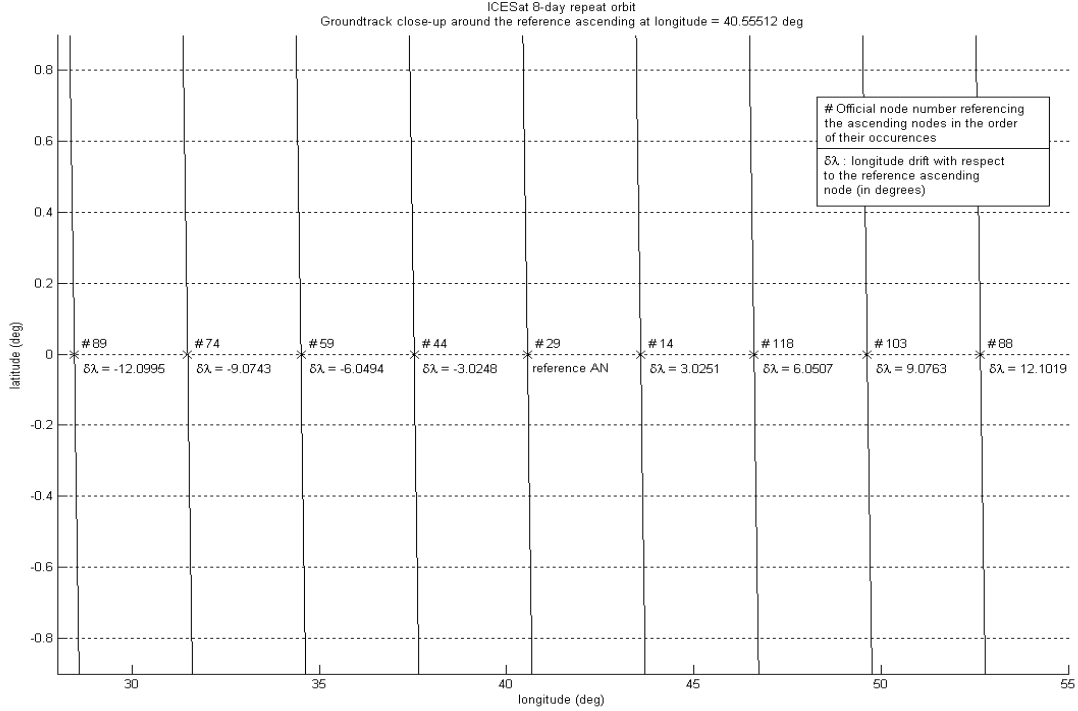


Fig. 3.1: Close up of the groundtrack pattern at the equator in the case of ICESat's 8-day repeat orbit (only ascending track segments are shown).

crossings. In the case of the 8-day repeat orbit, we observe that 7 ascending nodes are found between the nodes #88 and #89. That is to say that the node #89 lies 8 nodes west of the node #88. This is consistent Eq.(3.2).

Similarly on Fig. (3.2), the reference ascending node is designated as #1132. Directly west of the node #1278 is the node #787. In the case of the 91-day repeat orbit, the time-consecutive node to node #1278, i.e. node #1279, is found 91 nodes west of node #1278. The node #1279 does not appear on Fig. 2, since only 11 ascending nodes are represented on the graph for readability purposes.

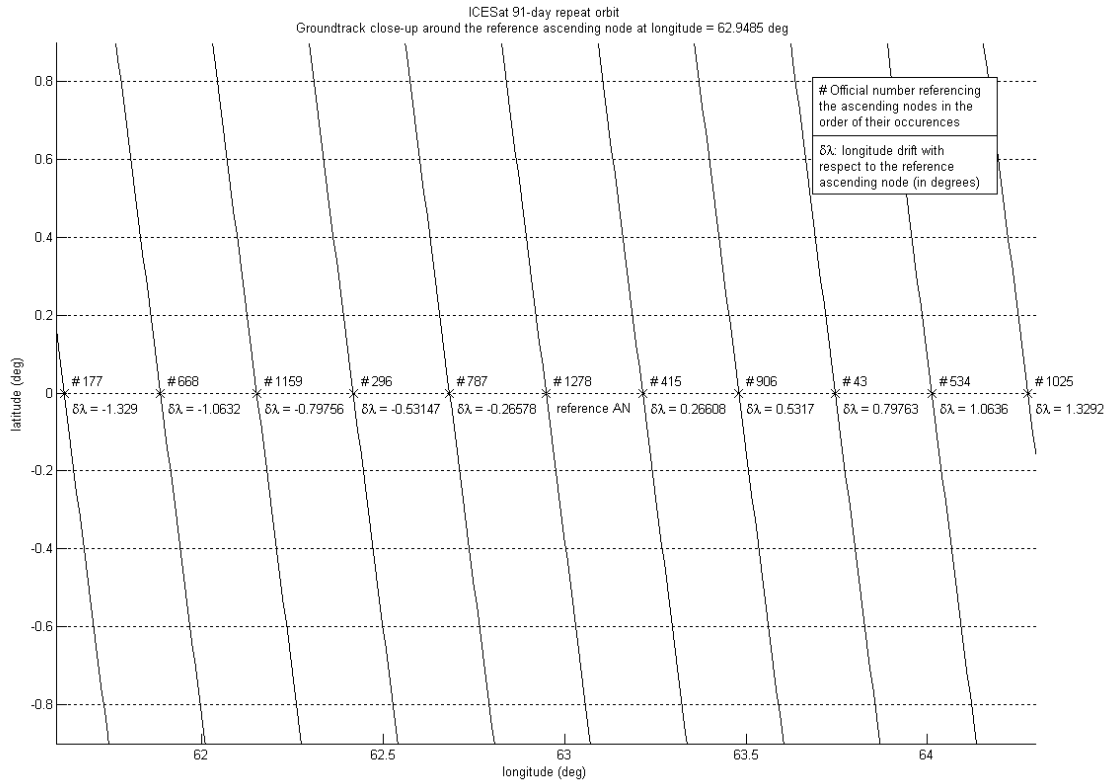


Fig. 3.2: Close up of the groundtrack pattern at the equator in the case of ICESat's 91-day repeat orbit (only ascending track segments are shown).

In the case of the ICESat 91-day repeat orbit, the distance between two space-consecutive tracks is approximately equal to 29.6 km at the equator. For example, the track #906 lies 29.6 km west of the track #415. This means that after 491 satellite revolutions, the groundtrack almost retraces itself. The track #906 is called *near-repeat groundtrack* with respect to track #415. Near-repeat groundtracks are very important in mapping missions because they perform a global coverage in a time interval corresponding to one *near-repeat cycle*^[Mars Global Surveyor – 14]. In the case of the ICESat 91-day orbit, the near-repeat cycle that corresponds to 491 satellite revolution has an offset of 29.6 km eastward.

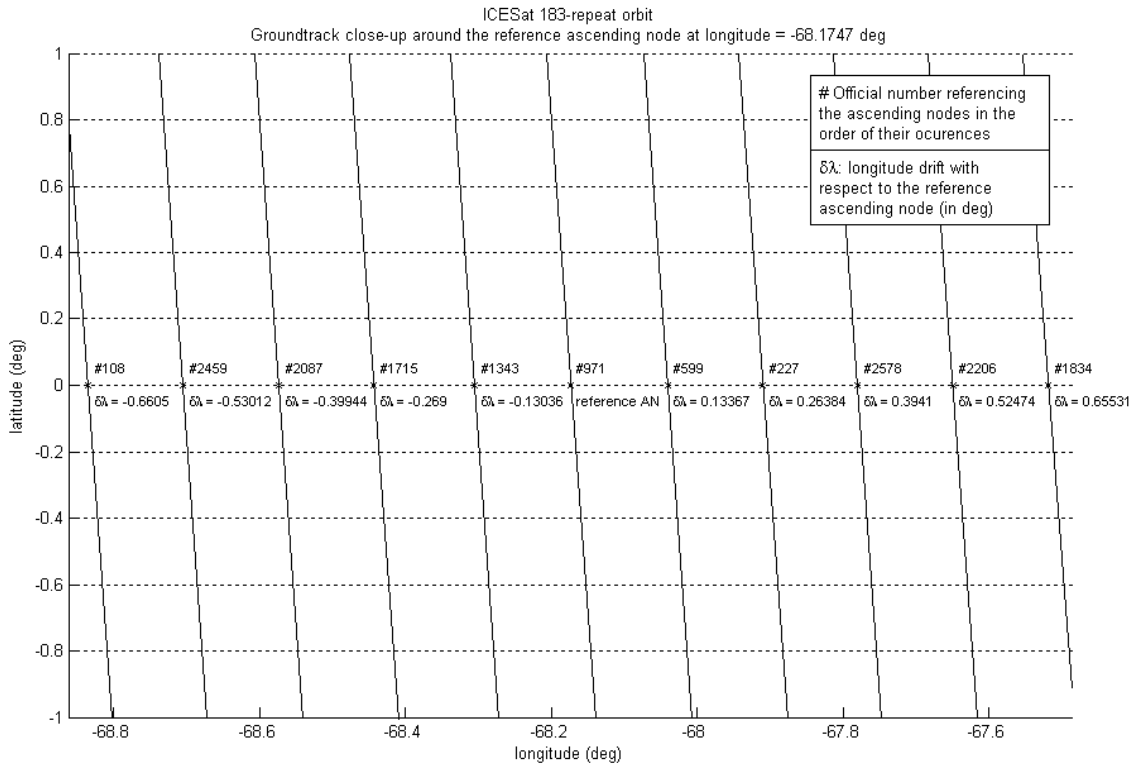


Fig. 3.3: Close up of the groundtrack pattern at the equator in the case of ICESat's 183-day repeat orbit (only ascending track segments are shown).

There exist other near-repeat cycles to the ICESat 91-day repeat orbit. A second near-repeat groundtrack corresponding to 365 satellite revolutions is illustrated by the tracks #906 and #1278. The track #1278 lies two nodal spacing, i.e. 59.2 km, west of the track #906. This second near-repeat cycle is shorter in time, but the offset between the tracks is twice the one described in the previous paragraph and in the opposite direction.

In the case of the 183-day repeat orbit, the distance between two space-consecutive nodes is approximately equal to 14.7 km at the equator. Therefore on Fig. (3.3), the node#1343 lies 14.7 km west of the reference node whose track number is #971. This means that there exist a near repeat cycle with an offset of one nodal spacing westward

and corresponding to 372 satellite revolutions. Another near repeat cycle can be found with an offset of three nodal spacing eastward and corresponding to 1607 satellite revolution. This near repeat cycle is illustrated by the ascending node referenced as #2578. Many more near repeat cycle can be read on Fig. (3.3) in both directions: eastward and westward.

As before, only 11 tracks are shown for readability purposes. Therefore, Fig. (3.3) does not show two time consecutive nodes. The ascending node belonging to track #972, that occurs one satellite revolution after the reference ascending node and separated from it by one longitude shift, would be found 183 nodes west of track #971.

3.1.3 SUBCYCLES

We use the definition of a *subcycle* as it was given by Lim^[1,2] for the study of a 183-day repeat groundtrack for the EOS ALT/GLAS mission. According to his definition, a subcycle is an integer number of nodal days after which the groundtrack nearly repeats itself with a small offset. This offset can be described as a multiple of nodal spacing. In other words, a subcycle can be viewed as a near-repeat cycle with a duration equal to a integer number of nodal days. It is therefore relevant to identify the D ascending nodes of the repeat cycle that correspond to an integer number of nodal days in order to select the ones for which the longitude difference with the reference ascending node is small.

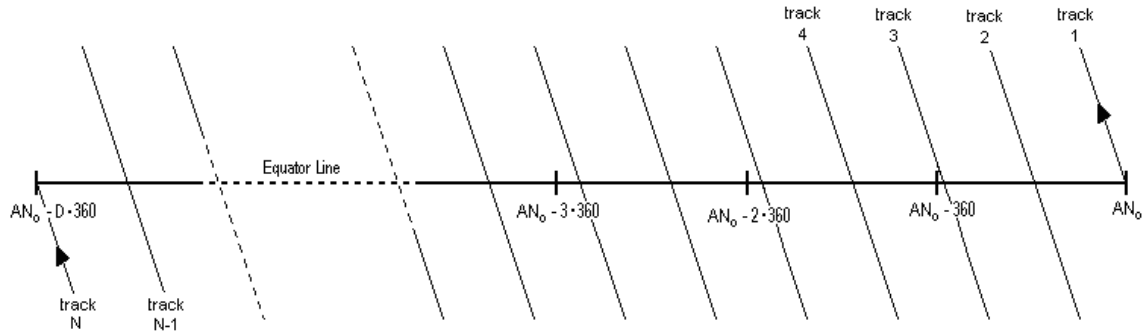


Fig. 3.4: Spacing pattern of the ascending nodes on the extended equatorial arc.
(Simplified illustration for a retrograde orbit, not the actual ICESat groundtrack)

To identify these D ascending nodes, we use an approach similar to the one used by (King, 1976). For an observer at a fixed location in the satellite orbit plane above the Earth equator, the equatorial arc from longitude AN_0 to longitude $AN_0 - 360$ represents a $+360^\circ$ rotation of the Earth. In other words, this equatorial arc represents one nodal day. Consequently, the entire D -day repeat cycle can be represented by repeating D times this equatorial arc in a continuous line. We call *extended equatorial arc* the equatorial line made of these D equatorial arcs and *extended longitude* the longitude of a node on the extended arc. The extended longitude of node is therefore in the interval $(AN_0 - D \cdot 360; AN_0)$ and corresponds to the traditional longitude modulo 360° . On the extended equatorial arc, the longitude AN_0 is represented $D+1$ with a modulo 360° and the N^{th} ascending node of the orbit's groundtrack coinciding with the D^{th} repetition of the origin AN_0 . This representation of the extended equatorial arc is shown in Fig. (3.4).

The Earth performs a rotation of 360 degrees with respect to the orbit plane in one nodal day. Consequently, every single equatorial arc $\{AN_0 - k \cdot 360; AN_0 - (k - 1) \cdot 360\}$, with $k=1...D$, shown on Fig. (3.3) represents one nodal day and every value of $(AN_0 - k \cdot 360)$ refers to the same traditional longitude AN_0 on the equator. Thus, looking for the subcycle at k nodal days is equivalent to looking for the ascending node whose extended longitude is the nearest to $(AN_0 - k \cdot 360)$ on Fig. (3.3). This way, $D-1$ ascending nodes are identified; the D^{th} ascending node identified is the one occurring after D nodal days, that is to say when the groundtrack repeats itself exactly. The D^{th} subcycle coincides with the complete D -day repeat cycle and the longitude of its ascending node is AN_0 . For each extended longitude $(AN_0 - k \cdot 360)$, the closest ascending node is selected among all the orbit's ascending nodes. Therefore, if the D equatorial arcs are superimposed again (which is equivalent to switching from the extended longitudes to traditional longitudes) the $D-1$ ascending nodes selected are naturally the $D-1$ closest ascending node to the origin of the repeat cycle AN_0 .

Looking back at Fig. (3.1), this means that the 4 tracks west of the reference ascending node (#89, #74, #59, #44) and the 3 tracks east of the reference ascending node (#14, #118, #103) correspond to the 7 subcycles of the ICESat 8-day repeat orbit. The 8th subcycle corresponds to the complete 8-day repeat cycle. In the case of the ICESat 91-day repeat orbit, the first 45 ascending nodes west of the reference node and the first 45 east of the reference ascending node correspond to the 90 subcycles of the repeat orbit. Finally in the case of the 183-day repeat orbit, the first 91 ascending nodes west and the

first 91 ascending nodes east of the reference ascending node correspond to the 182 subcycles of the repeat orbit. Fig. (3.2) and Fig (3.3) show only 11 tracks each, including the reference ones. Therefore, all the nodes represented on Fig. (3.2) and Fig. (3.3) correspond to subcycles of their respective repeat orbits.

One remark should be made about the definition of subcycle. In Lim’s definition, there are no specifics given for the offset, other than being “small”. On Fig. (3.1), let’s consider the 4th ascending node west of the origin of the 8-day repeat cycle (# 89). We could consider the 45th ascending nodes east and west of the origin of the 91-day repeat cycle, or also the 91st ascending nodes east and west of the origin of the 183-day repeat cycle, not represented in Fig. (3.2) and Fig (3.3). They all lie about 1350km from the repeat cycles’ reference ascending nodes. In these cases, the offsets of the groundtracks are not small. However, to remain general in our study and since the acceptable range for the groundtrack offset depends on mission requirements, all the D - I ascending nodes identified by the method above will be called subcycles of the D -day repeat orbit they belong to.

It is also important to understand that the crossing of the equator corresponding to the k -day subcycle does not occur exactly at the time corresponding to k nodal days. Indeed, if the crossing of the equator was to occur exactly at that time, then the extended longitude of that ascending node would be $(AN_0 - k \cdot 360)$ in the extended equatorial arc. This longitude would therefore correspond to the reference longitude AN_0 with a modulo 360° . That is to say that the groundtrack would repeat itself exactly at the end of the k^{th}

nodal day. In the case of non-degenerated orbit (the ratio N/D is irreducible), this only occurs for $k = D$. Moreover, observations show that the greater the difference between the longitude of AN_0 and the longitude of the ascending node corresponding to the k -day subcycle, the greater the time difference (positive or negative) between the occurrence of the crossing and the time corresponding to k nodal days exactly.

3.2 SUBCYCLES OF THE THREE ICESAT REPEAT ORBITS

Once the ascending nodes that correspond to the subcycles are identified as described above, the results are shown in a graph that we call *chart of subcycles*. For each subcycle, the chart shows the number of nodal days versus the groundtrack offset from the longitude of the reference ascending node AN_0 . These offset values are presented in two different ways. The scale of the Y-axis shows the distance between the tracks at the equator (in km). The offset is also shown as a multiple of the nodal spacing, σ . A positive offset is to be interpreted as an offset to the east, and a negative offset as an offset to the west. The chart also lists the number of satellite revolutions, m , for each subcycle.

Fig. (3.5) shows the chart of subcycles for the ICESat 8-day repeat orbit. All the subcycles represented on Fig. (3.1) appear on the chart: four subcycles westward and three subcycles eastward. The new information given by the chart is the number of nodal days at which each subcycle occurs. In the case of the 8-day orbit the layout of the subcycles throughout the entire repeat cycle is very simple.

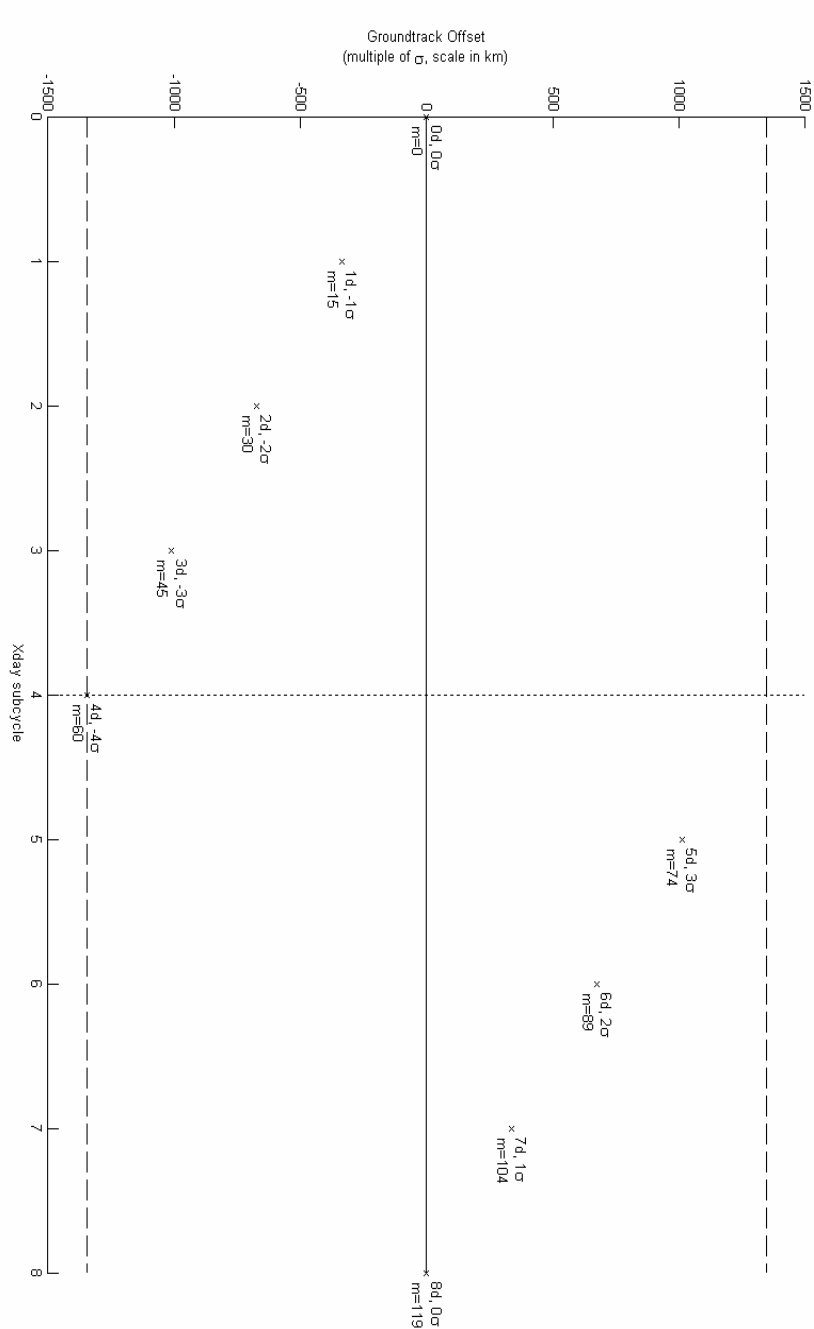


Fig. 3.5: Chart of subcycles for the ICESat 8-day repeat orbit with $N = 119$. For each subcycle, the number of the nodal can be read on the X-axis (Xday) or on the graph (for example $2d$ correspond to the 2-day subcycle). The offset can be read on the Y-axis in km at the equator or on the graph in terms of nodal spacings (for example 2σ correspond to an offset of two nodal spacings westward). The parameter m represents the number of satellite revolutions corresponding to each subcycle.

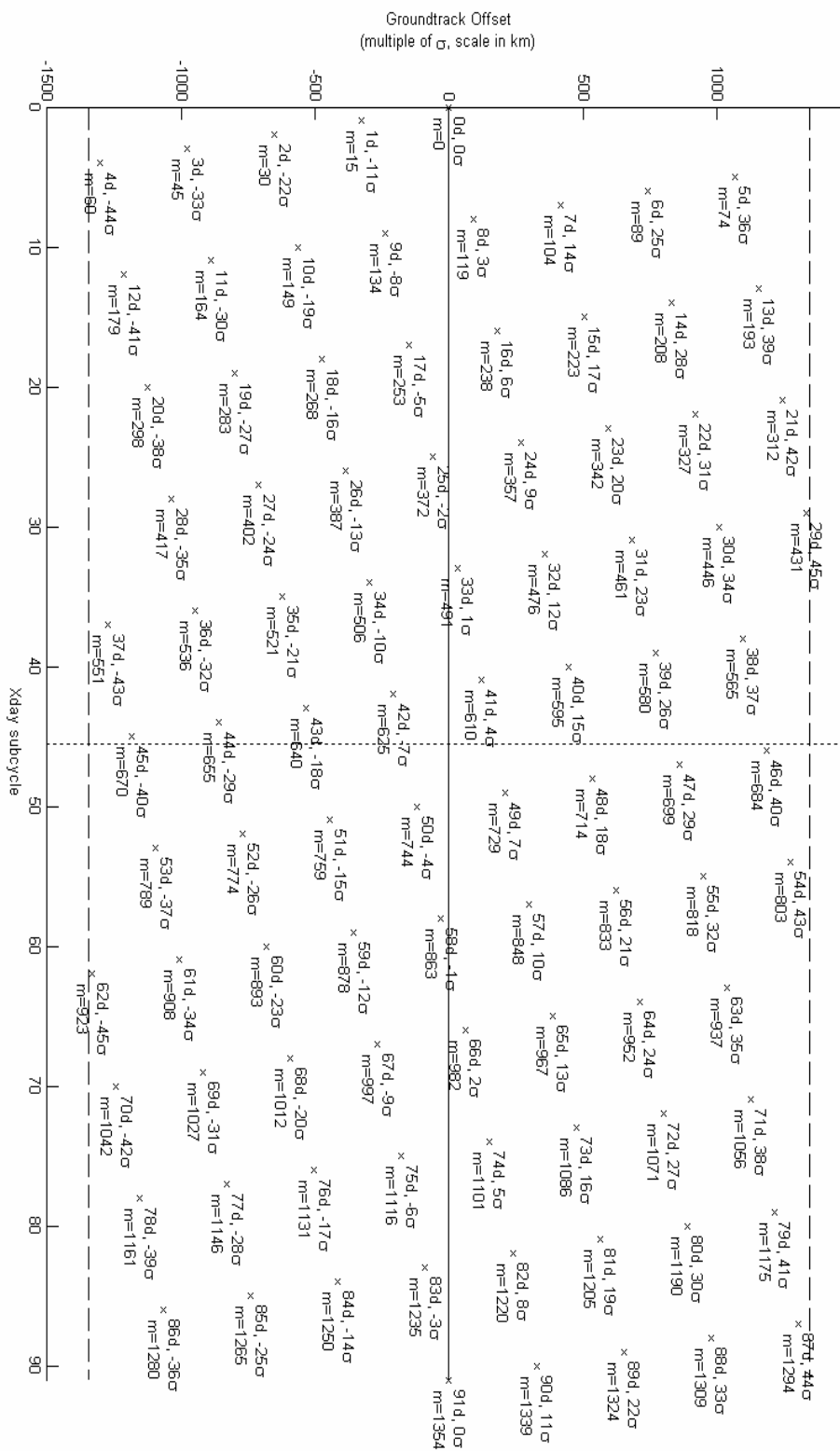


Fig. 3.6: Chart of subcycles for the ICESat 91-day repeat orbit with $N = 1354$.

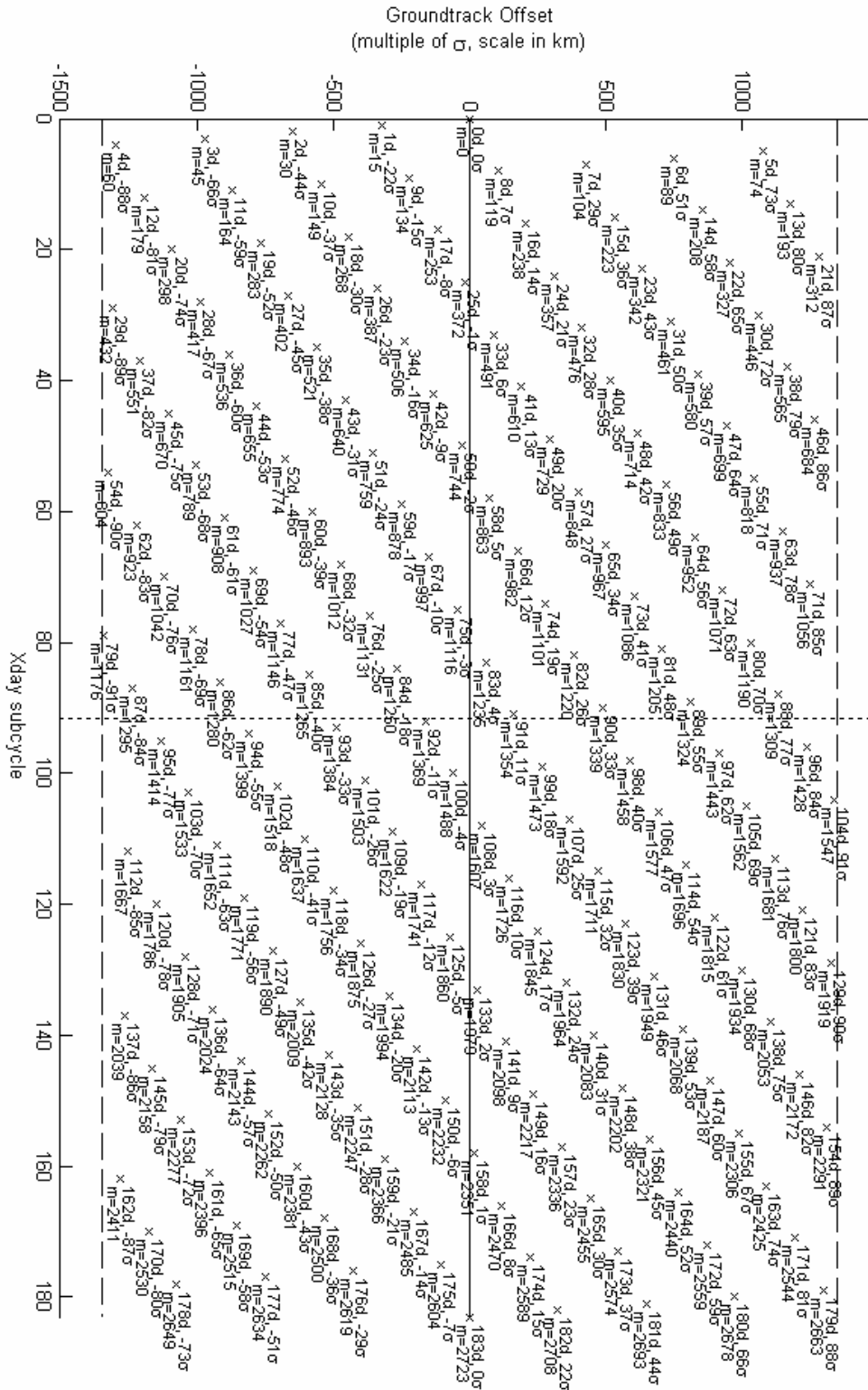


Fig. 3.7: Chart of subcycles for the ICESat 183-day repeat orbit with $N = 2723$.

Fig. (3.6) and Fig. (3.7) show the chart of subcycles for the ICESat 91-day and 183-day repeat orbits respectively. In these two cases, the layouts of the subcycles are more complex. It is however possible to identify a few geometrical properties on the charts of subcycles. These properties allow to easily breakdown the repeat cycle into a succession of several subcycles for which the offsets from the reference ascending node remain small.

3.3 PROPERTIES OF THE CHART OF SUBCYCLES

3.3.1 BOUNDED DISTRIBUTION

The first property exhibited on Fig. (3.5)) is that the distribution of the offsets is bounded. This property corresponds to the previous discussion on the location of the subcycles. The maximum offsets are found within $\pm D\sigma/2$. These boundaries are reached, i.e. there exists a subcycle with an offset at $\pm D\sigma/2$ exactly, if and only if D is an even number. For example on the chart for the 8-day repeat orbit in Fig. (3.5), the largest offset corresponds to the 4-day subcycle with a deviation of 4σ eastward. In the case of the 91-day repeat orbit on Fig. (3.6), the largest offsets are found for the 29-day subcycle with an offset of 45σ and the 62-day subcycle with an offset of -45σ . Finally on Fig (3.7) showing the subcycles of ICESat 183-day repeat orbit, the two largest offsets are found for the subcycles at 79 nodal days with a deviation of -91σ and 104 nodal days with a deviation of 91σ .

3.3.2 SYMMETRICAL DISTRIBUTION

A second property illustrated by the charts of the three ICESat orbits is the central symmetry of the distribution of the subcycle. The central point of symmetry is located on the chart at the coordinates $\{(D/2)d, 0\sigma\}$. For example, on Fig.(3.6), the subcycle at 32 nodal days $\{32d, +12\sigma\}$ has a symmetrical subcycle at 59 nodal days $\{59d, -12\sigma\}$. These two subcycles are at the same distance from the central point of symmetry on the chart. Moreover, their groundtrack offsets have the exact opposite value. The three charts presented in Fig. (3.5) to (3.7) show that every subcycle has a symmetrical subcycle. The only exception is found for the 8-day repeat orbit. The subcycle at 4 nodal days with an offset of -4σ does not exhibit any symmetrical subcycle at $+4\sigma$. This is typical of non-degenerated repeat orbit with an even number of nodal days. When D is an even integer, there is an odd number, $D-1$, of subcycles. Naturally, the symmetry of the distribution is broken (for one subcycle) in the case of an odd number of subcycles. In the case of these orbits, the subcycle at $D/2$ nodal days is found on either the upper or lower boundary described in the previous section. We'll see in the following section how, to some extent, this is still consistent with the overall symmetry of the subcycles' distribution.

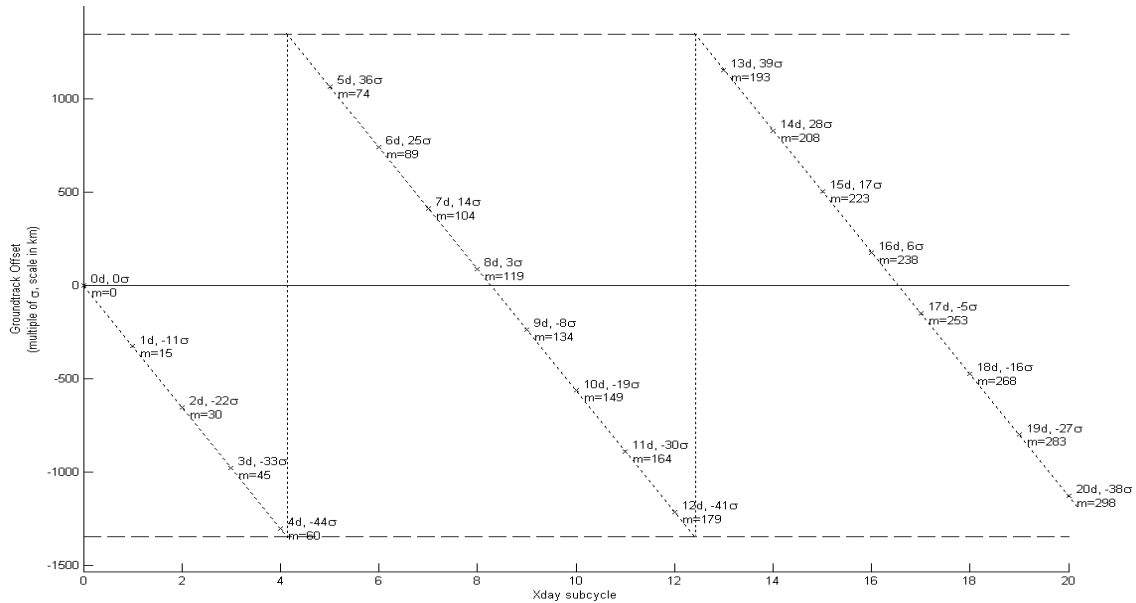


Fig. (3.8): Close-up of Fig. (3.6). The subcycles are located on a set of parallel lines. In the case of ICESat 91-day repeat orbit, the slope of these lines is -11σ per nodal day.

3.3.3 LINEAR DISTRIBUTION

The third property is the linearity of the distribution of the subcycles. The distribution of the offsets from the reference ascending node AN_0 consists of a set of parallel straight lines. The slope of these lines can be read simply by looking at the first subcycle. In the case of ICESat 91-day orbit represented in a close-up view on Fig. (3.8), the first subcycle (subcycle corresponding to one nodal day) is found at a deviation of -11σ . Consequently, the slope of the lines is equal to -11σ per nodal day; in other words, the ICESat groundtrack shifts 11 nodal spacings westward per nodal day. In the case of the 183-day repeat orbit, Fig. (3.9) shows that the slope is twice the one of the 91-day

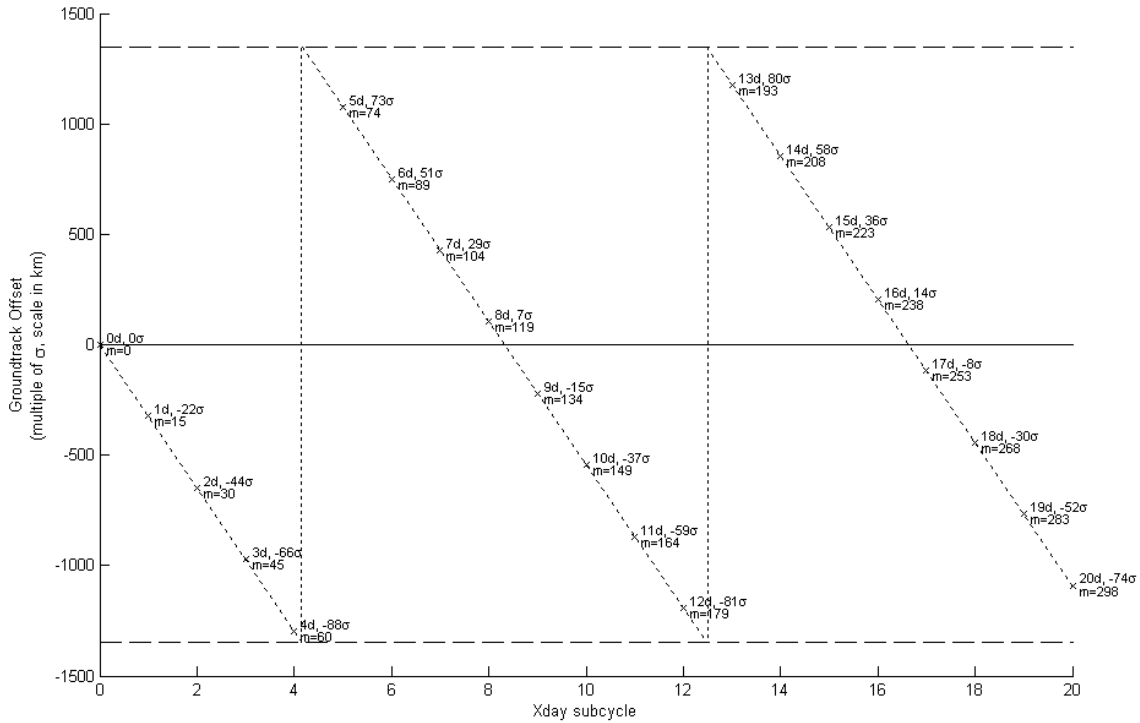


Fig. (3.9): Close-up of Fig. (3.7). In the case of ICESat 183-day repeat orbit, the slope of these lines is -22σ per nodal day.

repeat orbit, that is to say that the groundtrack shifts 22 nodal spacings westward per nodal day. Keeping in mind that the value of the nodal spacing is orbit dependent, the groundtrack shift per nodal day of each orbit are actually of the same order.

It might be useful to visualize a chart of subcycle as a three dimensional torus as shown on Fig. (3.10). First, let's transform the chart into a horizontal *cylinder* by patching the upper boundary at $+D\sigma/2$ to the lower boundary at $-D\sigma/2$. This is an artificial transformation that is inspired by the fact that the extremities of each segment on Fig. (3.8) and (3.9) lines up perfectly with one another (as illustrated by the vertical lines). In

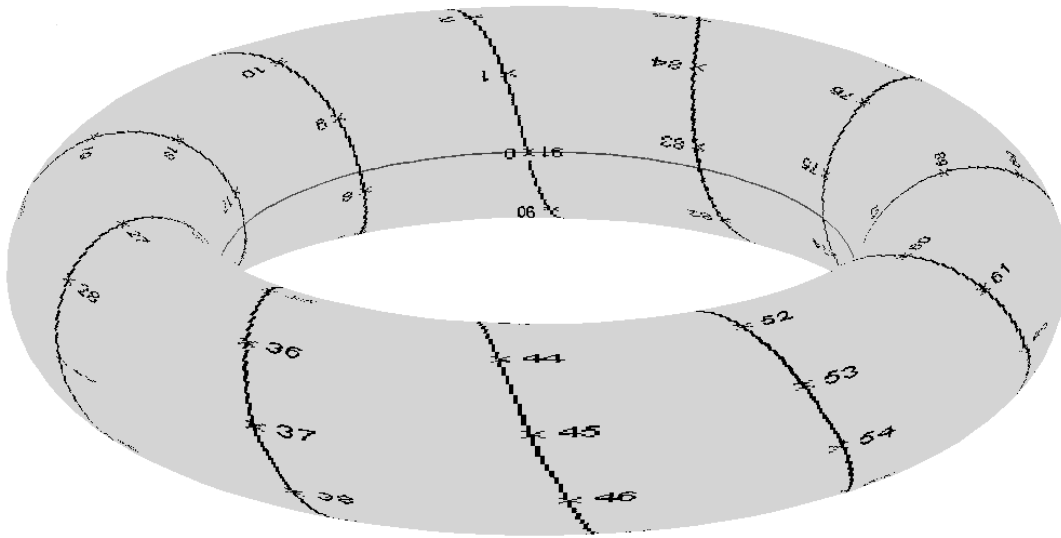


Fig. (3.10): Three-dimensional representation of the chart of subcycles for ICESat's 91-day repeat orbit.

this representation, the set of parallel lines become one continuous spiral around the cylinder. Then, by patching the edge of the cylinder at $X = 0$ days to the edge at $X = D$, we obtain a torus on which the spiral closes. This second transformation is not as artificial since it represents the periodicity of the repeat groundtrack.

The representation of the chart of subcycle as a three dimensional torus does not have a physical meaning, but it is useful to fully understand the next property. It also reconciles the absence of a symmetrical subcycle when the offset of the subcycle is found on either the upper or lower boundary. In the torus representation, both boundaries are merged together and a subcycle with an offset on any of the boundary becomes its own symmetrical subcycle.

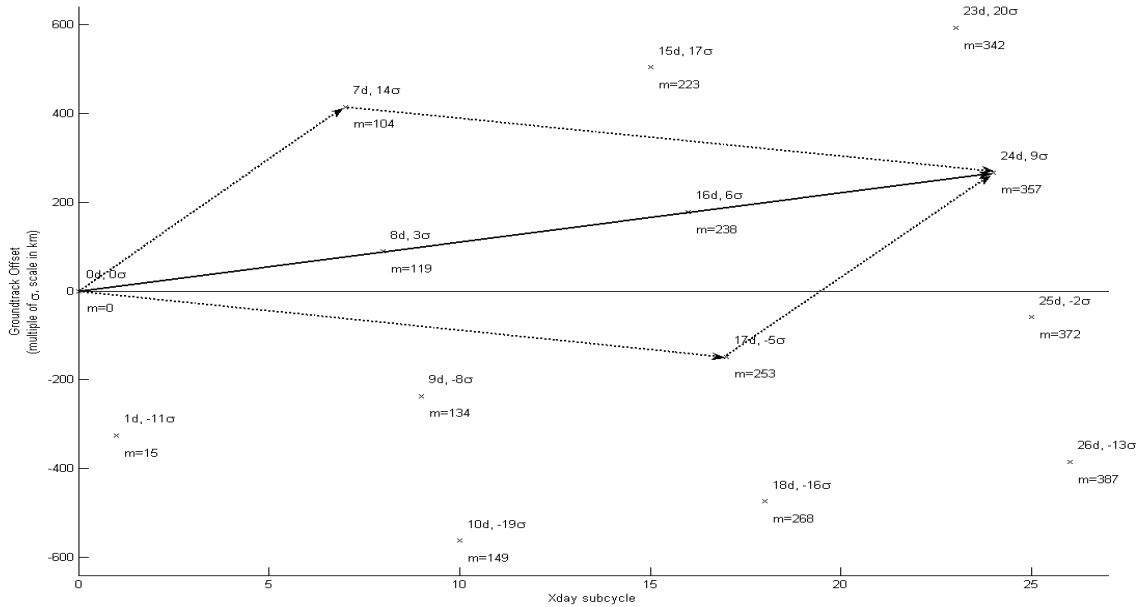


Fig. (3.11): Close-up of Fig. (3.6). The combination of the 7-day subcycle and the 17-day subcycle leads to the 24-day subcycle. On the chart of subcycles, the subcycles can be added like vectors.

3.3.4 SUBCYCLE COMBINATION

The last property of the chart of subcycles is less trivial. On the chart, subcycles can be added together like vectors, which we call *subcycle combination*. For example the chart shown on Fig. (3.6), exhibits a subcycle at 7 nodal days with an offset of $+14\sigma$ and $m = 104$. Another subcycle is found at 17 nodal days with an offset of -5σ and $m = 253$: The subcycles are respectively labeled $(7d,+14\sigma)$ and $(17d,-5\sigma)$. As shown on the chart, the subcycle at 24 nodal days has an offset of $+9\sigma$ and $m = 357$. The offset and the number of satellite revolutions for the 24-day subcycle correspond to the sum of the ones

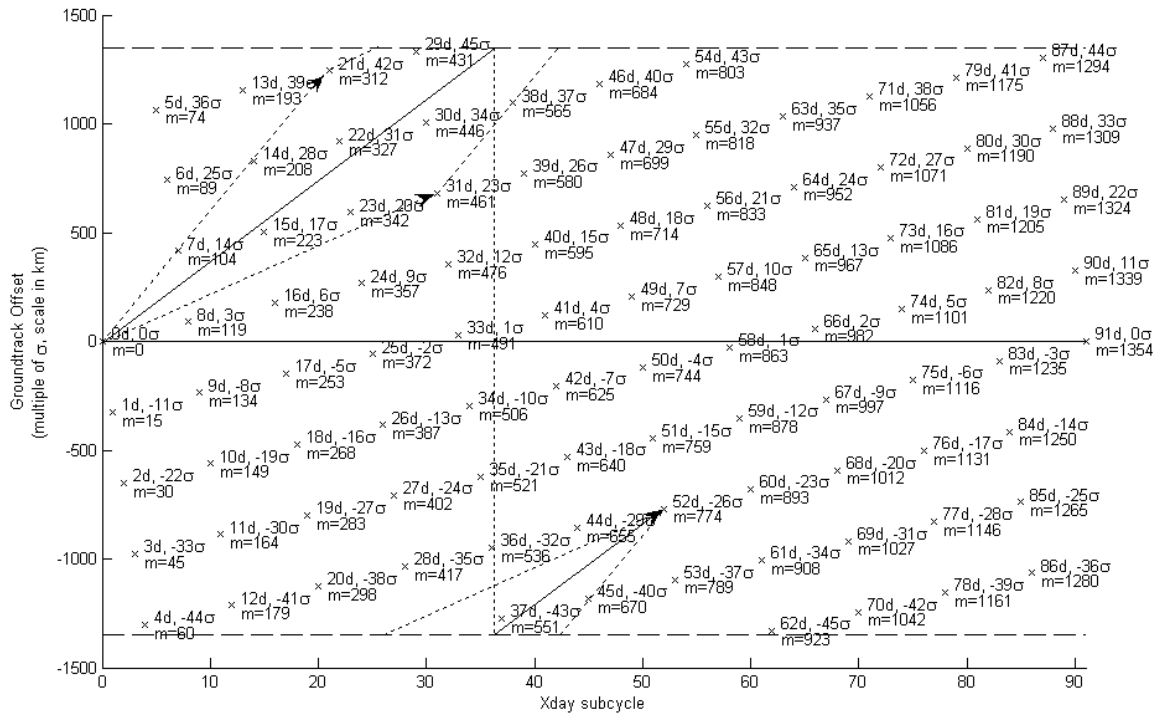


Fig. (3.12): The combination of the 21-day subcycle and the 31-day subcycle. leads to the 52-day subcycle when the combination is considered in the three dimensional representation.

corresponding to the two previously mentioned subcycles. This combination is easily identified by a vectorlike addition of the subcycles as shown on Fig. (3.11). The representation of the chart as a torus allows extending this property to combinations of subcycles that would otherwise lead incorrectly to a resulting subcycle outside of the chart's boundaries as illustrated on Fig. (3.12).

3.4 ICESAT'S SEQUENCE OF SUBCYCLES

Using this last property, it became possible to illustrate a very particular characteristic of ICESat's repeat cycle. In the 91-day repeat orbit, it was observed that a subdivision of the cycle into three main subcycles of 33 days, 25 days, and 33 days led to offsets of one nodal spacing at the end of each subcycle. This pattern can be explained using the chart shown on Fig. (3.6). The subcycle at 33 nodal days has an offset of $+1\sigma$ as represented on Fig. (3.3). If this subcycle is then combined with the one at 25 nodal days labeled $\{25d, -2\sigma\}$, the resulting subcycle is therefore the one labeled $\{58d, -1\sigma\}$. Finally, combining this resulting subcycle with another 33-day subcycle $\{33d, +1\sigma\}$ leads to the full cycle $\{91d, 0\sigma\}$. The ICESat entire cycle can therefore be achieved with a 33-25-33 subcycle sequence. Fig. (3.6) also illustrates the existence of many other subcycle sequences. For example, one among many could be the 8-17-8-17-16-17-8 subcycle sequence which leads the following successive offsets: $+3\sigma, 2\sigma, +1\sigma, -4\sigma, +2\sigma, -3\sigma$. However, the 33-25-33 subcycle sequence might be the most interesting sequence as it is the only one with the offsets no greater than $\pm 1\sigma$. More specifically, such a sequence gives an interpretation of the layout of the groundtrack throughout the entire repeat cycle. The 33-25-33 subcycle sequence divides the repeat cycle into three *main subcycles (MS)*: *MS1* corresponds to the first 33 nodal days of the repeat cycle, *MS2* corresponds to the following 25 nodal days, finally *MS3* corresponds to the last 33 nodal days. During *MS1*, a first segment of the groundtrack is being traced. The groundtrack flown over during *MS2* almost retraces, or duplicates, the one corresponding to *MS1* but with an offset of

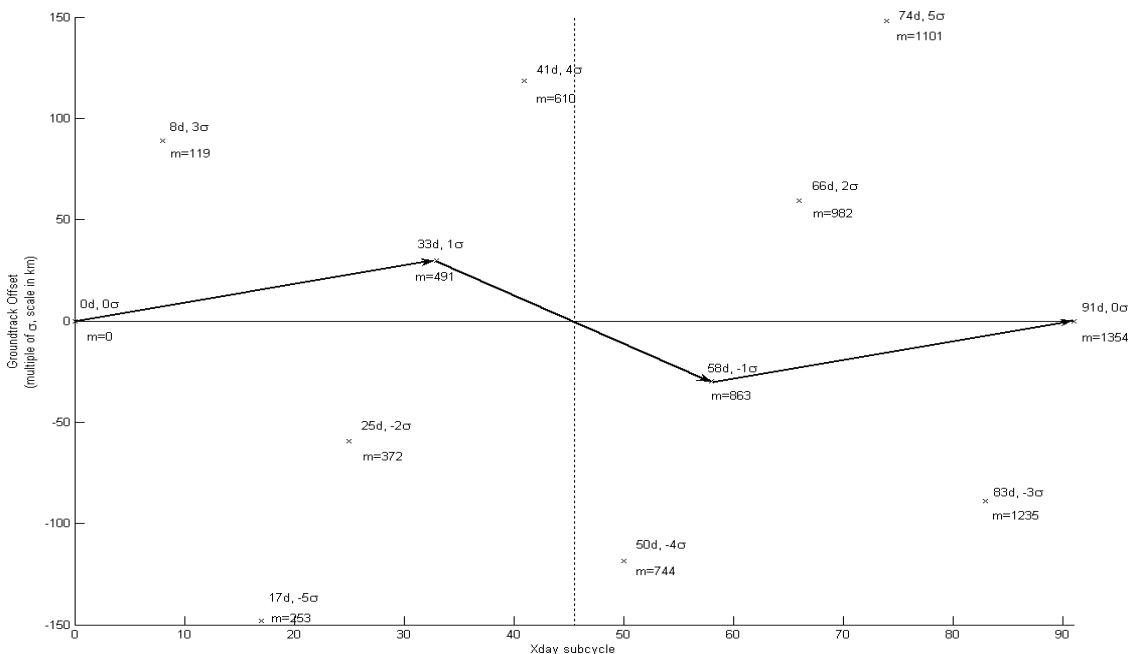


Fig. 3.13: Close-up of Fig. (3.6). Sequence of subcycles 33-25-33. The maximum offset from the reference ascending node AN_0 within this sequence is one nodal spacing.

one nodal spacing eastward. However, $MS2$ being 8 nodal days shorter than $MS1$, the groundtrack corresponding to the last 8 days of the first phase is not being duplicated. At the end of $MS2$, the satellite is over the track corresponding to the 58th day of the repeat cycle. This track is naturally located two nodal spacings west of the track corresponding to the 25th nodal day of the repeat cycle. As Fig. (3.13) shows, this track is also located one nodal spacing west of the reference track, i.e. the beginning of $MS1$. Consequently, during $MS3$, the groundtrack almost retraces the segment corresponding to $MS1$ but with an offset of one nodal spacing westward. In the end, the groundtrack corresponding to the

first 25 nodal days of the repeat cycle is nearly retraced (once eastward and once westward). The groundtrack corresponding to the following 8 nodal days (from day 25 to day 33) nearly retraced once westward.

This existence of subcycles within the ICESat 91-day repeat cycle turned out to be a very useful characteristic of the orbit in order to achieve the observation goals of the ICESat mission, given the equipment difficulties suffered by the ICESat satellite. After the launch of ICESat, the first of the three lasers failed while in the 8-day repeat orbit used for the instrumentation calibration. The defect that caused the failure was expected to exist in the remaining two lasers. An alternate operation scenario was therefore devised to allow measurements over several years to create a time series to meet the science requirements. This scenario was based on approximately 30-day operation, three times per year. The 91-day repeat cycle offers a subcycle at 33 nodal days which met this requirement. The 33-day campaigns provide a global coverage. This global coverage is less dense than the one provided by the entire 91-day repeat orbit. However, these 33-day campaigns have been the operational periods of the ICESat satellite, that is to say the periods when the laser is actually being fired.

3.5 INFLUENCE OF THE PARAMETER N

As we have seen before, a particular layout of the subcycles on the chart might be preferable to another one to achieve the scientific requirements and goals of a mission. In the case of ICESat, the values of the parameters D and N are known $\{D = 91, N = 1354\}$.

However, these parameters might not always be known or fixed to some imposed values when a study of the subcycles is being conducted as a part of the orbit design phase of a mission. For scientific purposes, it might be required to design an orbit with a specific subcycle with a specific deviation. For a fixed value of D , there is a large range of different subcycle patterns of the subcycles depending on the value of N . To illustrate this point, we give the chart of subcycles for two hypothetical ICESat orbits: one in which one satellite revolution was removed $\{D = 91, N = 1353\}$ on Fig. (3.14); a second in which a satellite revolution was added $\{D = 91, N = 1355\}$ on Fig. (3.15).

3.5.1 ICESAT-II REPEAT ORBIT

The repeat orbit for the future ICESat mission (ICESat-II) is still currently being discussed and the issue of the subcycles was raised. In order to take advantage of successes and the lessons learned during the first ICESat mission, it was suggested that this second satellite should be placed in the same repeat orbit used for ICESat so that ICESat-II would follow exactly ICESat 91-day repeat groundtrack. However, it was also suggested that ICESat-II could be put in a longer repeat orbit in order to provide a denser global coverage. In this case, the operation repeat orbit could be chosen to be the original 183-day repeat orbit described in Table (2.1) and which chart of subcycles is presented on Fig. (3.7).

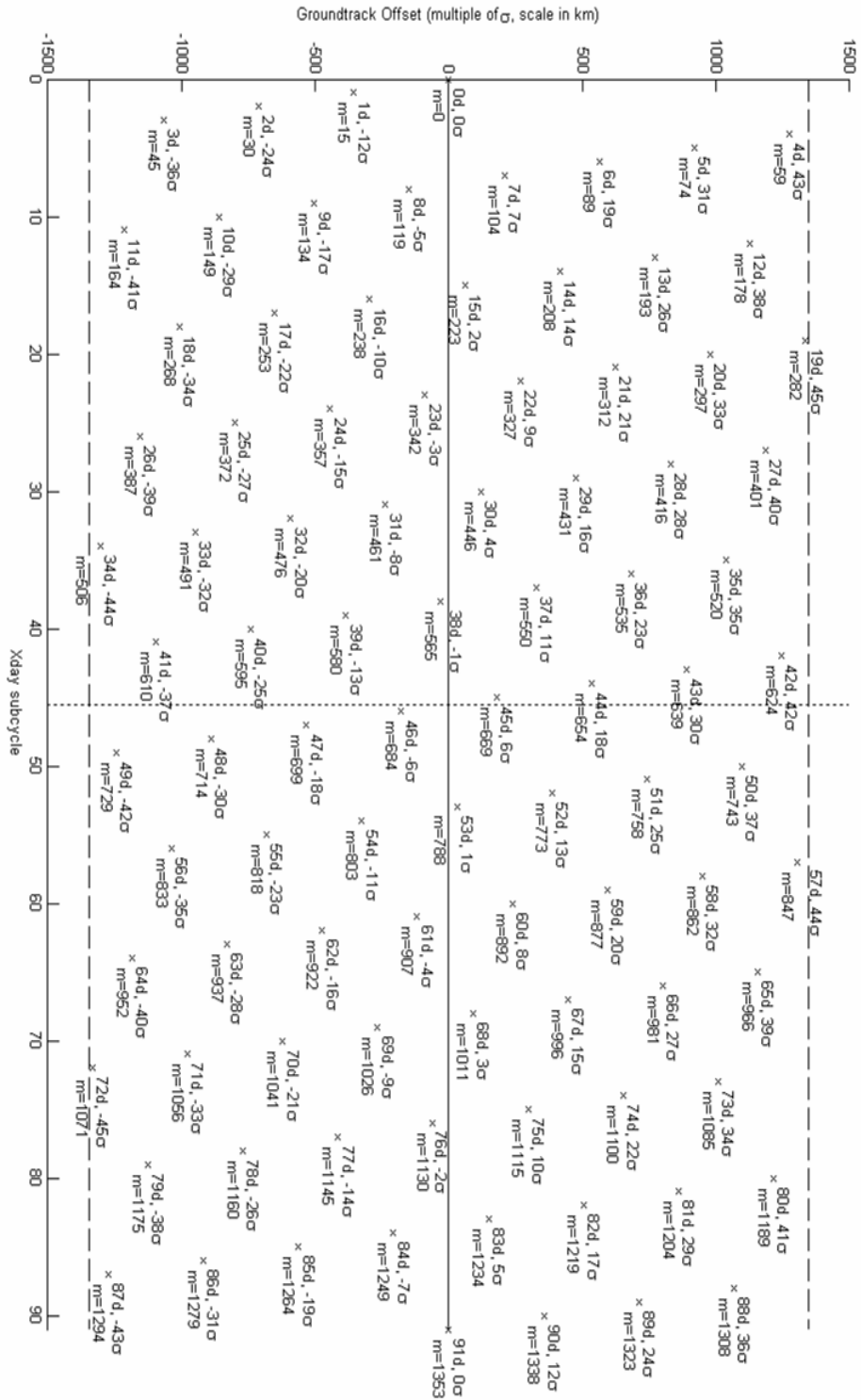


Fig. 3.14: Chart of subcycles for a 91-day repeat orbit with $N = 1353$ satellite revolutions. The subcycle sequence at $\pm 1\sigma$ is 38-15-38: MS1=38 nodal days, MS2=15 nodal days, MS3=38 nodal days.

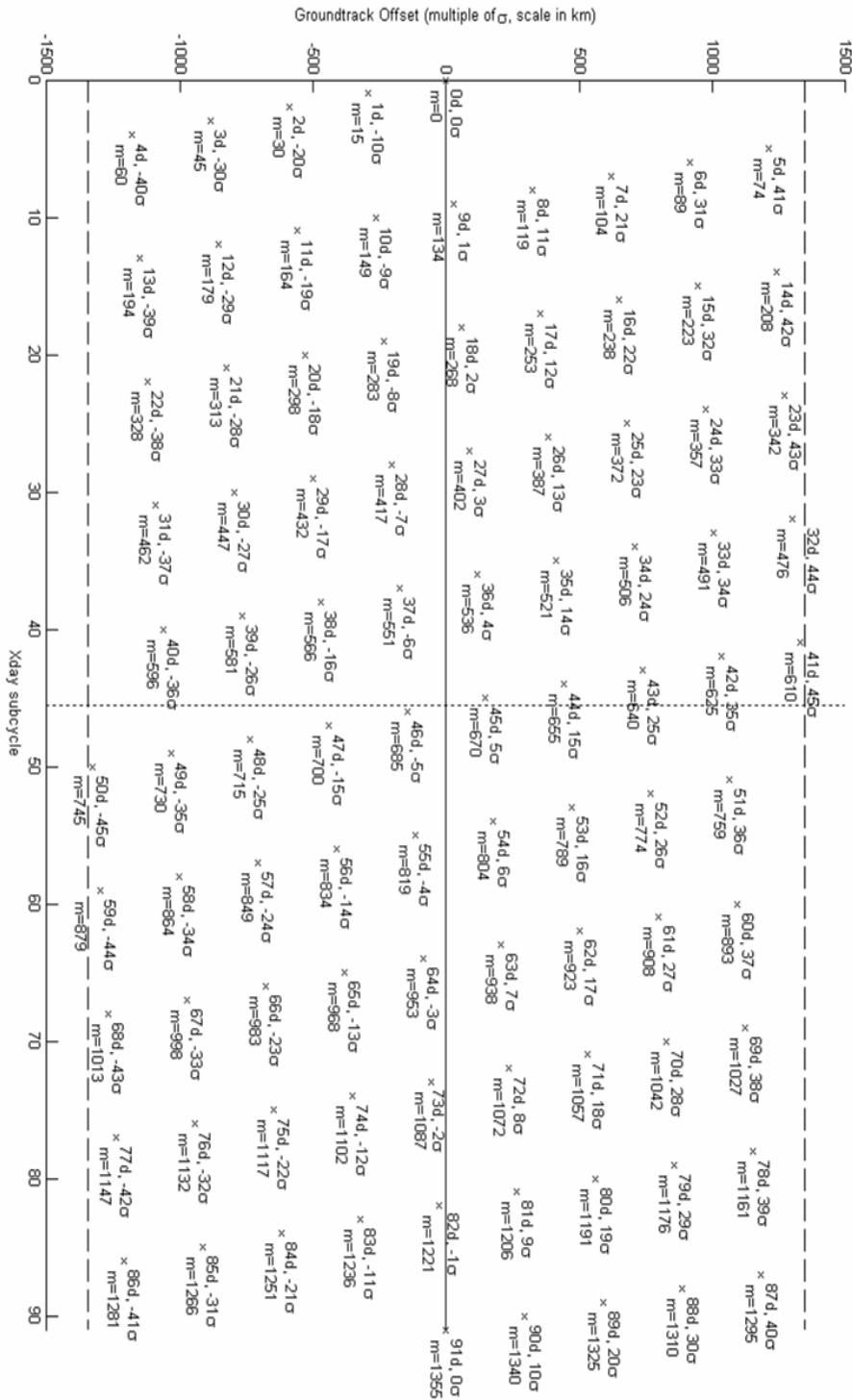


Fig. 3.15: Chart of subcycles for a 91-day repeat orbit with $N = 1355$ satellite revolutions. The subcycle sequence at $\pm 1\sigma$ is 9-73-9: MS1=9 nodal days, MS2=73 nodal days, MS3=9 nodal days.

Other considerations may result in a requirement for a lower altitude: 500km instead of 600km for ICESat. With such an orbit, the idea would be to obtain a subcycle pattern identical to Fig. (3.6) at this new altitude. This pattern can be defined by one of the subcycle, for example $(33d,+1\sigma)$. This is a direct consequence of the linearity property and the torus representation: since the distribution is a linear spiral around the torus, it is entirely defined by the slope of the spiral or, in other words, by one unique subcycle. Since the parameter N depends directly on the semi-major axis, we can expect its value to be different than 1354 as the semi-major axis varies.

3.5.2 THE BEZOUT THEOREM

To solve for the new value of N , we use the Bezout equation and then compare the resulting semi-major axis to the requirement of $a \approx 6878$ km. On one hand, the Bezout theorem (Everest and Ward, 2005) states that, given the following equation:

$$d \cdot N - m \cdot D = k \quad (3.3)$$

where d , D , and $k \neq 0$ are integers, an integer solution (N, m) exists if and only if k is a multiple of the greater common divisor of d and D . On the other hand, Lim (1995) showed that the d -day subcycle of a D -day repeat orbit that consists of N satellite revolutions has a deviation of $k\sigma$, where k satisfies the following equation:

$$d \cdot N = k \pmod{D} \quad (3.4)$$

N	a (km)	Deviation of the 33-day subcycle
...
1172	7673.4872168396405	$+1\sigma$
1194	7579.023314480136	-1σ
1263	7300.700251132113	$+1\sigma$
1285	7217.233481438066	-1σ
1354 (ICESat case)	6970.244381135064	$+1\sigma$
1376	6895.8652264702105	-1σ
1445	6674.937531969953	$+1\sigma$
...

Table 3.2: Solutions of the Bezout equation for the ICESat-II 91-day repeat orbit with a subcycle at 33 nodal days with a deviation $\pm 1\sigma$.

Equations (3.3) and (3.4) are equivalent when m is an integer. It is therefore possible to use the Bezout equation to solve for N . In the case of the ICESat-II mission with a lower altitude at 500 km, we look for a repeat orbit such that $D = 91$, $d = 33$ and $k = 1$. Since 1 is the greater common divisor of 91 and 33, the Bezout theorem confirms that an integer solution (N, m) exists. In Table (3.2), we present possible values for N and the corresponding values for the semi-major axes. We extended the search to a deviation $\pm 1\sigma$ instead of just $+1\sigma$.

Table (3.2) shows that a 91-day repeat orbit with a pattern similar to the one of ICESat orbit can be found at an altitude of approximately 518 km for $N = 1376$. However, it can be observed that the deviation of the 33-day subcycle is -1σ instead of

$+1\sigma$. This can be seen on Fig. (3.16) which shows the chart of subcycles for $D = 91$ and $N = 1376$. The distribution of the subcycles on this new chart is the similar Fig. (3.6), but *flipped* horizontally. The values of m which represents the number of satellite revolutions corresponding to each subcycle are however different since the total number of revolution is itself different. Furthermore, since $N = 1376$ for ICESat-II versus 1354 for ICESat, the new value of the nodal spacing is smaller: $\sigma = 0.26163$ degrees for ICESat-II versus 0.26588 degrees for ICESat.

Another suggested repeat orbit for the future ICESat mission was designed based solely on altitude consideration. This orbit is 91-day repeat groundtrack and consists in 1367 satellite revolutions with a semi-major axis equal to 6926 km. Using Eq. (3.3) and Eq. (3.4), we find that the subcycle at $+1\sigma$ corresponds to the values $d = 46$ and $m = 691$. The subcycle at -1σ corresponds to the values $d = 45$ and $m = 676$. Fig (3.17) shows the chart of subcycle of this particular orbit. For the readability of the chart, only the values of d (nodal days) and deviation (in term of σ) are represented on the graph. It can be observed that a few short subcycles have small deviations: the subcycle at 1 nodal day has a $+2\sigma$ deviation and the subcycle at 2 nodal days has a $+4\sigma$ deviation. However, the sequence of subcycles with deviations of $\pm 1\sigma$ is made of the three following main subcycles: 45 days, 1 day and 45 days ($45-1-45$). Depending on the mission requirement, this might not be the most adequate subcycle pattern.

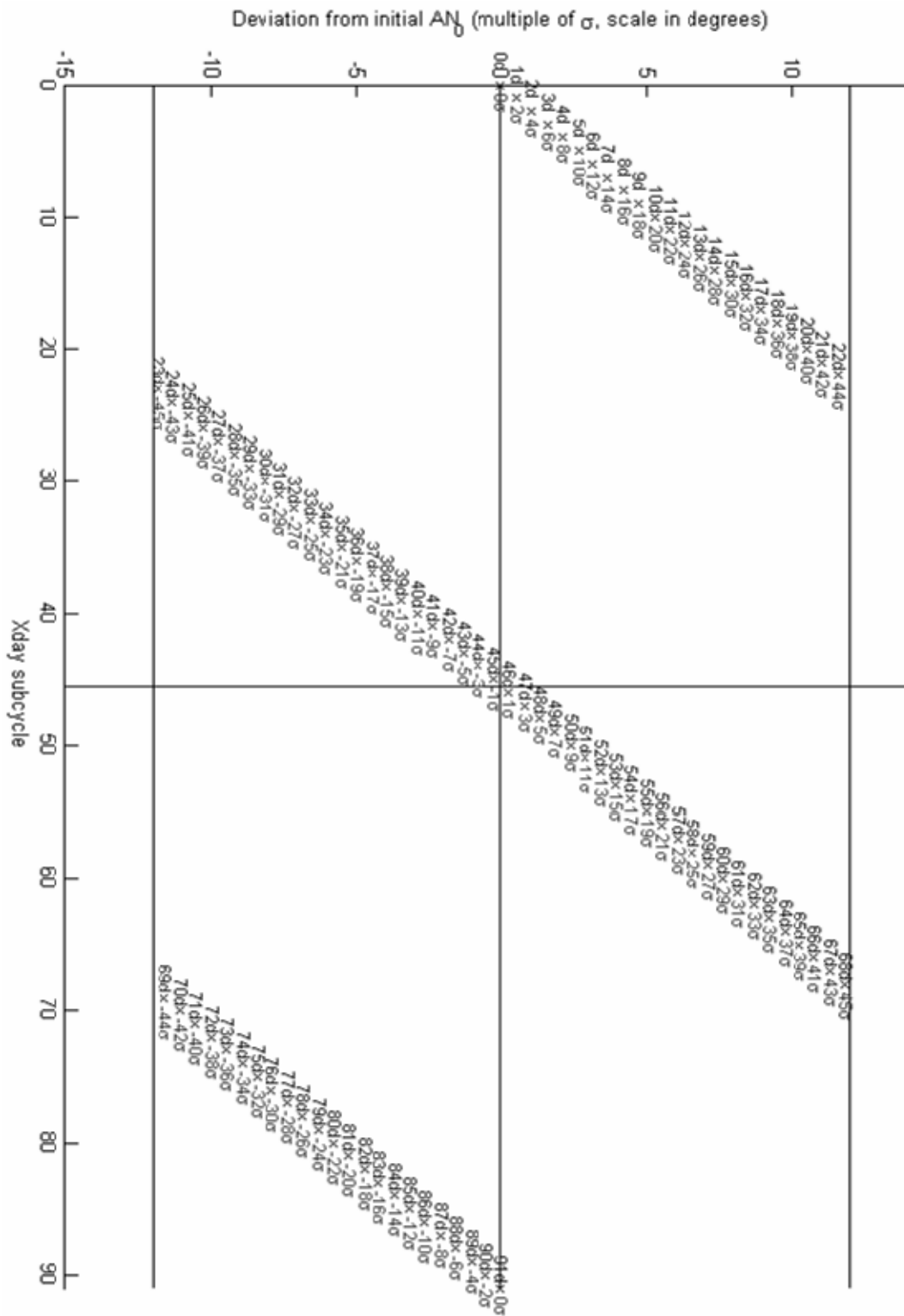


Fig. 3.17: Chart of subcycles for a future ICESat-II mission with a 91-day repeat orbit consisting in 1367 satellite revolutions.

CHAPTER 4

PHASING MANEUVERS

In the previous chapter we presented the concept subcycle of repeat orbits in the most general fashion. Though some authors would restrict their studies to the subcycles with the minimal deviation, i.e. $\pm 1\sigma$, we looked at the entire range of near-repeat tracks corresponding to an integer number of nodal days. This general approach was necessary to fully grasp the dynamic behind the concept of subcycles and will prove to be equally useful to understand the close relationship between the subcycles of a D -day repeat orbit and the shorter D' -day repeat orbits ($D' < D$) with comparable semi-major axis.

More specifically, in the case of the ICESat mission, one of these short-term repeat orbits, namely the 8-day repeat orbit presented in Table (2.1), is frequently used as a parking or transition orbit. Transferring between the 8-day and the 91-day repeat orbits proves to be a very practical way to perform some of the orbital maneuvers required in the mission to enable operation in a 33-day campaigns fashion which was designed after the failure of GLAS first laser.

The first laser to operate on board of the ICESat satellite failed after just 36 days of operation. After thorough analysis of the origin of the failure, an alternate plan was adopted in order to extend the life of the remaining three lasers. It was decided that the laser would operate in a *campaign* fashion during which the laser would be fired continuously for 33 nodal days at a time. These 33-day campaigns are being repeated three times a year, winter, summer and autumn, which allows for the observation of seasonal climate and ice mass changes. These campaigns correspond to a specific segment within the groundtrack of the 91-day repeat orbit. During each campaign, the measurements are made along the same portion of the groundtrack. However, the beginning of each campaign is calendar-specific. This could be an issue since, the adequate position of the satellite within the Earth Fixed reference frame is not guaranteed at the time of the beginning of the campaign. Rather than waiting until the next cycle which could completely violate the time requirement for the campaign, a *phasing maneuver* is applied to the satellite in order to reposition it into a different portion of the repeat cycle.

4.1 DEFINITIONS

The phasing maneuver is performed in two steps that consist in transferring into a second repeat orbit and back to the 91-day repeat orbit after the appropriate waiting time. This second repeat orbit is called a *transition orbit*. As it will be shown later in this chapter, the transfers into and out of the transition orbit have to be performed at specific

times in order to minimize the ΔV impulse required. Those times are called *transition opportunities* and depend on the transition orbit chosen.

The term *phasing maneuver* was adopted when the campaign approach was designed for the ICESat mission. Since the two orbits involved in the maneuver already corresponded to the operation *phase* and the calibration/validation *phase*, the transfer from one orbit to another was called phasing maneuver. Though this term does not reflect truly the purpose of the maneuver (outside maybe of the ICESat case), it is kept as the *de facto* term to describe the maneuver.

4.1.1 TRANSITION ORBIT

The transition orbit is a frozen repeat orbit with the same inclination and eccentricity as the one of the satellite operation repeat orbit. The semi-major axis of the transition orbit is nearly the same as the one of the operation orbit and its duration is shorter than the one of the operation orbit. In the case of the ICESat mission, the possible transition orbits are 1-day to 90-day repeat orbits with a semi-major axis approaching 6970 km. To find these repeat orbits, we use a map of resonance similar to the ones produced by Klokocnick⁽¹⁵⁾. This map is shown on Fig. (4.1). The value of the semi-major axis is given for any combination of integers N and D (i.e. the number of satellite revolutions and the number of nodal days respectively) and for all the repeat orbits shorter than 91 days with a semi major axis in the neighborhood of 6970 km. The semi-major axis is computed in a gravitational model that includes the coefficients J_2 and J_3

only, which account for most of the effects. Once the transition orbit is selected, it is necessary to recompute the semi-major axis in a more complete geopotential. This can be done using the procedures described in Chapter 2. Once the map of resonance is obtained, it is however necessary to disregard some of the repeat orbits plotted on Fig. (4.1). Indeed, if we look at the semi-major axis of the 8-day repeat with $N = 119$ we observe that other repeat orbits have the same exact semi-major axis. This is explained by the fact that the orbits $\{D=16, N=238\}$, $\{D=24, N=357\}$, and so on until $\{D=88, N=1309\}$ are all degenerate repeat orbits based on the non-degenerated repeat orbit $\{D=8, N=119\}$. This is evident since the ratios $16/238$, $24/357 \dots 88/1309$ are all reducible to $8/119$ which is itself irreducible. The resonance map in Fig. (4.1) is therefore simplified by eliminating the redundant orbits. This gives the new resonance map shown in Fig. (4.2). The transition orbit for the ICESat satellite was chosen to be the 8-day repeat with $N = 119$ satellite revolution. This orbit had already been studied by the ICESat team and had been successfully used for the calibration phase of the ICESat mission. It was therefore the natural choice when a solution had to be found to the pre-launch operations scenario. Furthermore among the orbits with the shortest repeat interval represented on Fig. 16, the 8-day repeat orbit has the semi-major axis the closest to the one of the 91-day repeat orbit. This implies that choosing an 8-day repeat orbit as a transition orbit will require less fuel than, for example, a 7-day repeat orbit.

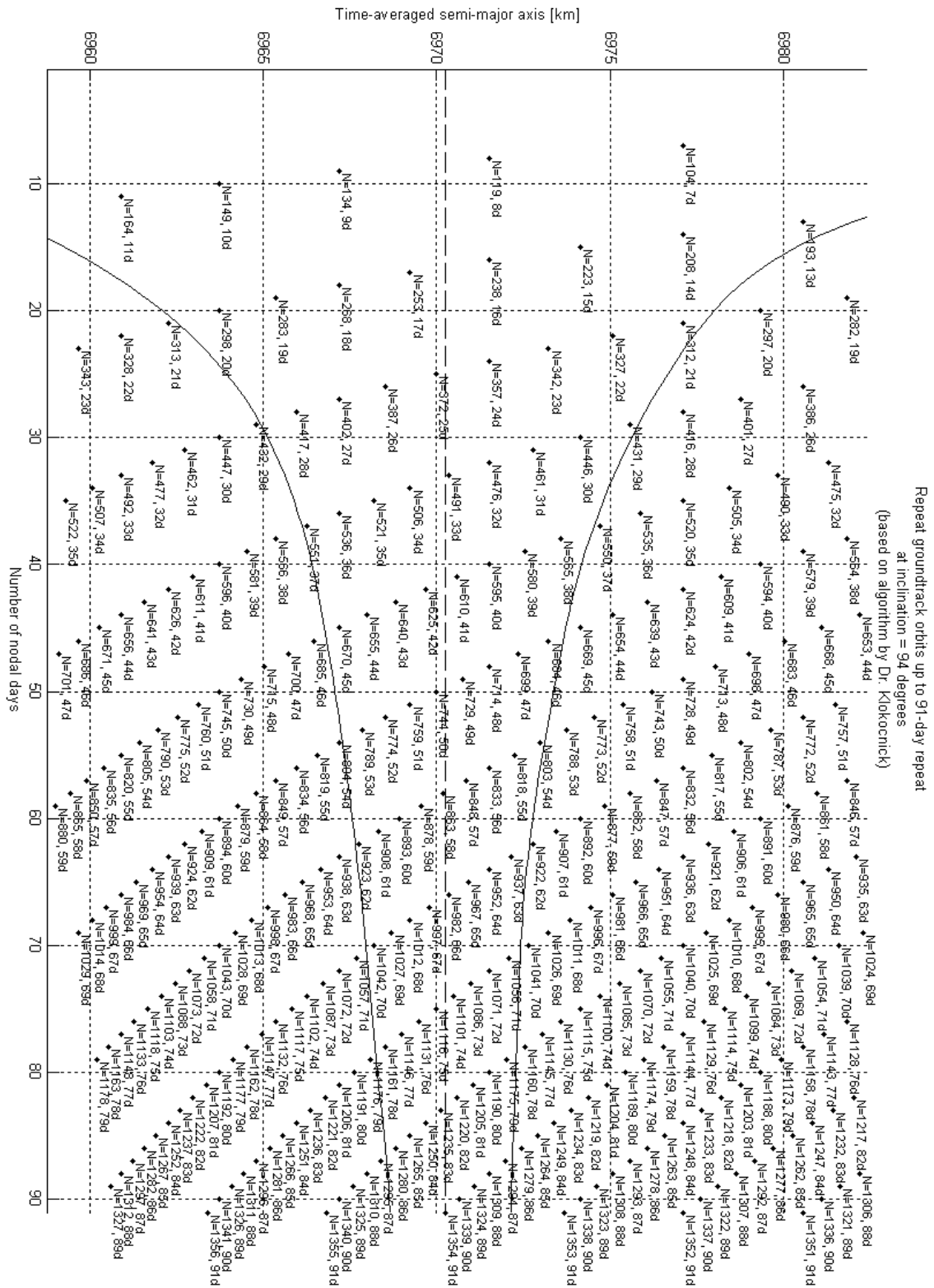


Fig. 4.1: Resonance map for 1-day to 91-day repeat orbits with a semi-major axis comparable to ICESat 91-day repeat orbit semi-major axis.

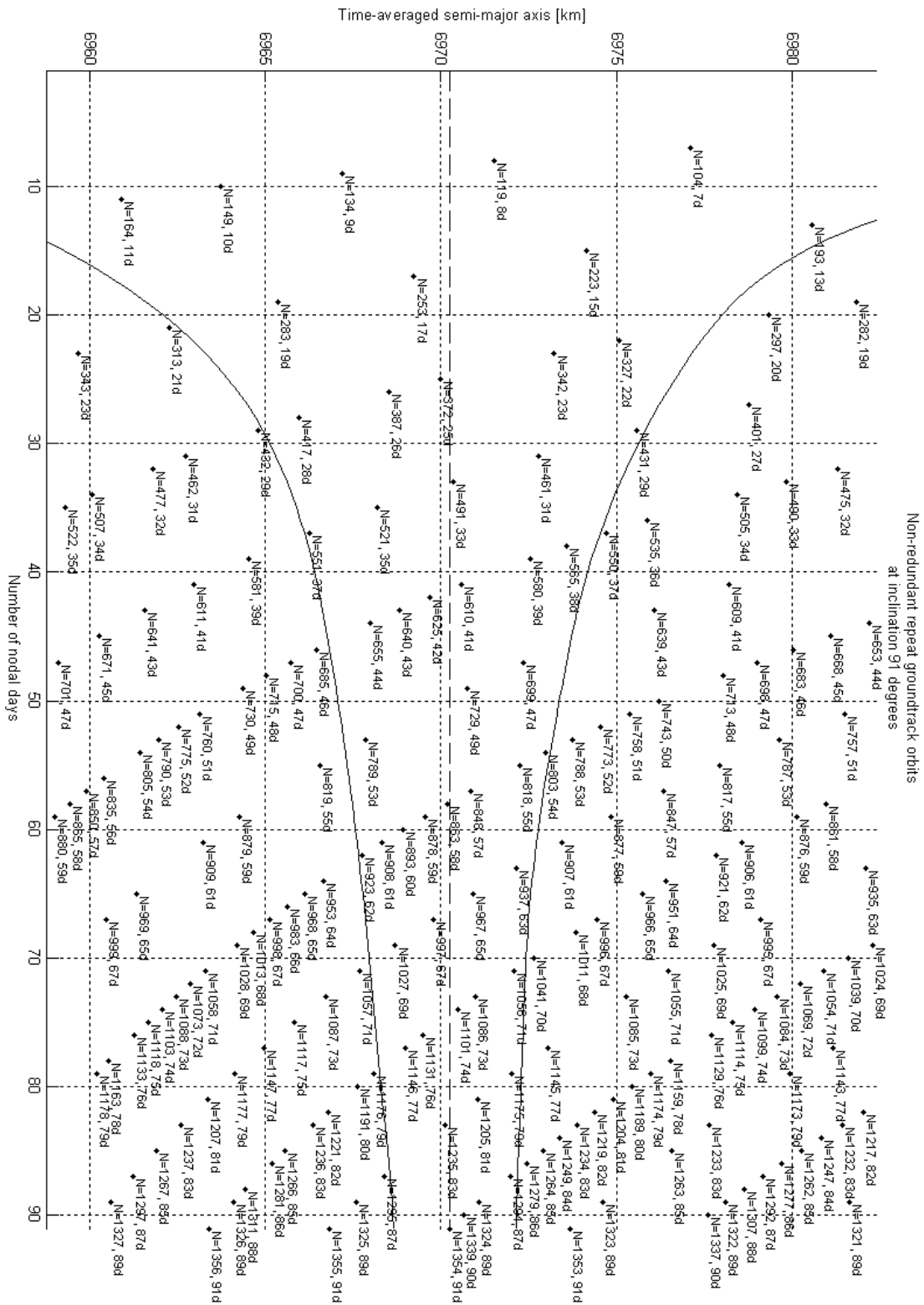


Fig. 4.2: Resonance map for 1-day to 91-day repeat orbits with redundant orbits.

A quick comparison of the resonance map before the elimination of the redundant orbits on Fig. (4.1) and the chart of subcycles for the ICESat 91-day repeat orbit on Fig. (3.6) shows a visible connection between the two graphs. To each subcycle corresponds a repeat orbit with the same number of satellite revolutions. The relative distribution of these repeat orbits with respect to the ICESat orbit on the resonance map is similar to the distribution of their respective subcycles on the chart of subcycles. The repeat orbits on Fig. (4.1) are located in an area centered on the ICESat semi-major axis and bounded by lower and upper envelopes which correspond to the lower and upper bounds on Fig. (3.6). For practical purposes, the locations of the repeat orbits at 1, 2, 3, 4, 5, 6, and 12 days are not represented on Fig. (4.1) and Fig. (4.2) since the values for the semi-major axes are too far apart to keep the graphs readable.

4.1.2 TRANSITION OPPORTUNITIES

We call transition opportunities the times at which the impulse ΔV necessary to the orbit change maneuver between the satellite's orbit and its transition orbit will be minimal. If we consider that the impulse is instantaneous, the vector ΔV is the sum of two impulse vectors: one to change the semi-major axis, a second one to change the line of node of the orbital plane. The change in semi-major axis can not be minimized since it is fixed by the choice of the transition orbit. Selecting an adequate time for the phasing maneuver can however reduce the line of node change. We call ΔAN the longitude difference in ECEF between an ascending node belonging to the groundtrack of the

transition orbit and an ascending node belonging to the ICESat groundtrack. The impulse required for the change in node which brings the satellite from one of the above ascending nodes to the other is minimized when ΔAN is a minimum. Therefore, the transition opportunities correspond to the smallest values of ΔAN .

The locations in ECEF of the ascending nodes of the transition orbit relative to the locations of the ICESat's ascending nodes can be characterized by the value of ΔAN_0 which represents the longitude difference between the reference ascending nodes of the transition orbit and the ICESat operation orbit. For each orbit, the reference ascending node is nothing more than one ascending node arbitrarily picked to represent the beginning of a repeat cycle. In the case of ICESat, the following ascending nodes were chosen to represent the beginnings of the 8-day and 91-day repeat cycles. As shown on Fig. (3.1) and Fig. (3.2), The reference ascending nodes are $(AN_0)_{8\text{-day}} = 40.555^\circ$ and $(AN_0)_{91\text{-day}} = 62.948^\circ$. We then proceeded to compare the longitude of each ascending node of the transition orbit to all the ascending nodes of the ICESat 91-day orbit. This enables us to identify the pairs of ascending nodes $(AN_{8\text{-day}}, AN_{91\text{-day}})$ for which ΔAN is minimal or within an acceptable range for the orbit change maneuver. To illustrate our point better, we decided to consider in this study all the pairs of ascending nodes that lie within 4 km of each other at the equator. The ICESat mission requirements actually set this criterion to 800 meters.

For each pair identified, we compute the time corresponding to the two ascending nodes. These times are computed in nodal days and represent the time elapsed since the

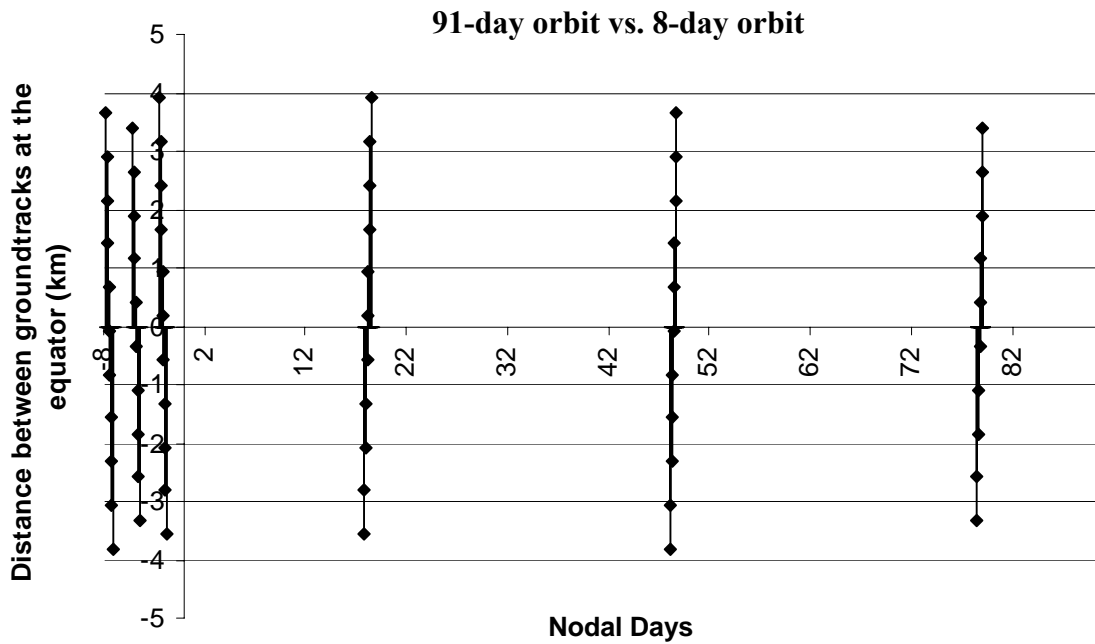


Fig. 4.3: Longitudes of the 91-day orbit’s ascending nodes compared to the longitudes of the 8-day repeat orbit’s ascending nodes. The results are shown using the distance between the nodes at the equator rather than the longitude difference. The ICESat mission requirements set the maximum admissible distance to 800 meters

beginning of the repeat cycle. It is important to remember that since the duration of one nodal day is orbit-dependent, the times of the ascending nodes are computed on two different scales depending on which repeat cycle they belong to. On Fig. (4.3), we show the distance between the two ascending nodes of each pair identified and the time corresponding to the ascending nodes. The positive part of the X-axis represents the time corresponding to the ascending nodes of the 91-day orbit. The negative part of the X-axis represents the time corresponding to the ascending nodes of the 8-day orbit. Therefore, for each pair of ascending nodes, the distance that separates them appears twice on the graph: once on the positive side and once on the negative side.

	8-day repeat orbit (transition orbit)		91-day repeat orbit (operation orbit)		Longitude difference at equator (deg)	Distance at equator (km)
	Track number	Time (nodal days)	Track number	Time (nodal days)		
Opportunity 1	60	2.118	194	18.146	$1.55 \cdot 10^{-3}$	0.172
Opportunity 2	20	7.428	645	48.457	$6.8 \cdot 10^{-4}$	0.075
Opportunity 3	99	4.739	1096	78.768	$3.08 \cdot 10^{-3}$	0.343

Table 4.1: Transition opportunities between the 8 day and the 91-day repeat orbits.

On both sides of the X-axis, we observe that the transition opportunities are almost lined up along three central values. Which means that we have three opportunities to transfer inexpensively from the 91-day repeat orbit to the 8-day repeat orbit, or from the 8-day repeat orbit to the 91-day repeat orbit. Using the double occurrence of the distance value on both the negative and positive sides of the X-axis, we also observe that the opportunities that occur at 18.1, 48.5 and 78.8 nodal days in the 91-day repeat cycle correspond respectively to 2.1, 7.4 and 4.7 nodal days in the 8-day repeat cycle. The values corresponding to each transition opportunity are summarized in Table (4.1).

On a practical point of view, this means that transferring from the 91-day orbit to the 8-day orbit at an epoch that correspond to 18.1 nodal days into the 91-day repeat cycle places the ICESat satellite in the 8-day orbit at a location that corresponds to 2.1 nodal days into the 8-day repeat cycle. Once in the transition orbit, let's suppose that the satellite remains in the 8-day orbit until it reaches the location that corresponds to 4.7

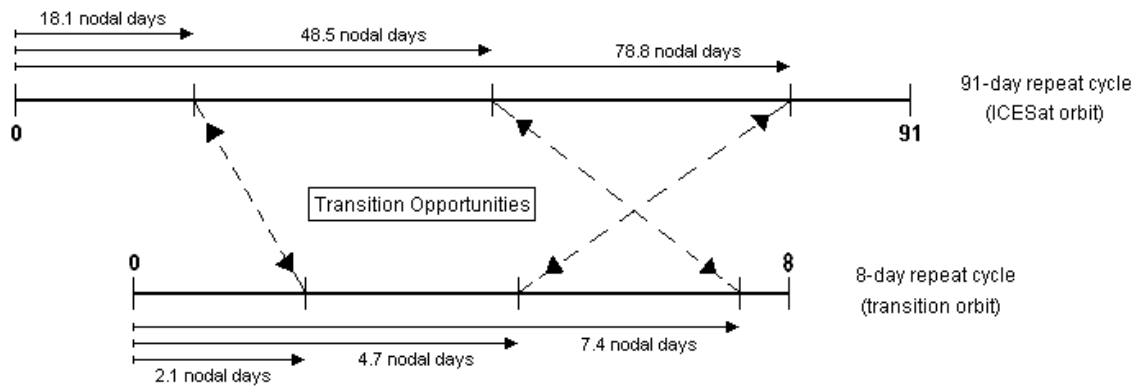


Fig. 4.4: Correspondence of the transition opportunities between the 8-day and the 91-day repeat orbits.

nodal days, which corresponds to a transition of 2.6 nodal days. A transfer back to the 91-day orbit at this epoch places the satellite at a location that corresponds to 78.8 nodal days into the 91-day repeat cycle. Therefore by waiting 2.6 nodal days in the 8-day orbit, the satellite can therefore *jump* 60.7 nodal days ahead into the 91-day repeat cycle. The diagram on Fig. (4.4) summarizes this idea.

Due to the time required for the data analysis after the first transfer to the transition orbit, or just in order to wait for the adequate time imposed by the calendar constraint of the 33-day campaign, it might not be realistic to plan a jump back into the 91-day orbit after only a couple of nodal days in the transition orbit. ICESat usually stays park in the 8-day orbit until all the data has been processed or until the time constraint is met. At that point, there is no more than 8 nodal days to wait until the desired transition opportunity, time at which the satellite is transferred back to the 91-day repeat orbit.

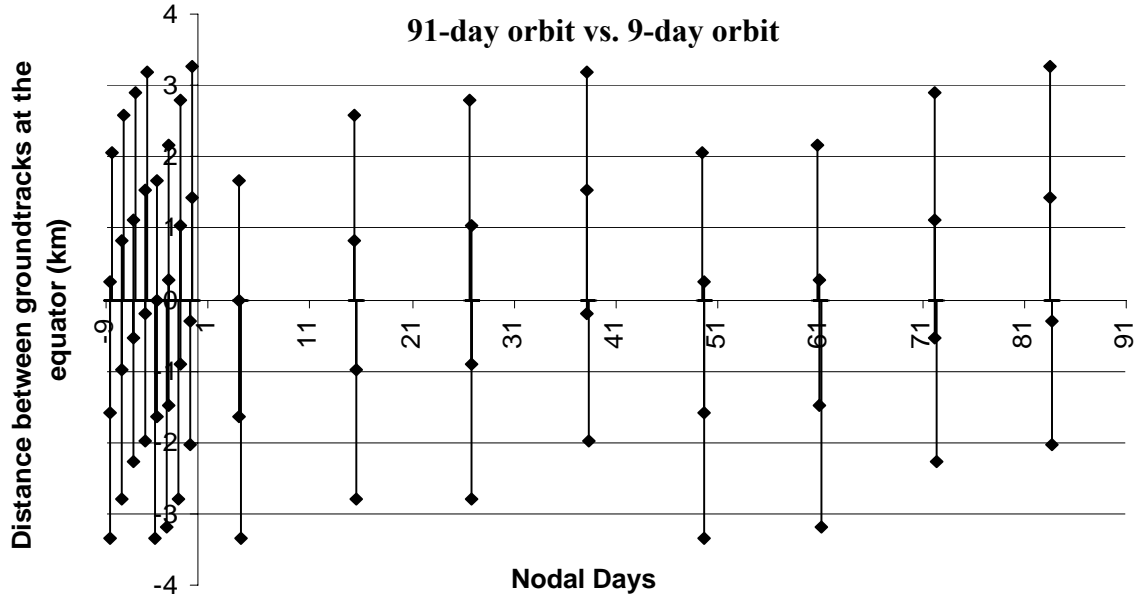


Fig. 4.5: Longitudes of the 91-day orbit's ascending nodes compared to the longitudes of the 9-day repeat orbit's ascending nodes.

4.2 NUMBER OF TRANSITION OPPORTUNITIES

It appears that the number of transition opportunities is related to the deviation of the subcycle corresponding to the transition orbit. In our case, we are considering an 8-day repeat orbit with 119 satellite revolutions which offers three transition opportunities. Its corresponding subcycle in the 91-day repeat cycle has a deviation of $+3\sigma$ as shown on Fig. (3.6). This correspondence between the number of transition opportunities and the deviation of the subcycle from which the transition orbit is derived can be observed for all the non-degenerated short-term repeat orbits shown on Fig (4.2).

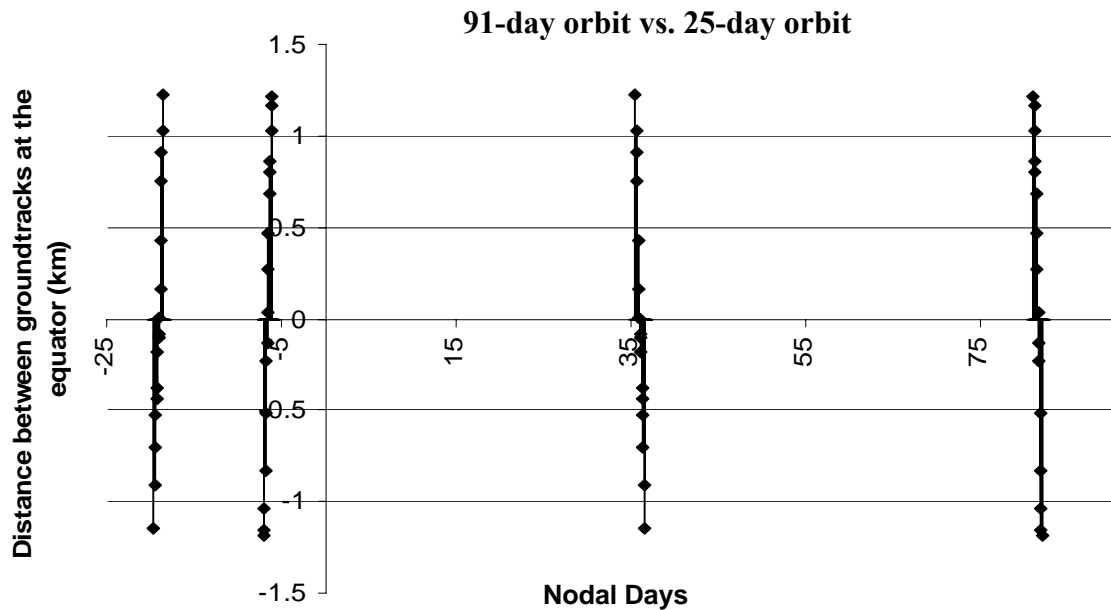


Fig. 4.6: Longitudes of the 91-day orbit’s ascending nodes compared to the longitudes of the 25-day repeat orbit’s ascending nodes.

On Fig (4.5) to Fig. (4.7), the results are shown for three repeat orbits that could have just as well been used as transition orbits for the ICESat mission: 9-day, 25-day and 58-day repeat orbits. The 9-day repeat orbit is made of 134 satellite revolutions as can be read on Fig. (4.2). Its corresponding subcycle has a deviation of -8σ . The graph of the transition opportunities between the 91-day and the 9-day repeat orbits on Fig. (4.5) shows eight transition opportunities at 4, 15.4, 26.8, 38.2, 49.5, 60.9, 72.3 and 83.7 nodal days into the 91-day repeat cycle. As for the 25-day repeat orbit ($N=372$), the distances at the equator between its ascending nodes and the ones of the 91-day repeat orbit are shown on Fig. (4.6). It can be observed that there exist two transition opportunities at 36 and 81.5 nodal days into the 91 day repeat cycle. Consistently, Fig (3.6) shows that the 25-day subcycle corresponds to a deviation of -2σ .

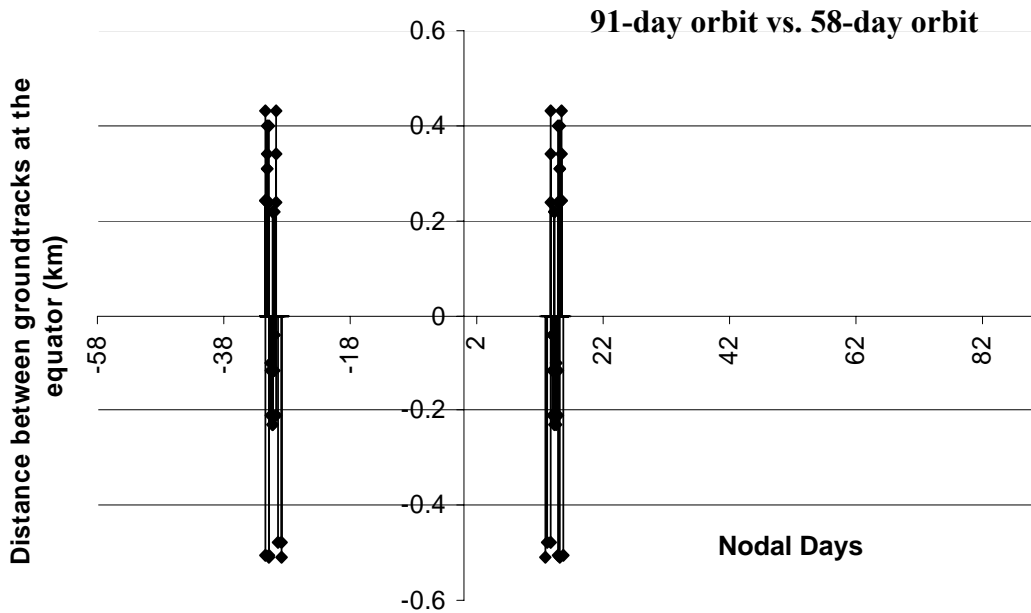


Fig. 4.7: Longitudes of the 91-day orbit’s ascending nodes compared to the longitudes of the 58-day repeat orbit’s ascending nodes.

It is interesting to look at the phasing between the 91-day and the 58-day repeat orbits. Indeed, the 58-day subcycle shows a deviation of -1σ . We observe only one transition opportunity on Fig. (4.7). This means that transferring to the 58-day orbit and back using the transition opportunity would send the satellite back to the exact same position where it left off the 91-day orbit. Transferring into the 58-day repeat orbit could be seen as *pausing* the progression of the 91-day repeat cycle. In the case of ICESat 91-day repeat cycle, it is not an interesting option since the transition orbit would have such a long repeat cycle and one would need to wait at least 58 nodal days before transferring back to the 91-day. We can however envisage some long repeat orbits containing a short subcycle with a deviation of $\pm 1\sigma$. For example, on Fig. (3.16) we considered a hypothetical orbit for the ICESat 91-day orbit with $N = 1355$. This hypothetical orbit has

a subcycle at 9 nodal days with a deviation of $+1\sigma$. This means that there would be only one transition opportunity between this hypothetical orbit and the 9-day repeat orbit. However, the waiting time to transfer back to the 91-day orbit would be only 9 nodal days. Or, the satellite could remain parked into this transition orbit with an opportunity every 9 days to resume its progression into its operation orbit.

4.3 ADVANTAGES

The ICESat satellite is being regularly repositioned in a different location of its orbit via phasing maneuvers. Each time, the transfers in and out of the transition orbit occurred at a time corresponding to one of the same three transition opportunities described in Table (4.1) and Fig (4.4). Therefore in the case of the ICESat 91-day repeat orbit and an 8-day repeat transition orbit, the six maneuvers corresponding to the three possible transfers into the transition orbit and the three possible transfers out of the transition orbit are the only maneuvers that have to be designed. This simplifies greatly the analytical work that precedes any in-flight maneuver. Indeed, if the satellite was repositioned at anytime of the repeat cycle via a *direct* maneuver which would consist in a change of its orbit plane's line of node, the maneuver would have to be recomputed each time.

A second and more important advantage is the fuel efficiency of the phasing maneuver compared to a more direct approach. As described earlier, the impulse for the first step of the phasing maneuver is the sum of an impulse to change the line of node and

an impulse to change the semi-major axis. A second maneuver is then necessary to go back into the ICESat orbit. On the other hand, only one impulse is required for a direct maneuver to change the line of node. This last impulse is computed as follows:

$$\Delta V_{\Omega} = 2V \sin i \sin \frac{\Delta\Omega}{2} \quad (4.1)$$

with i the inclination and $\Delta\Omega$ the line of node change. For the purpose of this particular discussion we neglect the eccentricity of the orbit and the variations of the other orbital elements. Consequently, we can approximate the actual velocity of the satellite V in the 91-day repeat orbit to the velocity of the satellite if it was in a circular Keplerian orbit:

$$\Delta V_{\Omega} = 2(na)_{91\text{-day}} \sin i \sin \frac{\Delta\Omega}{2} \quad (4.2)$$

with n the mean motion of the satellite and a the mean semi-major axis of the ICESat 91-day repeat orbit.

In the case of the phasing maneuver, the impulse required to change only the line of node can also be obtained using Eq. 10. The impulse required to change only the semi-major axis is equal to ΔV_a . The magnitude of the vector resulting from the sum of the two impulses previously mentioned corresponds to the total impulse for the transfer from the 91-day repeat orbit to the 8-day repeat orbit. The magnitude of the total impulse is equal to:

$$\Delta V_1 = \sqrt{\Delta V_{\Omega_1}^2 + \Delta V_a^2 - 2\Delta V_{\Omega_1}\Delta V_a \sin i \sin \frac{\Delta\Omega_1}{2}} \quad (4.3)$$

$$\text{where } \Delta V_a = (na)_{8\text{-day}} - (na)_{91\text{-day}} \quad (4.4)$$

with ΔV_{Ω_1} is given by Eq. (4.2) and $\Delta\Omega_1$ is the difference of line of node between the 91-day and the 8-day repeat orbits. The second impulse ΔV_2 is obtained by substituting $\Delta\Omega_2$ to $\Delta\Omega_1$ in Eq. (4.3). The total fuel cost for the phasing maneuver is $\Delta V_{total} = \Delta V_1 + \Delta V_2$. The impulse corresponding to the phasing and the direct maneuvers are plotted on Fig. (4.8). In order to simplify the plot to a 2-dimensional graph, $\Delta\Omega_1$ is set to be equal to $\Delta\Omega_2$.

For any value of $\Delta\Omega$, we observe that the impulse required for a phasing maneuver is greater than the one required for a direct maneuver. However, two major considerations must be made. First, a direct maneuver repositions the satellite into the same 91-day repeat orbit: the maneuver would consist in *jumping* from one track to another. Consequently $\Delta\Omega$ is a multiple of the nodal spacing σ , which is equal to 0.266 degree. Secondly, the two transfers of the phasing maneuver occurs at times corresponding to transition opportunities, that is to say when the longitude difference between the track belonging to the 8-day repeat orbit and the track belonging to the 91-day repeat orbit is minimal. At a transition opportunity, the maximum longitude difference between tracks is $3.08 \cdot 10^{-3}$ degree as summarized in Table (4.1). Fig. (4.9) is a close-up of Fig. (4.8) around the origin of the graph.

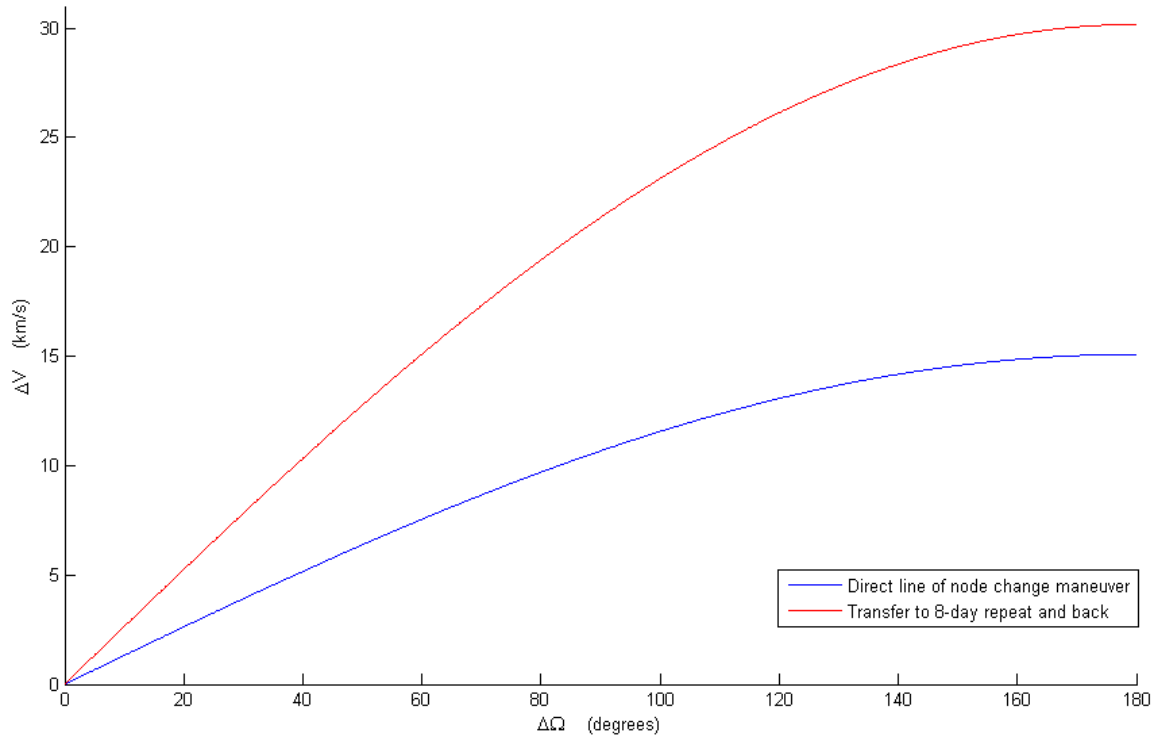


Fig. 4.8: Fuel cost for a direct maneuver and a phasing maneuver between the 91-day repeat orbit and the 8-day repeat orbit.

On one hand, the minimum impulse for a direct maneuver corresponds to the impulse required to perform a line of node change equal to one nodal spacing: $\Delta V = 3.503 \cdot 10^{-2}$ km/s. On the other hand, the maximum impulse for a phasing maneuver corresponds to the two transition opportunities where $\Delta\Omega_1 = \Delta\Omega_2 = 3.08 \cdot 10^{-3}$ degree. In this case, the impulse is 22 times smaller than the impulse corresponding to a direct maneuver: $\Delta V = 1.612 \cdot 10^{-3}$ km/s.

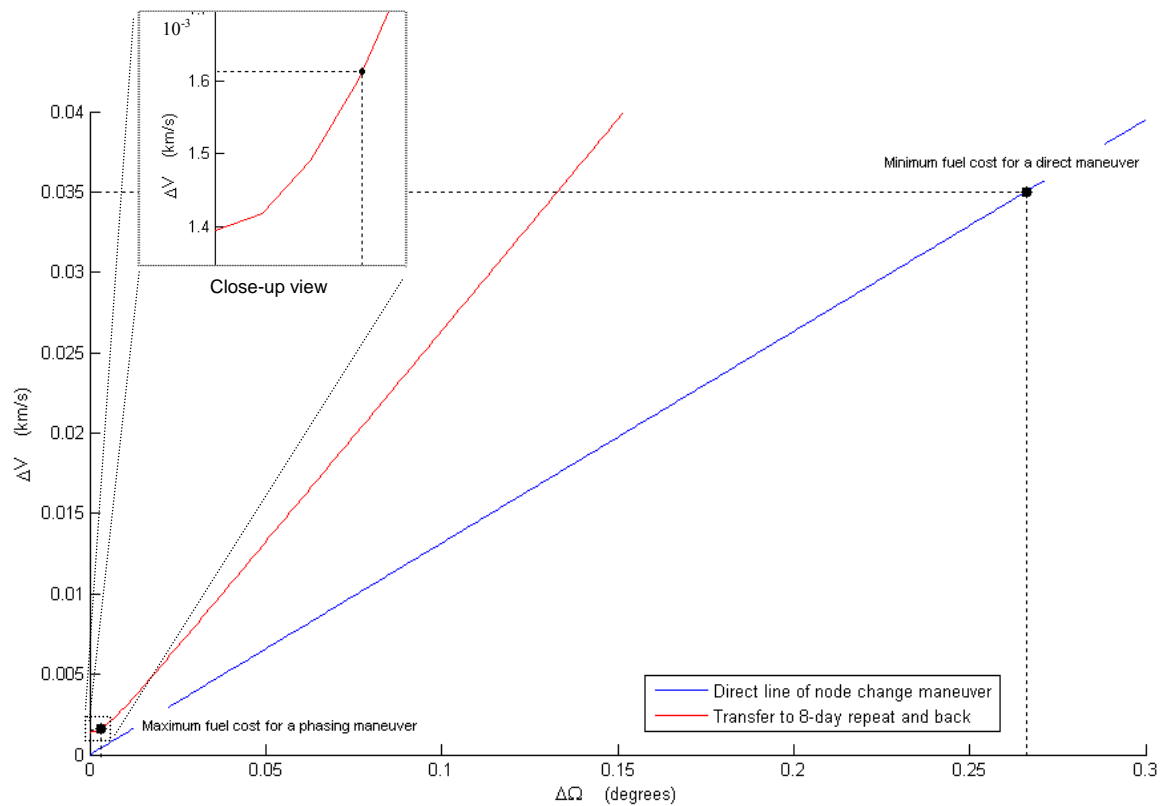


Fig. 4.9: Comparison between the minimum fuel cost for a direct maneuver and the maximum fuel cost for a phasing maneuver between the 91-day repeat orbit and the 8-day repeat orbit. The close-up view shows the fuel cost of a phasing rbit for the smallest value of $\Delta\Omega$. For $\Delta\Omega = 0$, the phasing maneuver consists in two Hohman transfers.

In practice, the change in line of node is not accounted for during the phasing maneuver due to the small values of $\Delta\Omega_2$ and $\Delta\Omega_1$. The small East/West error due to this simplification of the maneuver is accounted for during the regular corrective maneuvers performed by the ICESat satellite in order to compensate for the East/west drift of the orbit due mainly to the effect of the drag. However, Fig (4.8) and Fig (4.9) show that for larger values of $\Delta\Omega_2$ and $\Delta\Omega_1$ it becomes necessary to take the change in line of node into

account. As we just mentioned, the phasing maneuvers between ICESat 91-day operation orbit and its 8-day transition orbit does not account for the line of node change. The phasing maneuver consists therefore in two Hohman transfers from the operation orbit to the transition orbit and back. For each of the two transfers, two impulse burns are applied: one at the beginning of the transfer to leave the first orbit, the second at the end of the transfer to adjust the satellite velocity to the targeted orbit. In the case of ICESat, each impulse accounts for 0.35 m/s. To complete the phasing maneuver, four impulses are required which bring the total fuel cost of the maneuver to 1.4 m/s as can be verified on the close-up view of Fig (4.9) when $\Delta\Omega = 0$.

CHAPTER 5

CROSSOVERS

The CryoSat mission was approved in 1999 as part of the ESA Living Planet Program (ESA, 2003). Its purpose was very similar to some of ICESat mission goals. The CryoSat satellite was designed to make measurements of the thickness of the floating sea ice and the elevation of the ice sheets in the Polar Regions. Ultimately, the purpose of the CryoSat mission was to help to understand the influence of the global warming effect on the polar ice caps. The measurements were to be made by the on-board SIRAL radar altimeter operating in Synthetic Aperture Radar mode (SAR). The satellite was design to fly for a period of three years. The CryoSat orbit was designed to support the sole purpose of the mission, monitoring the changes in the sea ice thickness and the ice sheets elevation over Antarctica and Greenland. It was decided by ESA that the satellite would be placed into a non Sun-synchronous 369-day repeat groundtrack orbit to meet the science requirements, with an altitude of 717 km and a near-polar inclination. CryoSat was designed to fly at an inclination of 92° in order to provide a coverage that would satisfy the mission requirements in terms of crossover and latitude limit. This inclination

was a compromise to a polar orbit which would not have allowed a high density of crossover measurements over the polar regions. Indeed, the elevation measurements are made at the crossover locations, i.e. the intersection of an ascending track with a descending track. In the case of a polar orbit, the tracks would be parallel to the Earth meridians if it wasn't for the rotation of the Earth. The meridians intersect only at the poles. Therefore in the case of a polar orbit, the crossovers are due solely to the Earth rotation and are consequently too few to ensure a sufficient coverage of a region that is not in close vicinity to the pole, like Greenland.

As part of the calibration phase of the CryoSat mission, it was apparent that ICESat could provide opportunities to compare altitude measurements obtained by ICESat to the ones obtained by CryoSat. To implement this cross-validation, it is necessary that the altitude measurements obtained by each satellite be made over the exact same geographic location. In other words, the cross-validation measurements are made at the intersection of an ICESat track and a CryoSat track. Using ICESat's off-nadir capability, its laser can point at the locations along the CryoSat's track rather than its own. Cross-validation is a concept that has been used in the past: for example, in the case of Jason-1 and TOPEX, the ERS satellites or ENVISAT and ERS (Beneviste, 2000). However, in the three cases cited above, the satellites were required to fly in a tandem formation, i.e. in comparable orbits: same orbital elements except for the line of node of the orbit plane. The line of node is designed such that the two satellites involved in the cross-validation are flying exactly above the same groundtrack. The advantage of ICESat off-nadir capability is that CryoSat was not required to fly over ICESat's groundtrack, which would not have been

possible considering the 27 km difference between the two satellites' semi-major axes and consequently the difference in their orbital periods and groundtracks.

To perform the rotation of the laser on ICESat, it is necessary to know two things. First, the locations of the intersections between the ICESat groundtrack and the CryoSat groundtrack need to be determined. Though the theory on the location of crossovers between two different orbits has not been overly studied, a theoretical framework was developed for the in-depth analysis of the crossovers between the GEOSAT, ERS-1 and TOPEX/POSEIDON orbits (Kim, 1997). The second essential parameter to be computed is the angle between the two intersecting tracks. When designing the off-nadir pointing rotation maneuver, it is necessary to allow some time for ICESat's laser to be aligned with CryoSat groundtrack. ICESat' laser then *follows* Cryosat's groundtrack for a short amount of time before and after the crossover and finally come back to its nadir pointing position. Similar maneuvers have already been performed numerous times during the ICESat mission to point the laser at *Targets Of Opportunity*, or TOO (Webb et al., 2006). Indeed, though ICESat measurements are now mainly obtained when flying in its 91-day repeat groundtrack orbit, a lot of valuable data was collected when it was flying in its 8-day repeat groundtrack calibration orbit. The off-nadir capability of ICESat's laser has been used to point at the tracks of the 8-day orbit from the 91-day repeat orbit. However in this case the orbital inclination of the two orbits is the same, so the respective tracks are parallel.

The rotation maneuvers described above are designed at the Laboratory for Atmospheric and Space Physics (LASP) at the University of Colorado at Boulder. The rotation maneuvers are simulated to test for their feasibility as they shouldn't force the satellite to go in its built-in *Safe-Hold* mode. Among other situations, the switch to the Safe-Hold mode could happen if the rotation angle is above the limitation of the instrumentation, if the acceleration rate is too high or if the position of the GLAS telescope with respect to the Sun is critical. Unfortunately, the launch of CryoSat ended in a failure on October 8th 2005 due to an anomaly in the launch sequence. However, the work done on the crossover between ICESat and CryoSat groundtracks is still relevant as it can be applied to other missions, and maybe even applied to ICESat and CryoSat-2 which is scheduled to launch by the end of the year 2009.

5.1 CROSSOVER LOCATION BETWEEN TWO ORBITS

5.1.1 IMPLICIT FUNCTION

Given two satellites in two different orbits around one main body with different semi-major axes, eccentricities and inclinations, we are first interested in finding the location of the crossover between two of their tracks, that is to say where the groundtracks of the two satellites intersect. In a second part and after obtaining the latitude and longitude at the crossover, we will compute the angle between the two tracks at the location of the crossover. For each satellite, we define its position vector as follows, where $\hat{\varepsilon}_r$ and $\hat{\varepsilon}_r'$ are unit vectors pointing from the Earth center to the satellites:

$$\vec{r} = r \cdot \hat{\varepsilon}_r \quad (5.1)$$

$$\vec{r}' = r' \cdot \hat{\varepsilon}_r' \quad (5.2)$$

In an Earth Centered Earth Fixed (ECEF) reference frame defined by the unit vectors $(\hat{\varepsilon}_1, \hat{\varepsilon}_2, \hat{\varepsilon}_3)$, the unit vector $\hat{\varepsilon}_r$ can be expressed in terms of the longitude, λ , and the latitude, φ , of the satellite in ECEF:

$$\hat{\varepsilon}_r = \cos \varphi \cos \lambda \cdot \hat{\varepsilon}_1 + \cos \varphi \sin \lambda \cdot \hat{\varepsilon}_2 + \sin \varphi \cdot \hat{\varepsilon}_3 \quad (5.3)$$

where $\hat{\varepsilon}_1$ is in the equatorial plane and in the direction of the Greenwich meridian, $\hat{\varepsilon}_3$ is perpendicular to the equatorial plane pointing North, $\hat{\varepsilon}_2$ completes the orthogonal direct-oriented triplet. In this first section, we are looking for the location of the crossovers of the two satellites' groundtracks knowing the characteristics of the two orbits and the longitudes of the equatorial crossings. The intersection occurs when the longitudes and latitudes of the two satellites are respectively equal. This condition is equivalent to $\hat{\varepsilon}_r = \hat{\varepsilon}_r'$. Unfortunately, the expression using the longitudes and latitudes of the satellites is not useful to find a general solution to the location of the crossovers. Therefore, we express $\hat{\varepsilon}_r$ and $\hat{\varepsilon}_r'$ in terms of the mean orbital elements:

$$\hat{\varepsilon}_r = [\hat{\varepsilon}_1 \quad \hat{\varepsilon}_2 \quad \hat{\varepsilon}_3] \cdot \begin{pmatrix} \cos \lambda_\Omega & -\sin \lambda_\Omega & 0 \\ \sin \lambda_\Omega & \cos \lambda_\Omega & 0 \\ 0 & 0 & 1 \end{pmatrix} \begin{bmatrix} \cos(\nu + \omega) \\ \sin(\nu + \omega) \cos i \\ \sin(\nu + \omega) \sin i \end{bmatrix} \quad (5.4)$$

$$\hat{\varepsilon}_r' = [\hat{\varepsilon}_1 \quad \hat{\varepsilon}_2 \quad \hat{\varepsilon}_3] \cdot \left(\begin{bmatrix} \cos \lambda_{\Omega'} & -\sin \lambda_{\Omega'} & 0 \\ \sin \lambda_{\Omega'} & \cos \lambda_{\Omega'} & 0 \\ 0 & 0 & 1 \end{bmatrix} \begin{bmatrix} \cos(\nu'+\omega') \\ \sin(\nu'+\omega') \cos i' \\ \sin(\nu'+\omega') \sin i' \end{bmatrix} \right) \quad (5.5)$$

with the true anomalies ν and ν' , the arguments of perigees ω and ω' , the inclinations i and i' and the longitudes of the nodes λ_{Ω} and $\lambda_{\Omega'}$ in ECEF. The longitudes of nodes are not orbital elements per se, but they are the equivalent of the arguments of the nodes (or Right Ascension of the Ascending Node, RAAN) in the ECEF rotating frame. In other words, the longitudes of nodes correspond to the longitudes of the ascending equator crossing. Since the orbital plane is not fixed in the ECEF frame, the longitude of the node is time-dependent due to the rotation of the Earth. The time rate of the node of each satellite in the inertial frame, $\dot{\Omega}$ and $\dot{\Omega}'$, are neglected and we assume a 2-body motion. For each satellite, the longitude of the node at the instant t is therefore defined as follows

$$\left\{ \begin{array}{l} \lambda_{\Omega}(t) = \Omega - \theta_G(t) = \Omega - \theta_G(t_0) - \omega_E(t - t_0) = \lambda_{\Omega}(t_0) - \omega_E dt \quad (5.6) \\ \lambda_{\Omega'}(t') = \Omega' - \theta_G(t') = \Omega' - \theta_G(t'_0) - \omega_E(t' - t'_0) = \lambda_{\Omega'}(t'_0) - \omega_E dt' \quad (5.7) \end{array} \right.$$

$$\text{and } \left\{ \begin{array}{l} \Delta \lambda_{\Omega 0} = \lambda_{\Omega'}(t'_0) - \lambda_{\Omega}(t_0) = \Omega' - \Omega - (\theta_G(t'_0) - \theta_G(t_0)) \quad (5.8) \\ \Delta \lambda_{\Omega} = \lambda_{\Omega'}(t') - \lambda_{\Omega}(t) = \Delta \lambda_{\Omega 0} - \omega_E(dt' - dt) \quad (5.9) \end{array} \right.$$

where θ_G is the angle between the vernal equinox and the direction given by the unit vector $\hat{\varepsilon}_1$, ω_E is the rotation rate of the Earth and t_0 is a reference epoch. The epoch t_0 is chosen to represent the time at which the satellite crosses the equatorial plane in the

ascending direction, that is to say the time corresponding to the ascending node. It is important to note that the values of t_0 , t and dt are different a priori from t'_0 , t' and dt' .

Substituting Eq. (5.8) into Eq. (5.4) and Eq. (5.5), the condition $\hat{\varepsilon}_r = \hat{\varepsilon}'_r$ can be written as a system of three independent equations:

$$\left\{ \begin{array}{l} \cos(\nu + \omega) = \cos \Delta\lambda_\Omega \cos(\nu' + \omega') - \sin \Delta\lambda_\Omega \sin(\nu' + \omega') \cos i' \end{array} \right. \quad (5.10)$$

$$\left\{ \begin{array}{l} \sin(\nu + \omega) \cos i = \sin \Delta\lambda_\Omega \cos(\nu' + \omega') + \cos \Delta\lambda_\Omega \sin(\nu' + \omega') \cos i' \end{array} \right. \quad (5.11)$$

$$\left\{ \begin{array}{l} \sin(\nu + \omega) \sin i = \sin(\nu' + \omega') \sin i' \end{array} \right. \quad (5.12)$$

Recombining these three equations together we obtain the following necessary condition for the crossover:

$$\cot(\nu + \omega) = \cot \Delta\lambda_\Omega (\cos i - \cot i' \sin i \cos \Delta\lambda_\Omega) - \cot i' \sin i \sin \Delta\lambda_\Omega \quad (5.13)$$

Eq. (5.13) gives the argument of latitude for one satellite passing above the crossover location as a function of its orbit inclination and the difference in longitude between the nodes of the two orbit planes. Knowing the longitude of the line of node for each orbit and therefore the value for $\Delta\lambda_\Omega$, it seems straight forward to obtain the location of the crossover given by $\nu + \omega$. However, Eq. (5.13) is not a practical equation to use in order to determine the location of the crossover. Looking at the groundtrack of the satellites, the difference in longitude between the ascending node of each satellite $\Delta\lambda_{\Omega_0}$ does not represent the longitude difference between the lines of nodes at the time when the satellites pass above the location of the crossover as shown in Eq. (5.9). The

parameter $\Delta\lambda_\Omega$ is a function of dt and dt' , which are themselves directly related to the respective true anomalies of the satellites ν and ν' . More precisely, the times t_0 and t_0' in Eq. (5.6) and Eq. (5.7) are chosen to represent the epochs at which the satellites pass over the equator in the ascending direction, and the times t and t' the epochs at which the satellites pass over the location of the crossover. The difference $\Delta\lambda_\Omega$ between the longitudes of the nodes of the two satellites will not be the same when the satellites are above the equator or above the crossover location as shown in Eq. (5.8) and Eq. (5.9). Hence, it appears that Eq. (5.13) is in fact an implicit function, which would require an iterative method to obtain an approximate numerical solution. In the following section, we will show a different approach to the problem that leads to an explicit analytical solution using some of the relations established in this section.

5.1.2 EXPLICIT FUNCTION

In this section, the problem of finding the location of a crossover between two groundtracks is approached differently. In the previous section, we started with the groundtracks of two satellites and we determined where they intersected. We are now taking the opposite approach. Suppose that the latitude at the crossover, φ_{CrOv} , is being determined by mission and science requirements and suppose that the longitude of the equatorial crossing of one of the two satellites, called *SatA*, is also known or pre-determined (in our case, we will work with the ascending crossing). We designate this

longitude as $\lambda_{\Omega, A0}$. To achieve the crossover, the only parameter left to be determined is the longitude of the equatorial crossing of the second satellite, *SatB*.

We first consider the intersection of *SatA*'s orbit and the parallel at latitude φ_{CrOv} . There are in fact two intersections, which can be identified by their arguments of latitude $\omega + \nu$ on *SatA*'s orbit. Using the spherical law of cosines, we get:

$$\sin(\omega_A + \nu) = \frac{\sin(\varphi_{CrOv})}{\sin(i_A)} \quad (5.14)$$

where i_A and ω_A are respectively the inclination and the argument of perigee of *SatA*'s orbit. Eq. (5.14) has two solutions for the true anomaly ν_A . The same results can be applied to *SatB*'s orbit:

$$\left\{ \begin{array}{l} \nu_{A1} = \sin^{-1}\left(\frac{\sin(\varphi_{CrOv})}{\sin(i_A)}\right) - \omega_A \end{array} \right. \quad (5.15)$$

$$\left\{ \begin{array}{l} \nu_{A2} = \pi - \sin^{-1}\left(\frac{\sin(\varphi_{CrOv})}{\sin(i_A)}\right) - \omega_A \end{array} \right. \quad (5.16)$$

$$\left\{ \begin{array}{l} \nu_{B1} = \sin^{-1}\left(\frac{\sin(\varphi_{CrOv})}{\sin(i_B)}\right) - \omega_B \end{array} \right. \quad (5.17)$$

$$\left\{ \begin{array}{l} \nu_{B2} = \pi - \sin^{-1}\left(\frac{\sin(\varphi_{CrOv})}{\sin(i_B)}\right) - \omega_B \end{array} \right. \quad (5.18)$$

Though the approach is different from the previous section, the Keplerian geometry of the orbits remains the same. Therefore, to determine the longitude of the equatorial

crossing of *SatB*, it will ultimately be necessary to express the time differences $t - t_0$ and $t' - t_0'$ and $t' - t_0'$ from Eq. (5.6) and Eq. (5.7) in terms of the orbital elements of each satellite. In this respect, we transform into eccentric anomalies the four true anomalies of Eq. (5.15) to Eq. (5.18), as well as the true anomalies of both satellites at their equatorial crossings, ν_{A0} and ν_{B0} . This is done using the following relationships between true and eccentric anomalies:

$$\left\{ \begin{array}{l} \cos(E_{Xn}) = \frac{e_X + \cos(\nu_{Xn})}{1 + e_X \cos(\nu_{Xn})} \end{array} \right. \quad (5.19)$$

$$\left\{ \begin{array}{l} \sin(E_{Xn}) = \frac{\sqrt{1 - e_X^2} \sin(\nu_{Xn})}{1 + e_X \cos(\nu_{Xn})} \end{array} \right. \quad (5.20)$$

where X represents either A or B for *SatA* or *SatB*, and n is $0, 1$ or 2 for the anomalies at the equator or the anomalies solutions of Eq. (5.15) to Eq. (5.18). Finally, e_X is the eccentricity of either *SatA* or *SatB*. Once the eccentric anomalies are known, it is possible to express the time required for each satellite to travel from its position over the equatorial crossing to any of the two positions determined in Eq. (5.15) to Eq. (5.18). This time difference is computed using the mean anomalies, M , and the Kepler's equation:

$$dt_{Xn} = t_{Xn} - t_{X0} = \frac{M_{Xn} - M_{X0}}{n_{SatX}} \quad (5.21)$$

$$M_{Xn} = E_{Xn} - e_X \sin(E_{Xn}) \quad (5.22)$$

where n_{SatX} is the mean motion of the *SatA* or *SatB*. Now that the values of the time differences are known, it is possible to determine the longitude of *SatI*'s line of node at the times it passes over each crossover location, $\lambda_{\Omega,A1}$ and $\lambda_{\Omega,A2}$ using Eq. (5.6). Recombining Eq. (5.3) and Eq. (5.4), it is then finally possible to compute the longitudes of the two crossover locations, $\lambda_{CrOv,1}$ and $\lambda_{CrOv,2}$:

$$\lambda_{\Omega,An} = \lambda_{\Omega,A0} - \omega_E dt_{An} \quad (5.23)$$

$$\left\{ \begin{array}{l} \cos(\lambda_{CrOv,n}) = \frac{\cos(\omega_A + \nu_{An}) \cos(\lambda_{\Omega,An}) - \cos(i_A) \sin(\omega_A + \nu_{An}) \sin(\lambda_{\Omega,An})}{\cos(\varphi_{CrOv,n})} \end{array} \right. \quad (5.24)$$

$$\left\{ \begin{array}{l} \sin(\lambda_{CrOv,n}) = \frac{\cos(\omega_A + \nu_{An}) \sin(\lambda_{\Omega,An}) + \cos(i_A) \sin(\omega_A + \nu_{An}) \cos(\lambda_{\Omega,An})}{\cos(\varphi_{CrOv,n})} \end{array} \right. \quad (5.25)$$

The last parameter to determine is the longitude of *SatB*'s equatorial crossing, $\lambda_{\Omega,B0}$. Since there are two true anomalies for each satellite that correspond to the latitude λ_{CrOv} , there will be four configurations possible for a track crossover at that latitude: one possible intersection between two ascending tracks; one possible intersection; finally, two intersections are possible between an ascending track and a descending track. Therefore, we introduce a new subscript, $m = 1..2$, to differentiate the two true anomalies defined in Eq. (5.17) and Eq. (5.18). The step described in Eq. (5.26) to Eq. (5.28) is the exact reverse as the one described from Eq. (5.23) to Eq. (5.25) as it gives the value of $\lambda_{\Omega,B0}$ knowing the value of λ_{CrOv} :

$$\left\{ \begin{aligned} \cos(\lambda_{\Omega, Bnm}) &= \frac{\cos(\omega_B + \nu_{Bm}) \cos(\lambda_{CrOv,n}) + \cos(i_B) \sin(\omega_B + \nu_{Bm}) \sin(\lambda_{CrOv,n})}{\cos^2(\omega_B + \nu_{Bm}) + \cos^2(i_B) \sin^2(\omega_B + \nu_{Bm})} \cos(\varphi_{CrOv,n}) \end{aligned} \right. \quad (5.26)$$

$$\left\{ \begin{aligned} \sin(\lambda_{\Omega, Bnm}) &= \frac{\cos(\omega_B + \nu_{Bm}) \sin(\lambda_{CrOv,n}) - \cos(i_B) \sin(\omega_B + \nu_{Bm}) \cos(\lambda_{CrOv,n})}{\cos^2(\omega_B + \nu_{Bm}) + \cos^2(i_B) \sin^2(\omega_B + \nu_{Bm})} \cos(\varphi_{CrOv,n}) \end{aligned} \right. \quad (5.27)$$

$$\lambda_{\Omega, B0nm} = \lambda_{\Omega, Bnm} + \omega_E dt_{Bn} \quad (5.28)$$

Starting from a desired latitude where the crossover is required to occur and the longitude of the equatorial crossing of one of the two satellites, we were able to get an analytical solution for the longitude of the crossover as well as the longitude of the equatorial crossing of the second satellite's track. The other orbital characteristics of the two satellites being given, we have determined the positions of the two orbital planes that will lead to a crossover at the latitude imposed by the mission requirements. In the case where the location of the crossover would be site-specific, therefore fixing not only the value of $\varphi_{CrOv,n}$, but also the value of $\lambda_{CrOv,n}$, the step described in Eq. (5.23) to Eq. (5.25) would be replaced by a step similar to the one described in Eq. (5.26) to Eq. (5.28) but applied to *SatA*.

However, in this section it is still not possible to give an analytical solution to the problem as it was set in the previous section. Given solely the longitude of the ascending of each satellite track, it is not possible to find an analytical solution for φ_{CrOv} and λ_{CrOv} in the general case of two non-circular orbits.

5.2 ANGLE BETWEEN TRACKS

In this section we want to determine the angle between the groundtracks at the location of the crossover, ω_{CrOv} . If we can express the unit vectors tangential to each track, then a simple dot product will give us the angle between the two vectors, therefore between the tracks. Each of the tangential vectors $\hat{\epsilon}_{TX}$, with $X = A$ or B for *SatA* or *SatB*, can be expressed in terms of the satellite's orbital elements in the Earth Centered Inertial (ECI) frame as follows:

$$\hat{\epsilon}_{TX} = [\hat{\epsilon}_{I1} \quad \hat{\epsilon}_{I2} \quad \hat{\epsilon}_{I3}] \cdot \begin{bmatrix} -\sin(\omega_X + \nu_X) \cos(\Omega_X) - \cos(\omega_X + \nu_X) \sin(\Omega_X) \cos i_X \\ -\sin(\omega_X + \nu_X) \sin(\Omega_X) + \cos(\omega_X + \nu_X) \cos(\Omega_X) \cos i_X \\ \cos(\omega_X + \nu_X) \sin i_X \end{bmatrix} \quad (5.29)$$

where $(\hat{\epsilon}_{I1}, \hat{\epsilon}_{I2}, \hat{\epsilon}_{I3})$ are the unit vectors of the ECI frame. After much trigonometric simplifications and making use of Eq. (5.9), we find the following expression for the crossover track angle:

$$\begin{aligned} \cos(\omega_{CrOv}) = & \cos(\lambda_{\Omega_{B0}} - \lambda_{\Omega_{A0}}) (\sin(\omega_A + \nu_A) \sin(\omega_B + \nu_B) + \cos(\omega_A + \nu_A) \cos(\omega_B + \nu_B) \cos i_A \cos i_B) \\ & + \sin(\lambda_{\Omega_{B0}} - \lambda_{\Omega_{A0}}) (\sin(\omega_A + \nu_A) \cos(\omega_B + \nu_B) \cos i_B + \cos(\omega_A + \nu_A) \cos(\omega_B + \nu_B) \cos i_A) \\ & + \cos(\omega_A + \nu_A) \cos(\omega_B + \nu_B) \sin i_A \sin i_B \end{aligned} \quad (5.30)$$

5.3 APPLICATIONS TO ICESAT AND CRYOSAT

The theory presented in the two previous sections was developed to address the problem of groundtracks crossover for the ICESat and CryoSat satellites. The analytical solutions, both implicit and explicit, remain however general enough so that they can be used to identify the intersections between the groundtracks of any two elliptic Keplerian orbits. As the interest for the intersections between ICESat and CryoSat groundtracks was the first incentive for this study, we will use the results obtained for this case to illustrate the theory detailed previously. In the following sections, we will look at other cases including the ENVISAT orbit and the ICESat calibration orbit.

The results presented below were obtained to test the feasibility of an off-nadir maneuver in which the ICESat GLAS altimeter would be pointed at the CryoSat track. It is required that the off-nadir rotation should not exceed 5 degrees. This limit represents one of the criteria for the feasibility of the maneuver, along with the attitude acceleration rate of the satellite. For this reason, we were interested in determining the relative position between the tracks of the two satellites that would lead to a minimum value for the angle between the tracks. The characteristics of ICESat's orbit as well as its groundtrack are well known. On the other hand, some of the characteristics of the CryoSat orbit, such as the exact mean value of its semi-major axis had to be inferred from the CryoSat mission overview documents (ESA, 2003).

Orbit Characteristics	ICESat orbit	CryoSat orbit
Repeat Cycle	91 nodal days	369 nodal days
Number of Sat. Rev. per Cycle	1354	5344
Semi-Major Axis	6970.238 km	7095.348 km
Eccentricity	0.0013	0.0014
Inclination	94°	92°
Argument of Perigee	90°	90°
Longitude of Node for the chosen track: $\lambda_{\Omega 0}$	29.043°W	(To Be Determined)

Table 5.1: Characteristics of ICESat and CryoSat orbits.
Sources from Mission Overview documents: (Schutz et al., 2005) (ESA, 2003) and (Wingham et al., 2006)

Finally, since the case to be studied is a hypothetical one, there is no actual requirement for the location of the crossover, but the location was chosen to represent a typical choice in the polar region. Hence a latitude in the vicinity of 70°N. One of ICESat's 1354 tracks was selected arbitrarily with an ascending segment of the track that cuts through the Greenland region. The characteristics of the two orbit are summarized in Table (5.1).

The results of Eq. (5.30) are shown on Fig. (5.1) for values of $(\lambda_{\Omega, C0} - \lambda_{\Omega, I0})$ ranging from -180° to 180° and values of the latitude at the crossover (φ_{Crov}) ranging from 0° to 86°. The latitude equal 86° corresponds to the highest latitude reached by

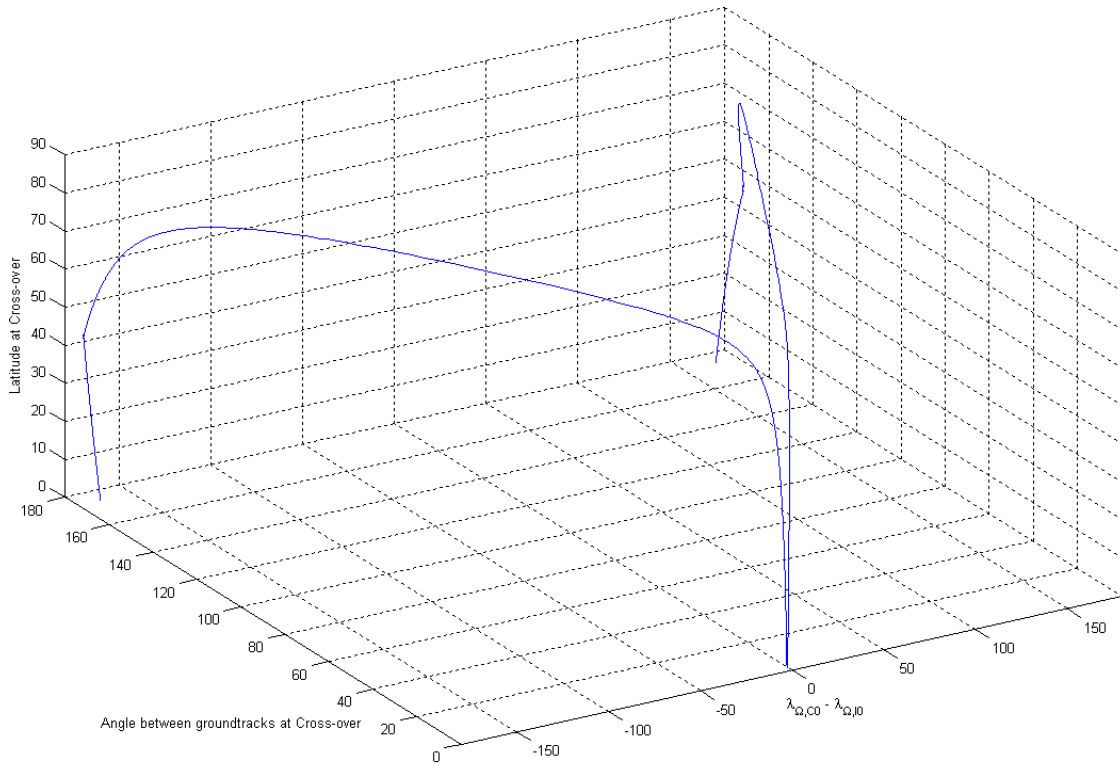


Fig. 5.1: 3-dimensional plot giving the latitude at the crossover (φ_{CrOv}) as a function of the difference of the equatorial crossings longitudes ($\lambda_{\Omega,C0} - \lambda_{\Omega,I0}$) and the angle between the tracks at the crossover (ω_{CrOv}).

ICESat. The plot is approximately symmetrical with respect to the vertical plane defined by $(\lambda_{\Omega,C0} - \lambda_{\Omega,I0}) = 0$. The small asymmetry is due to the rotation of the Earth during each satellite's half revolution over the northern hemisphere, and the fact that the two orbits do not have the same nodal period. The discontinuity in the derivative of the function in the region of $(\lambda_{\Omega,C0} - \lambda_{\Omega,I0}) = \pm 180^\circ$ is explained by the 360° -periodicity of the term $(\lambda_{\Omega,C0} - \lambda_{\Omega,I0})$. The lower segment of the curve at $(\lambda_{\Omega,C0} - \lambda_{\Omega,I0}) = 180^\circ$ is the continuation of the function beyond $(\lambda_{\Omega,C0} - \lambda_{\Omega,I0}) = -180^\circ$ but translated back into

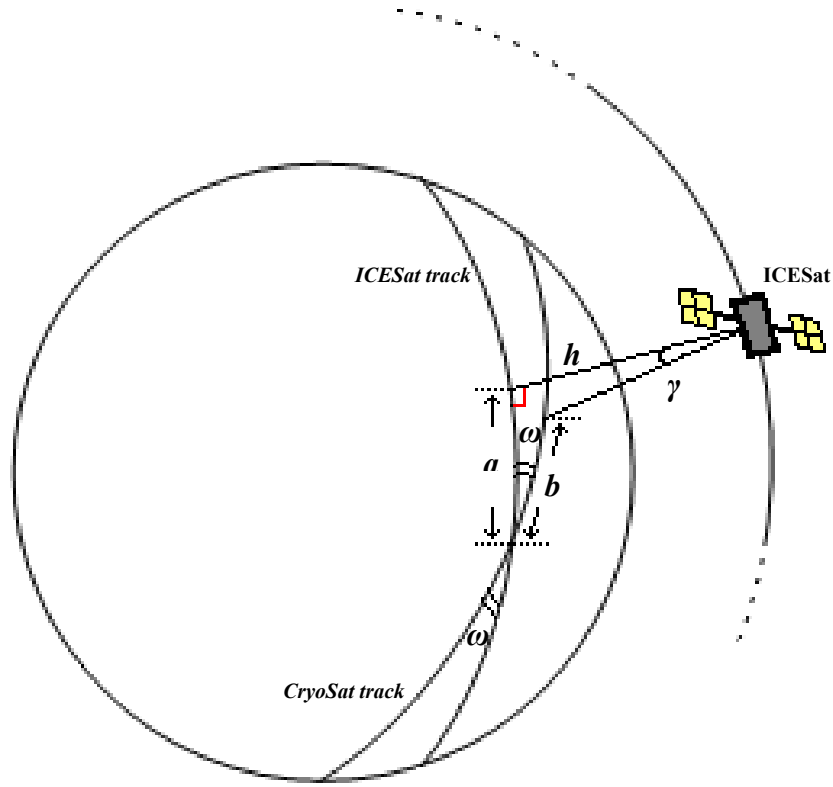


Fig. 5.2: Off-nadir pointing.

the interval $(-180^\circ, 180^\circ)$ via a modulo 360° , and vice versa. It is desired to implement the off-nadir maneuver above the latitude 70°N and the maximum off-nadir angle, γ , permitted for the rotation of ICESat is 5° . As illustrated on Fig. (5.2), the angle γ is directly related to the angle between the groundtracks (simply referred on the picture as ω instead of ω_{CrOv}) and the length of the CryoSat track segment that is being followed by ICESat. If it is assumed that the segments are sufficiently small with respect to the Earth radius, then the triangle described by the segments of lengths a and b in Fig. (5.2) is in a plane.

Under the previous assumption, γ and ω_{CrOv} satisfy the following relationship:

$$\omega_{CrOv} = \cos^{-1}\left(\frac{a^2 + b^2 - (h \cdot \tan \gamma)^2}{2ab}\right) \quad (5.31)$$

To test the feasibility of the off-nadir pointing maneuver, the interval of time dt was arbitrarily chosen to be equal to 50 seconds. More precisely, ICESat follows the CryoSat groundtrack 25 seconds before and 25 seconds after flying over the crossover location. The value of γ varies throughout the maneuver reaching a minimum of 0° at the crossover. The maximum value is found the furthest away from the crossover, that is when a and b are equal to:

$$a = \frac{R_{Earth}}{2} n_{ICESat} dt \quad (5.32)$$

$$b = \frac{R_{Earth}}{2} n_{CryoSat} dt \quad (5.33)$$

with the eccentricities being neglected and where n_{ICESat} and $n_{CryoSat}$ are the mean motion of the two satellites. Eq. (5.31) through Eq. (5.33) are applied to the case of ICESat to find the maximum acceptable value for the angle between the tracks, ω_{CrOv} . To ensure that γ remains less than 5° , ω_{CrOv} , must be less than 17.6° .

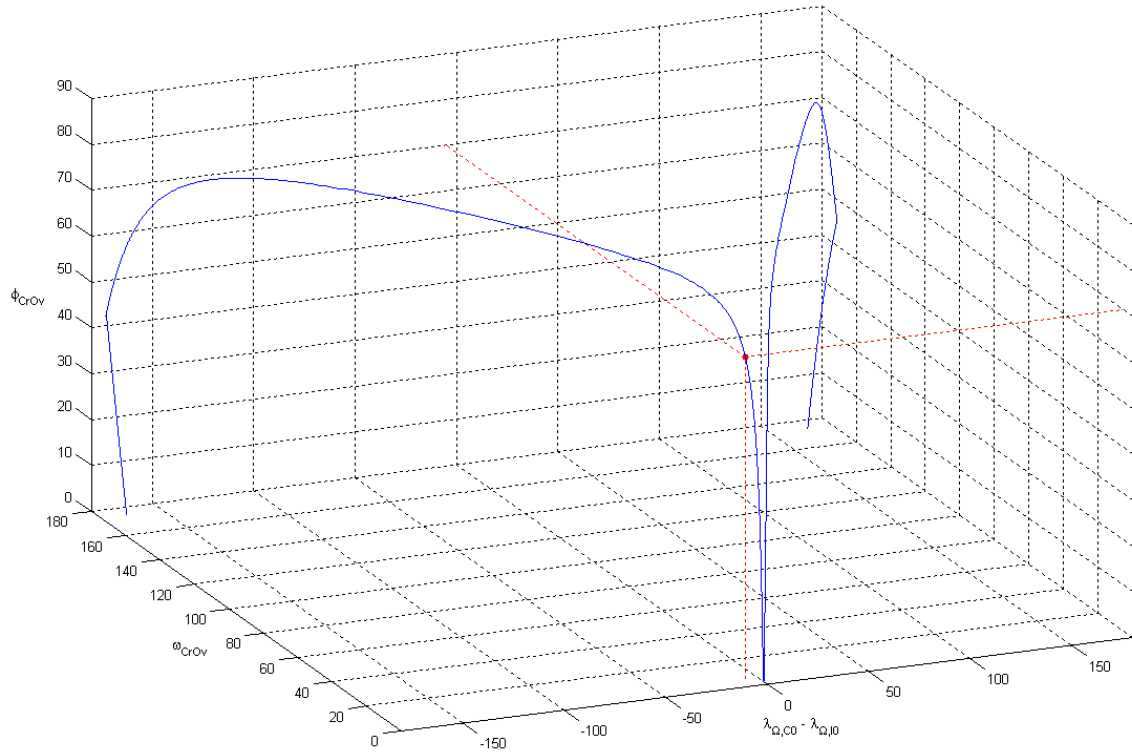


Fig. 5.3: ICESat vs. CryoSat case. 3-dimensional plot giving the latitude at the crossover (ϕ_{CrOv}) as a function of the difference of the equatorial crossings longitudes ($\lambda_{\Omega,C0} - \lambda_{\Omega,I0}$) and the angle between the tracks at the crossover (ω_{CrOv}). A solution is selected for an altitude of 70°N and an angle between tracks less than 17.6°.

Using the three-dimensional plot on Fig. (5.3) and its two-dimensional projections on Fig. (5.4), it is possible to identify a solution for the value of the longitude difference between the equatorial crossings of the ICESat and CryoSat tracks at a latitude of 70°N while respecting the condition $\omega_{CrOv} < 17.6^\circ$. The condition on ω_{CrOv} is indeed respected since the angle between tracks at this altitude is equal to 5.855°. The rest of the results are summarized in Table (5.2). The resulting crossover is illustrated on Fig. (5.5) and a close-up of the Greenland region is given in Fig. (5.6).

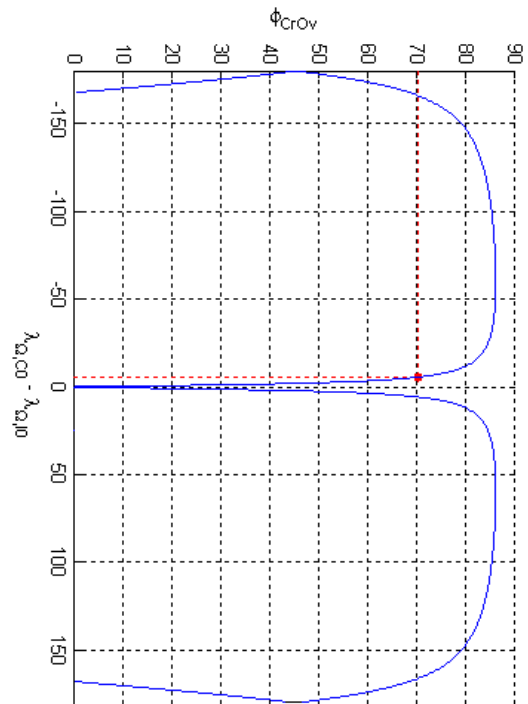
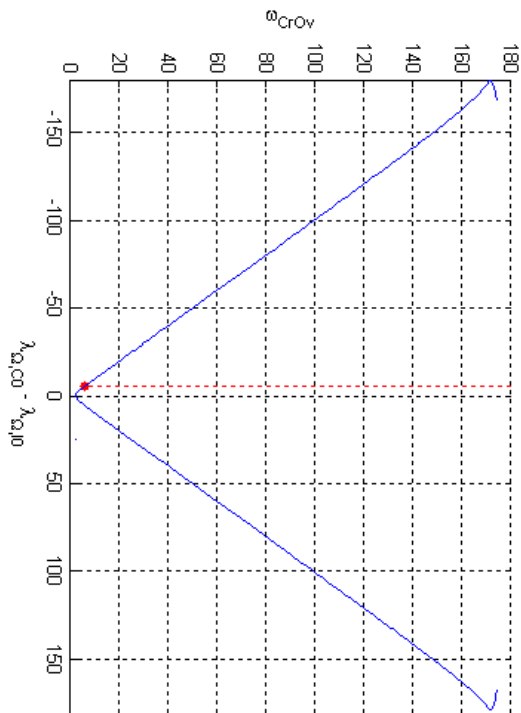
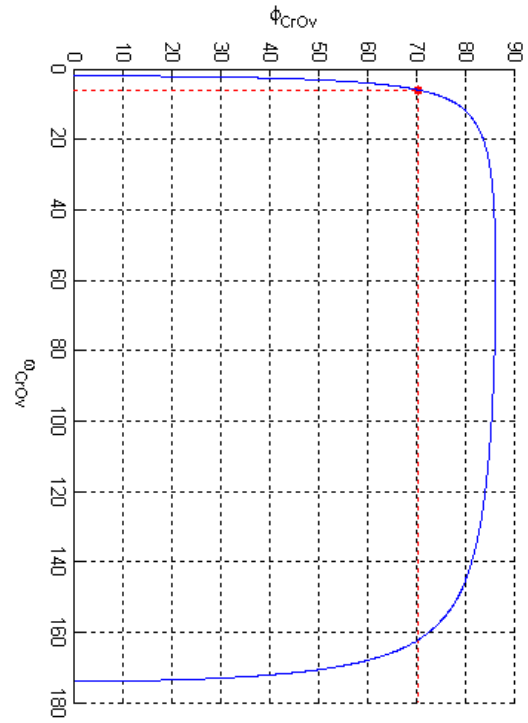
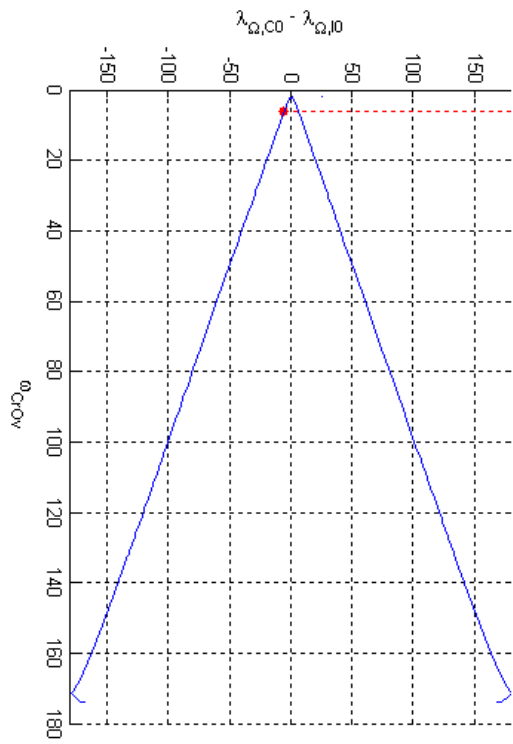


Fig. 5.4: Projections of Fig. (5.3)

Off-nadir maneuver parameters	
Latitude: φ_{CrOv}	69.998°N
Longitude: λ_{CrOv}	44.857°W
ICESat ascending node (ECEF): $\lambda_{\Omega,I0}$	29.043°W
CryoSat ascending node (ECEF): $\lambda_{\Omega,C0}$	34.508°W
$\lambda_{\Omega,C0} - \lambda_{\Omega,I0}$	-5.465°
ICESat track segment: a	339.121 meters
CryoSat track segment: b	335.066 meters
Angle between track: ω_{CrOv}	5.855°
Off-nadir angle: γ	1.657°

Table 5.2: Summary of the parameters for the off-nadir maneuver over Greenland at latitude 70°N.

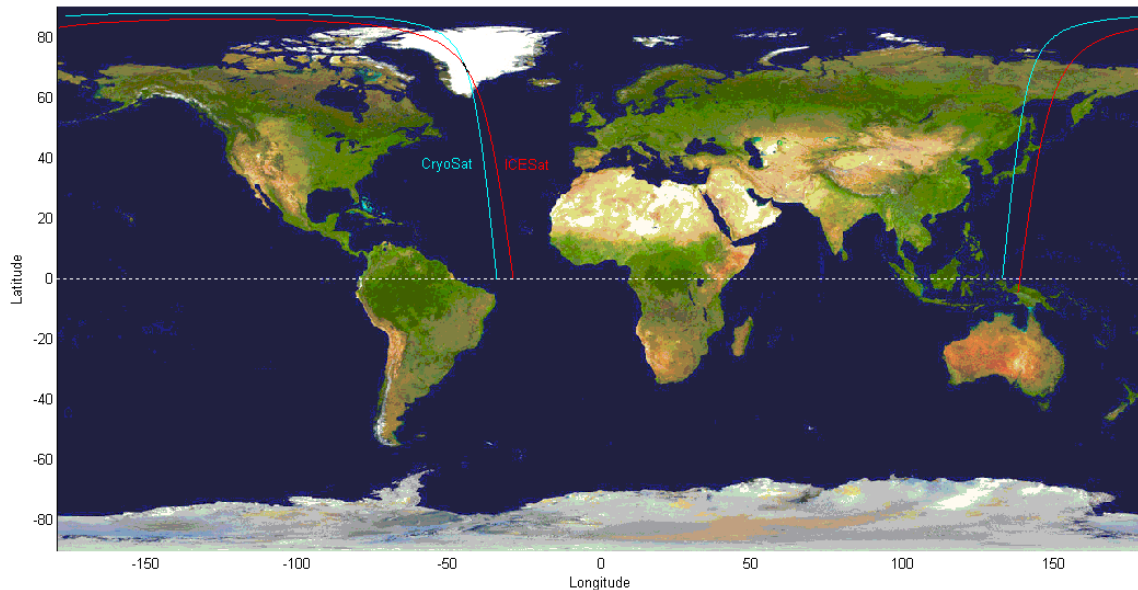


Fig. 5.5: Crossover between ICESat and CryoSat tracks over Greenland at latitude 70°N. (Background picture from <http://visibleearth.nasa.gov>)

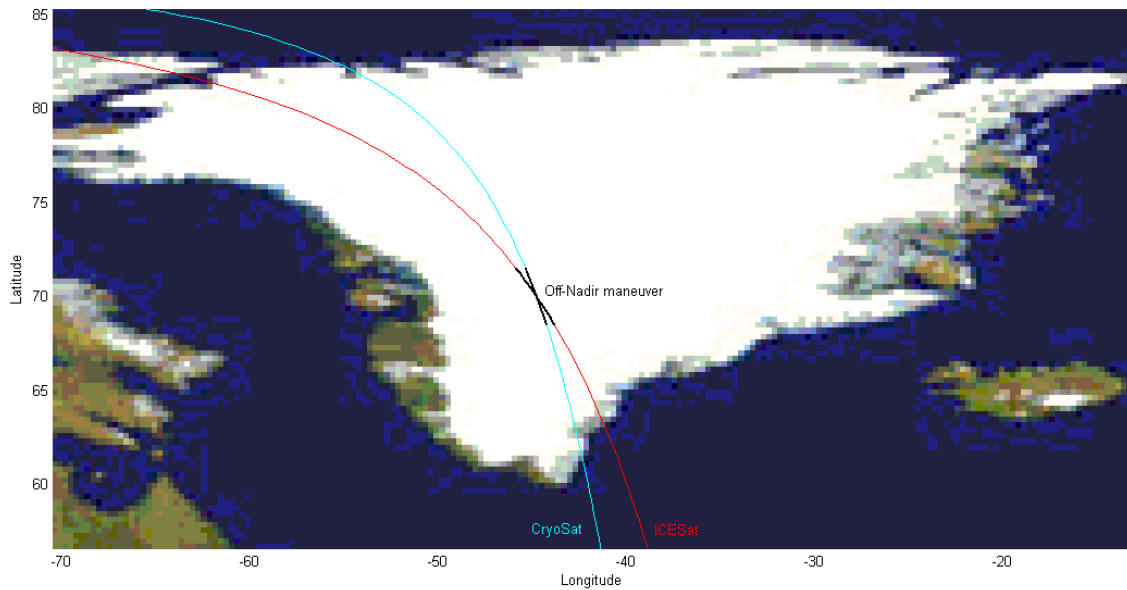


Fig. 5.6: Close-up of ICESat and CryoSat crossover at latitude 70°N. The segments of the groundtrack corresponding to the 50 seconds during which the ICESat laser follows the CryoSat groundtrack appear in black.
 (Background picture from <http://visibleearth.nasa.gov>)

5.4 APPLICATION TO ICESAT AND ENVISAT

ENVISAT was launched in March 2002 as part of the European Space Agency Earth Observation program. The ENVISAT mission is the follow-on of the very successful mission ERS-1 and ERS-2. The main objectives of the mission are to provide extensive continuous data to environmental and climate studies, which includes ocean dynamics, ice sheet characteristics and sea ice distribution among others. It was launched into an orbit similar to the ERS orbits: sun-synchronous with an inclination of 98.55° and a mean altitude of 799.8 km. The orbit is also repeat-groundtrack, with a repeat cycle of 35 nodal days which is consists made of 501 satellite revolutions. Because of its sun-synchronous characteristic, the maximum latitude reached by the satellite is 81.45°,

Orbit Characteristics	ICESat orbit	ENVISAT orbit
Repeat Cycle	91 nodal days	35 nodal days
Number of Sat. Rev per Cycle	1354	501
Semi-Major Axis	6970.238 km	7159.5 km
Eccentricity	0.0013	0.0014
Inclination	94°	98.55°
Argument of perigee	90°	90°

Table 5.3: Characteristics of ICESat and ENVISAT orbits.

much lower than ICESat. This greater difference between the inclinations of the two satellites leads to results slightly different from the ones presented on Fig. (5.3) and Fig. (5.4) for the CryoSat satellite. The overall character of the plots however remains similar to the CryoSat's plots.

We apply the same method used in the previous discussion to the search for an intersection over Greenland between ICESat and ENVISAT groundtracks. Though the problem seems identical, the approach used to solve the case of ENVISAT is slightly different from the one used previously to solve the case of CryoSat. The difference results from the fact that the CryoSat mission failed at launch. Consequently, the data defining the ECEF longitudes of the ascending nodes of the CryoSat orbit are not available. In the case of ENVISAT, however, the 501 ECEF longitude values corresponding to each ascending node of the 35-day repeat orbit are known. While it was possible in the previous section to adjust the angle between the tracks ω_{Cryo} to any value

that would satisfy the latitude and off-nadir angle constraints, in the case of ENVISAT the value of ω_{CrOv} depends on the tracks selected for ICESat and ENVISAT. Instead of choosing beforehand the value of ICESat's ascending node longitude $\lambda_{\Omega,10}$ as done previously in the CryoSat case, we select a triplet $\{ \lambda_{\Omega,E0} - \lambda_{\Omega,10}, \omega_{CrOv}, \varphi_{CrOv} \}$ that satisfies the required constraints. The selection is done using Fig. (5.7), and for a more exact solution the triplets output file used to plot Fig. (5.7). The plot presented on Fig. (5.7) is similar to the one presented in Fig. (5.3). It shows the correspondence between latitude of the crossover, the angle between tracks and the ascending node longitude difference for ICESat's 91-day repeat orbit and ENVISAT's 35-day repeat orbit. To assist with the interpretation of the plot, the graph is projected onto the three main orthogonal planes of the 3-dimensional view in Fig. (5.8).

Once again, the latitude chosen for the location of the crossover is 70° N. The off-nadir angle constraint is inherent to the ICESat instrumentation limitation and, as such, remains unchanged: the maximum acceptable value for γ is 5° . Using Eq. (5.31) through Eq. (5.33) and replacing $n_{CryoSat}$ by $n_{ENVISAT}$ in Eq. (5.33), we find that the off-nadir angle constraint translates into a maximum value of approximately 17.6° for ω_{CrOv} . The maximum value for ω_{CrOv} is about the same as the one found previously in the case of CryoSat. This similarity is explained by the fact that CryoSat and ENVISAT's mean semi-major axis are only 64 km apart. Therefore $n_{CryoSat}$ and $n_{ENVISAT}$ also have comparable values.

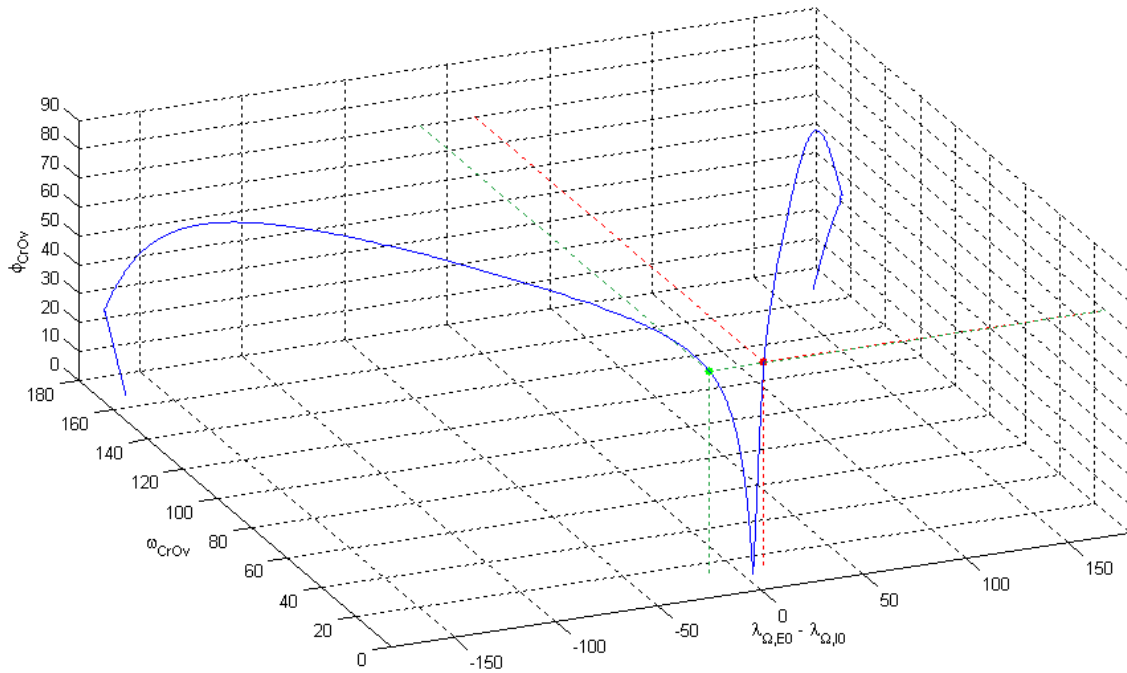


Fig. 5.7: ICESat vs ENVISAT case. 3-dimensional plot giving the latitude at the crossover (φ_{CrOv}) as a function of the difference of the equatorial crossings longitudes ($\lambda_{\Omega,C0} - \lambda_{\Omega,I0}$) and the angle between the tracks at the crossover (ω_{CrOv}). Selecting a solution for an altitude of 70°N and an angle between tracks less than 17.6° .

On Fig. (5.7), two horizontal lines at latitude 70°N intersect the plot at $\omega_{CrOv} = 13.997^\circ$. One of the intersection points corresponds to a solution with $\Delta\lambda_{\Omega,0,1} = \lambda_{\Omega,E0} - \lambda_{\Omega,I0} = 13.616^\circ$ (in red). The second intersection corresponds to a solution with $\Delta\lambda_{\Omega,0,2} = \lambda_{\Omega,E0} - \lambda_{\Omega,I0} = -13.122^\circ$ (in green).

The projections shown on Fig.(5.8) illustrate the comment made in the first paragraph of this section regarding the difference in the inclinations of the two satellites. In the case of ICESat versus CryoSat, the difference in inclination was only 2 degrees. As

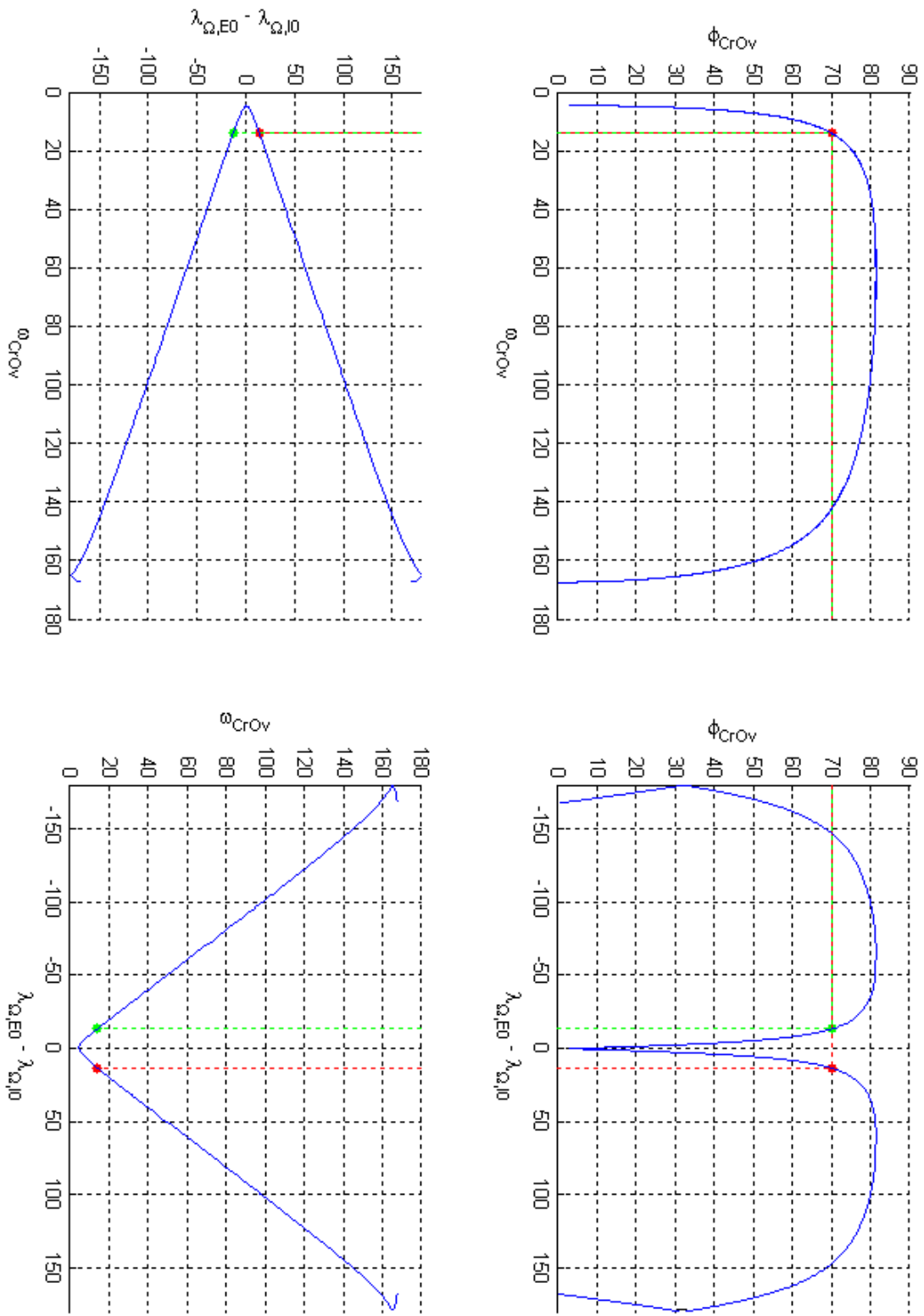


Fig. 5.8: Projections of Fig. (5.7)

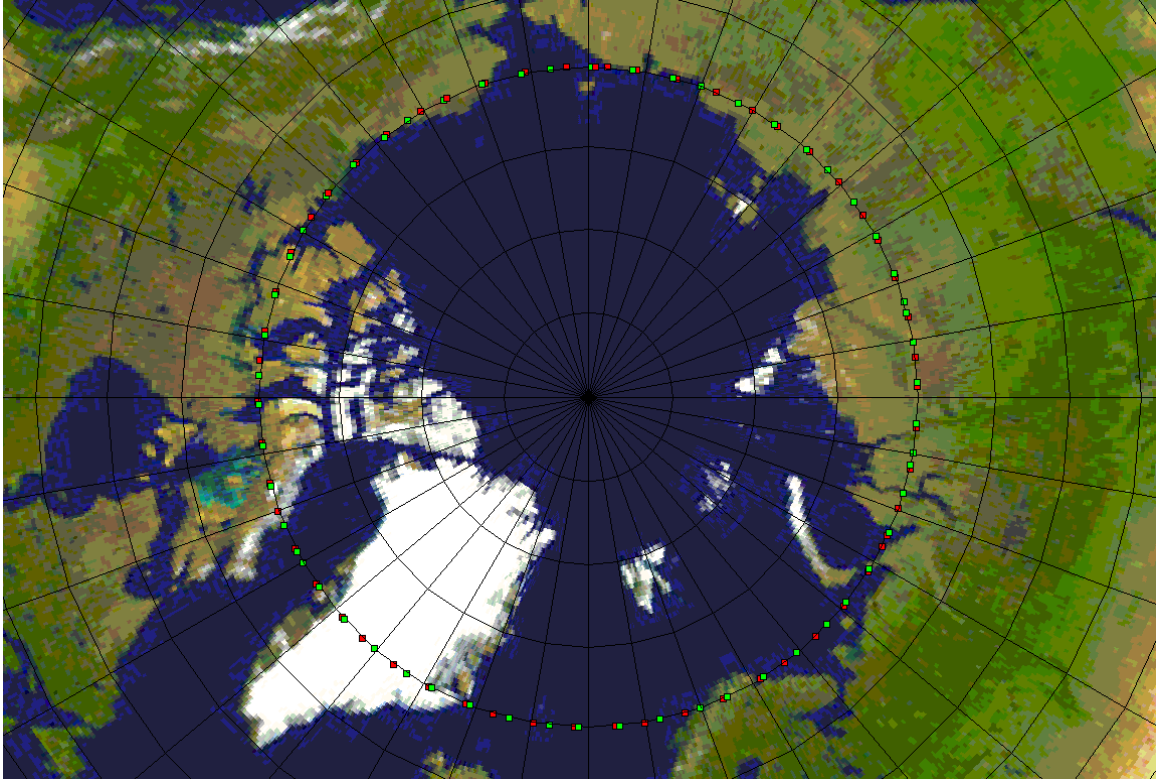


Fig. 5.9: Locations of crossovers between ICESat and ENVISAT tracks at latitude 70°N.
(Background picture from <http://visibleearth.nasa.gov>)

a result, small values for ω_{CrOv} were found at relatively high latitude. In the case of ICESat versus ENVISAT, the difference in inclination is equal to 4.55 degrees and the limit value for ω_{CrOv} due to the off-nadir angle limitation is reached for a much lower latitude than in the previous case, which is clearly apparent when we compare the projection $(\omega_{CrOv}, \varphi_{CrOv})$ of Fig. (5.4) and Fig. (5.8).

Once the two values of the parameter $\Delta\lambda_{\Omega_0}$ are known for a crossover at latitude 70°N, we scan through the ascending node files of both ICESat and ENVISAT and identify the pairs with longitude differences that approach either $\Delta\lambda_{\Omega_{01}}$ or $\Delta\lambda_{\Omega_{02}}$.

λ_{CrOv}	$\varphi_{CrOv} \approx 70^\circ$	$\lambda_{\Omega,IO}$	$\lambda_{\Omega,E0}$	$\Delta\lambda_{\Omega 0}$	ω_{CrOv}	$\gamma < 5^\circ$
-21.0804	70.0142	155.2110	142.0839	-13.1272	13.9479	3.9799
-21.7286	70.0025	-5.9124	7.7126	13.6250	13.9400	3.9777
-28.2510	70.0243	148.0330	134.8982	-13.1347	13.9555	3.9820
-28.8999	69.9928	-13.0899	0.5270	13.6168	13.9323	3.9756
-33.3225	69.9953	142.9809	129.8683	-13.1126	13.9344	3.9761
-36.0723	69.9846	-20.2681	-6.6587	13.6094	13.9253	3.9736
-40.4972	70.0026	135.8018	122.6827	-13.1192	13.9410	3.9780
-43.2480	69.9778	-27.4477	-13.8443	13.6034	13.9196	3.9721
-47.6682	70.0124	128.6243	115.4970	-13.1273	13.9481	3.9799
-48.3176	70.0040	-32.4997	-18.8742	13.6254	13.9396	3.9776
-54.8404	70.0214	121.4453	108.3114	-13.1339	13.9542	3.9816
-55.4881	69.9949	-39.6772	-26.0599	13.6173	13.9328	3.9757

Table 5.4: Detailed information of the crossovers between ICESat and ENVISAT occurring over the Greenland region. The negative values in the first, third and fourth columns indicate longitudes west of the Greenwich meridian.

Starting from the ascending equatorial passing, the orbits of each satellite are propagated for half a revolution. The intersection of the two groundtracks is then found by interpolation of the latitudes over the half-revolution. The interpolation gives the value of the latitude as well as the longitude of the crossover. This last step is performed for each pair of ascending node longitude identified previously. The locations of the crossovers between ICESat and ENVISAT that satisfy the latitude constraint (and therefore the off-nadir constraint) are plotted on Fig. (5.9). The color code is consistent with the one

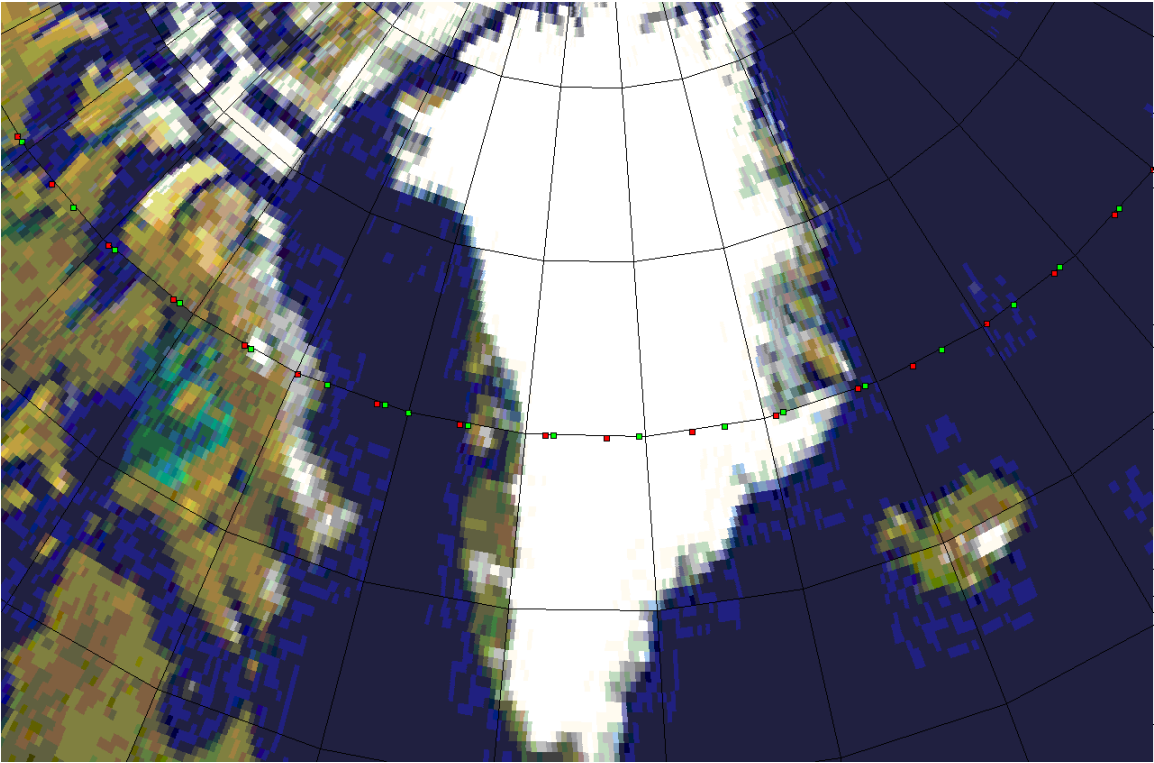


Fig 5.10: Close-up of Fig.(5.9) over the Greenland region for ICESat and ENVISAT crossovers.

used on Fig. (5.7) and Fig. (5.8): the locations in red correspond to ascending nodes' longitude difference close to $\Delta\lambda_{\Omega 01}$ and in green for values close to $\Delta\lambda_{\Omega 02}$. Twelve crossovers were found to occur over the Greenland region while satisfying our constraints. The information for each of these crossovers is summarized in Table (5.4) and then plotted on Fig. (5.10) which is a close-up view of Fig. (5.9) over Greenland. The maximum error in latitude for the crossovers listed in Table (5.4) is 0.02° . A larger tolerance for the constraint on the latitude at crossover would have resulted in a denser distribution of the crossover locations.

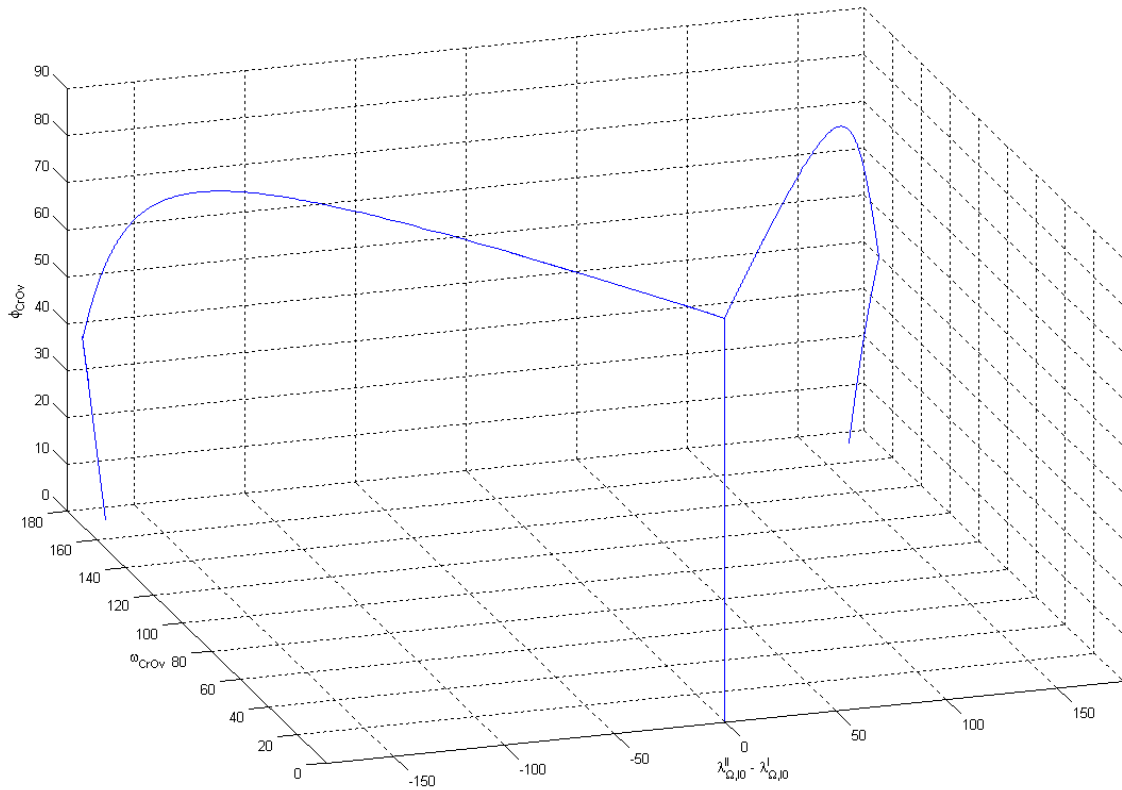


Fig. 5.11: 3-dimensional plot giving the latitude ϕ_{CrOv} as a function of $\lambda''_{\Omega,10} - \lambda^I_{\Omega,10}$ and the angle ω_{CrOv} , where $\lambda''_{\Omega,10}$ is the ECEF longitude of the ascending node belonging to the hypothetical ICESat-II 91-day repeat orbit track (1376 satellite revolutions and altitude of 518 km) and $\lambda^I_{\Omega,10}$ is the one corresponding to the usual ICESat 91-day repeat orbit.

5.5 APPLICATION TO ICESAT AND ICESAT-II

The operational orbit for the future ICESat-II mission is still under discussion. Unless the orbit is chosen to be the exact same orbit as the first ICESat mission, the new repeat groundtrack will not match the one of ICESat. In such a case, the comparison between the altitude measurements along the repeat tracks will be much more difficult to achieve. However, the mission requirements for the future ICESat mission call for a greater agility of the satellite. While 10 minutes are allowed for the ICESat satellite to

perform a 5° off-nadir pointing maneuver, ICESat-II should be required to perform this same maneuver in less than 60 seconds. Therefore in the case of a new operational orbit for the future ICESat mission, we could expect that the off-nadir pointing capabilities of the satellite would be used routinely to enable comparison measurements along segments of the first mission groundtrack. A precise knowledge of the geolocation of the crossovers between the old and the new groundtracks will then be mandatory.

For example, suppose that the operational orbit chosen for the ICESat-II mission is the 91-day repeat orbit presented in Section 3.5.2, with an altitude of 518 km and 1376 satellite revolutions. Fig (5.11) and Fig (5.12) show the 3-dimensional graph that represent the relationship between the latitude at the crossover, the angle between tracks and the longitude difference at the equator between the tracks of ICESat and ICESat-II. The graph shows that crossovers with an admissible angle between tracks can only be found at the highest latitude 85.99° to 86° . This result compromises entirely the idea of performing comparison measurements between the two ICESat missions using the off-nadir pointing maneuver around the crossovers. However, by selecting tracks that lie close to one another, it could be conceivable to perform off-nadir targeting comparable to the ones performed for the TOOs at lower latitudes than the ones corresponding to crossover (Webb et al., 2006). Since it is essential that the data collected by the future ICESat- II mission can be used in correlation with the data collect by ICESat, the feasibility of such maneuvers should be studied before any decision is made regarding ICESat-II's operation orbit.

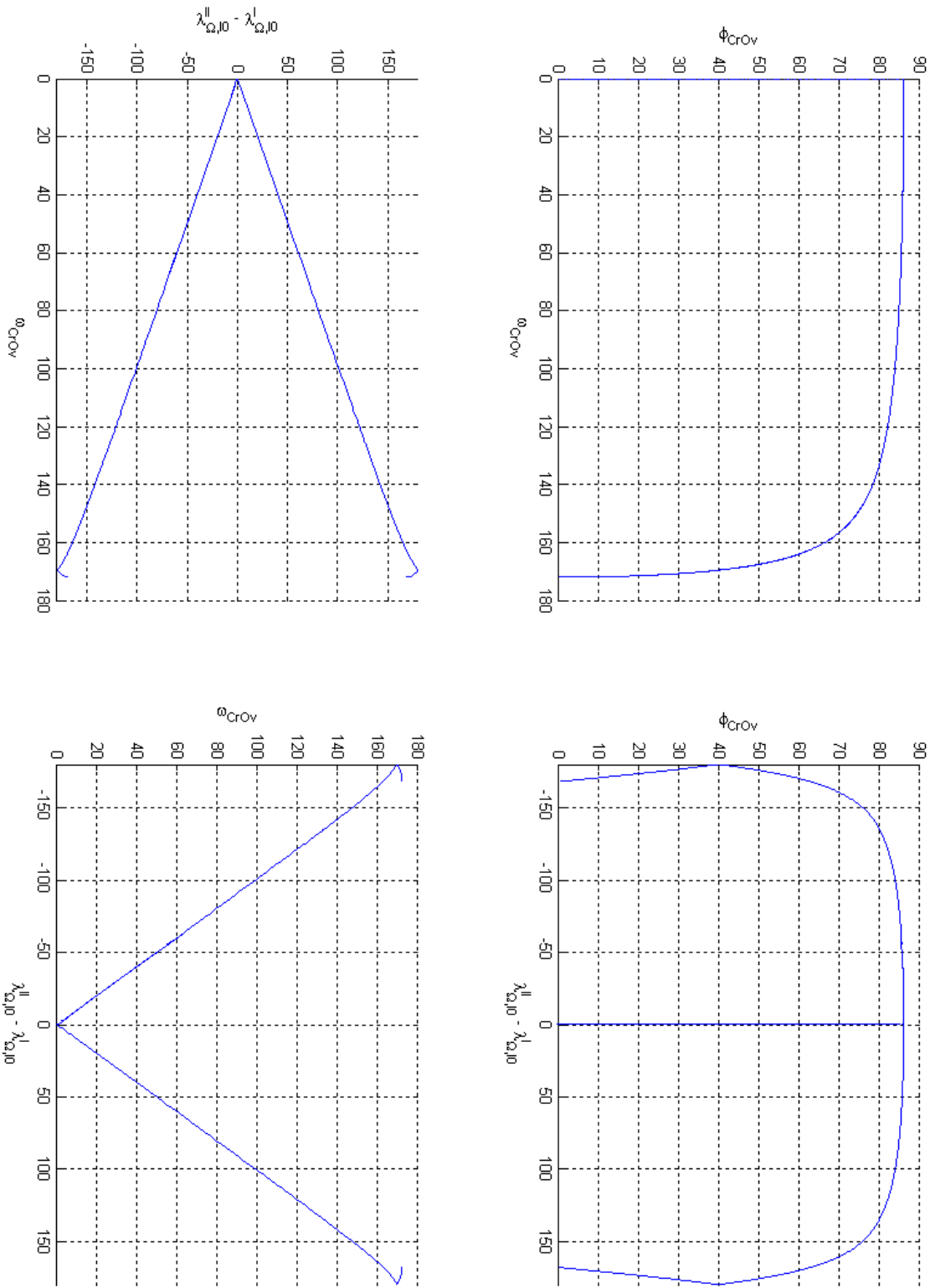


Fig. 5.12: Projections of Fig. (5.11)

CHAPTER 6

THIRD BODY PERTURBATIONS

In this chapter, we study the influence of a perturbing third body on the mean orbital elements of ICESat 91-day repeat groundtrack orbit. Prior literature on the third body perturbation includes the work of Kaula (1962) and Giacaglia (1977). Kaula (1962) expressed the disturbing function in osculating Keplerian elements in a fashion similar to the work he did for the terrestrial gravitational field. Giacaglia (1977) developed the geopotential, the third body and the solar pressure disturbing functions in nonsingular variables. Some recent works include Prado (2003) and Broucke (2003). Both use a double averaging of the third-body potential. Prado (2003) used this potential to analyze the evolution of orbits around major natural moons of the solar system, while Broucke's (2003) motivation was to study the long-term third-body effects on the stability of an Earth satellite. Solórzano and Prado (2004) published a paper in which they study the long term evolution of the orbital elements using a single average model.

In our study, we use a simplified model of the third-body problem. The main body with mass m_{\oplus} is at the origin of the system. The orbit of the perturbing body of mass m' is assumed to be unperturbed Keplerian and elliptical. However, the numerical experiments in this chapter assume that the third body is in a circular orbit. The orbit of the massless spacecraft around the main body is three-dimensional and nominally elliptical. Though the expansion of the disturbing is in part based on the computation developed by Kaula (1962) and Giacaglia (1977), we depart from their work by introducing Chebychev polynomials in the expansion of the potential instead of the usual Hansen's coefficients. By using the Chebychev polynomials we obtain the dependency on the satellite eccentricity as a finite series, whereas the Hansen's coefficients lead to an infinite series and therefore an additional truncation of the disturbing function is necessary during numerical experiments.

6.1 SINGLE-AVERAGE DISTURBING FUNCTION

We recall the most general expression of the disturbing function of a the third-body on a massless spacecraft, which can simply be written as a function of the position vectors of both the spacecraft and the third body with respect from the main body (Morando, 1966):

$$U' = \mu' n'^2 a'^3 \left[\frac{1}{\sqrt{|\vec{r} - \vec{r}'|^2}} - \frac{\vec{r} \cdot \vec{r}'}{r'^3} \right] \quad (6.1)$$

where:

$$\mu' = \frac{m'}{m_{\oplus} + m'}, \quad m_{\oplus} = \text{mass of the main body}, \quad m' = \text{mass of the third body}$$

n' = mean motion of the third body

a' = semi-major axis of the third body's orbit

\vec{r}' = position vector of the third body with respect to the main body

\vec{r} = position vector of the spacecraft with respect to the main body

Under the assumption that $r' \gg r$, this expression can be developed into a series expansion using the Legendre polynomials:

$$U' = \sum_{l=2}^{\infty} U'_l \quad (6.2)$$

with:

$$U'_l = \frac{\mu' n'^2 a'^3}{r'} \left(\frac{r}{r'} \right)^l P_l(\cos \alpha') \quad (6.3)$$

where P_n are the Legendre polynomials and α' is the geocentric elongation of the spacecraft from the third body, or the angle between the position vectors \vec{r} and \vec{r}' . It is possible to relate the elongation angle and the equatorial coordinates by the equation below:

$$\cos \alpha' = \sin \varphi \sin \varphi' + \cos \varphi \cos \varphi' \cos(\lambda - \lambda') \quad (6.4)$$

where:

ϕ = latitude of the spacecraft (with respect to the equator)

λ = longitude of the spacecraft (from the Greenwich meridian in the equator)

ϕ' = latitude of the third body (with respect to the equator)

λ' = longitude of the third body (from the Greenwich meridian in the equator)

The Legendre Polynomials can then be developed further using the equatorial coordinates:

$$P_l(\cos \alpha') = \sum_{m=0}^l \varepsilon_m \frac{(l-m)!}{(l+m)!} P_{lm}(\sin \phi) P_{lm}(\sin \phi') \cos m(\lambda - \lambda') \quad (6.5)$$

where $\varepsilon_m = 2 - \delta_{0m}$ and δ represents the Kronecker function. Giacaglia (1977) introduced some harmonic coefficients to separate the spacecraft's coordinates from the ones of the perturbing body:

$$C'_{lm} = \frac{\mu' n'^2}{a'^{l-2}} \left(\frac{a'}{r'} \right)^{l+1} \varepsilon_m \frac{(l-m)!}{(l+m)!} P_{lm}(\sin \phi') \cos m\lambda' \quad (6.6)$$

$$S'_{lm} = \frac{\mu' n'^2}{a'^{l-2}} \left(\frac{a'}{r'} \right)^{l+1} \varepsilon_m \frac{(l-m)!}{(l+m)!} P_{lm}(\sin \phi') \sin m\lambda' \quad (6.7)$$

Using these harmonic coefficients, the disturbing function is rewritten as:

$$U' = \sum_{l=2}^{\infty} \sum_{m=0}^l U'_{lm} \quad (6.8)$$

with

$$U'_{lm} = r^l P_{lm}(\sin \phi) \{C'_{lm} \cos m\lambda + S'_{lm} \sin m\lambda\} \quad (6.9)$$

Finally, the U'_{lm} terms can be transformed into functions of the spacecraft's orbital coordinates rather than the equatorial ones by introducing the usual inclination functions F_{lmp} (Kaula, 1966) and the angles ψ_{lmp} . This leads to:

$$U'_{lm} = r^l \sum_{p=0}^l F_{lmp}(i) \{A'_{lm} \cos \psi_{lmp} + B'_{lm} \sin \psi_{lmp}\} \quad (6.10)$$

where

$$\psi_{lmp} = (l - 2p)(\omega + f) + m\Omega \quad (6.11)$$

with ω , f , Ω , being respectively the argument of the perigee, the true anomaly and the argument of node. The terms A'_{lm} and B'_{lm} are defined as follows:

$$\begin{aligned} l - m \text{ even:} \quad & A'_{lm} = C'_{lm}, \quad B'_{lm} = S'_{lm} \\ l - m \text{ odd:} \quad & A'_{lm} = -S'_{lm}, \quad B'_{lm} = C'_{lm}. \end{aligned}$$

In order to perform the average of the disturbing function over the short period of the satellite, we separate the true anomaly from the other orbital angles using basic trigonometric identities:

$$\begin{aligned}
U'_{lm} = r^l \sum_{p=0}^l F_{lmp}(i) \left[\{A'_{lm} \cos((l-2p)\omega + m\Omega) \right. \\
+ B'_{lm} \sin((l-2p)\omega + m\Omega)\} \cos(l-2p)f \\
- \{A'_{lm} \sin((l-2p)\omega + m\Omega) \\
\left. - B'_{lm} \cos((l-2p)\omega + m\Omega)\} \sin(l-2p)f \right]
\end{aligned} \tag{6.12}$$

The single-averaged potential $\overline{U'}$ is obtained by integration over the mean anomaly M which is proportional to time. To avoid discussion on the convergence of the integrated Legendre series of Eq. (6.2) and for practical computation purposes, the disturbing function is truncated to n^{th} degree before the integration is performed:

$$\overline{U'}_{2 \rightarrow n} = \frac{1}{2\pi} \int_0^{2\pi} \left(\sum_{l=2}^n \sum_{m=0}^l U'_{lm} \right) dM = \sum_{l=2}^n \sum_{m=0}^l \overline{U'}_{lm} \tag{6.13}$$

where

$$\overline{U'}_{lm} = \frac{1}{2\pi} \int_0^{2\pi} U'_{lm} dM \tag{6.14}$$

Using the relation $r = a(1 - e \cos E)$ and the change of variable $dM = (1 - e \cos E)dE$, where E is the eccentric anomaly, we obtain:

$$\bar{U}'_{lm} = \sum_{p=0}^l a^l F_{lmp}(i) \left[\frac{(A'_{lm} c_{lmp} + B'_{lm} s_{lmp})}{2\pi} \int_0^{2\pi} (1 - e \cos E)^{l+1} \cos(l-2p)f \, dE - \frac{(A'_{lm} s_{lmp} - B'_{lm} c_{lmp})}{2\pi} \int_0^{2\pi} (1 - e \cos E)^{l+1} \sin(l-2p)f \, dE \right] \quad (6.15)$$

where: $c_{lmp} = \cos((l-2p)\omega - m\Omega)$ and $s_{lmp} = \sin((l-2p)\omega - m\Omega)$

We then use the Chebychev polynomials of the first kind to transform $\cos(l-2p)f$ and the Chebychev polynomials of the second kind to transform $\sin(l-2p)f$:

$$\cos(l-2p)f = \sum_{k=0}^{\left\lfloor \frac{|l-2p|}{2} \right\rfloor} T_{lpk}(\cos f)^{|l-2p|-2k} \quad (6.16)$$

$$\sin(l-2p)f = \sum_{k=0}^{\left\lfloor \frac{|l-2p|-1}{2} \right\rfloor} T^*_{lpk}(\cos f)^{|l-2p|-2k-1} \sin f, \quad \text{for } |l-2p| > 0 \quad (6.17)$$

where

$$T_{lpk} = (-1)^k 2^{|l-2p|-2k-1} \frac{|l-2p|}{|l-2p|-k} \frac{(|l-2p|-k)!}{k!(|l-2p|-2k)!} \quad (6.18)$$

$$T^*_{lpk} = (-1)^k 2^{|l-2p|-2k-1} \frac{|l-2p|}{|l-2p|} \frac{(|l-2p|-k-1)!}{k!(|l-2p|-2k-1)!} \quad (6.19)$$

and $\lfloor \cdot \rfloor$ represents the floor function. We call T_{lpk} and T_{lpk}^* the *modified* Chebychev coefficients of the first and second kind respectively. They are based on the usual Chebychev, but applied to the specific case of Eq. (6.16) and (6.17).

Since the true and the eccentric anomalies are directly dependent, we need to replace f by E in Eq. (6.16) and Eq. (6.17). We do so by using the usual relations $\cos f = (\cos E - e)/(1 - e \cos E)$ and $\sin f = (\sqrt{1 - e^2} \sin E)/(1 - e \cos E)$. We can rewrite Eq. (6.15) as follows:

$$\bar{U}_{lm} = \sum_{p=0}^l a^l F_{lmp}(i) \left[\begin{aligned} & \left(A'_{lm} c_{lmp} + B'_{lm} s_{lmp} \right) \sum_{k=0}^{\lfloor \frac{|l-2p|}{2} \rfloor} T_{lpk} I_{lpk}(e) \\ & - \left(A'_{lm} s_{lmp} - B'_{lm} c_{lmp} \right) \sum_{k=0}^{\lfloor \frac{|l-2p|-1}{2} \rfloor} T_{lpk}^* I_{lpk}^*(e) \end{aligned} \right] \quad (6.20)$$

where

$$I_{lpk}(e) = \frac{1}{2\pi} \int_0^{2\pi} (1 - e \cos E)^{2k+l+1-|l-2p|} (\cos E - e)^{|l-2p|-2k} dE \quad (6.21)$$

$$I_{lpk}^*(e) = \frac{1}{2\pi} \int_0^{2\pi} \sqrt{1 - e^2} \sin E (1 - e \cos E)^{2k+l+1-|l-2p|} (\cos E - e)^{|l-2p|-2k-1} dE \quad (6.22)$$

I_{lpk}^* proves to be equal to 0 for any l, p and k such that $|l - 2p| > 0$. If $|l - 2p| = 0$, then the *sin* function under the second integration in Eq. (6.15) is equal to 0, which cancels the second integration. We can therefore simplify Eq. (6.20) and get our final expression of the single-averaged disturbing potential truncated at the Legendre polynomial of degree n :

$$\overline{U'}_{2 \rightarrow n} = \sum_{l=2}^n \sum_{m=0}^l \sum_{p=0}^l \sum_{k=0}^{\lfloor \frac{|l-2p|}{2} \rfloor} \overline{U'}_{lmpk} \quad (6.23)$$

$$\overline{U'}_{lmpk} = a^l F_{lmp}(i) (A'_{lm} c_{lmp} + B'_{lm} s_{lmp}) T_{lpk}(e) I_{lpk}(e) \quad (6.24)$$

The next step is to develop the disturbing function with respect to the third body's orbital coordinates. We start by bringing back the coordinates of the third body λ' and φ' which appear in the terms A'_{lm} and B'_{lm} . We introduce the following coefficients:

$$C'_{lmpk} = \frac{\mu' n'^2 a^l}{a'^{l-2}} \left(\frac{a'}{r'} \right)^{l+1} \varepsilon_m \frac{(l-m)!}{(l+m)!} F_{lmp}(i) T_{lpk}(e) I_{lpk}(e) c_{lmp} \quad (6.25)$$

$$S'_{lmpk} = \frac{\mu' n'^2 a^l}{a'^{l-2}} \left(\frac{a'}{r'} \right)^{l+1} \varepsilon_m \frac{(l-m)!}{(l+m)!} F_{lmp}(i) T_{lpk}(e) I_{lpk}(e) s_{lmp} \quad (6.26)$$

Using the two coefficients above, the term \bar{U}'_{lmpk} can be rewritten in the following fashion:

$$\bar{U}'_{lmpk} = P_{lm}(\sin \varphi') \{ A'_{lmpk} \cos m\lambda' + B'_{lmpk} \sin m\lambda' \} \quad (6.27)$$

where A'_{lm} and B'_{lm} are defined as follows:

$$\begin{aligned} l - m \text{ even:} \quad & A'_{lmpk} = C'_{lmpk}, \quad B'_{lmpk} = S'_{lmpk} \\ l - m \text{ odd:} \quad & A'_{lmpk} = S'_{lmpk}, \quad B'_{lmpk} = -C'_{lmpk}. \end{aligned}$$

Finally, the \bar{U}'_{lmpk} terms can be transformed into functions of the third body's orbital coordinates rather than the equatorial ones by introducing the usual inclination functions $F_{lmp'}$ and the angles $\psi_{lmp'}$. This leads to:

$$\bar{U}'_{lmpk} = \sum_{p'=0}^l F_{lmp'}(i') \{ X_{lmpk} \cos \psi_{lmp'} + Y_{lmpk} \sin \psi_{lmp'} \} \quad (6.28)$$

where

$$\psi_{lmp'} = (l - 2p')(\omega' + f') + m\Omega' \quad (6.29)$$

with i' , ω' , f' and Ω' being respectively the inclination, the argument of the perigee, the true anomaly and the argument of node. The terms X_{lm} and Y_m are defined as follows:

$$\begin{aligned} l - m \text{ even:} \quad & X_{lmpk} = A'_{lmpk} = C'_{lmpk}, \quad Y_{lmpk} = B'_{lmpk} = S'_{lmpk} \\ l - m \text{ odd:} \quad & X_{lmpk} = -B'_{lmpk} = C'_{lmpk}, \quad Y_{lmpk} = A'_{lmpk} = S'_{lmpk}. \end{aligned}$$

Therefore, \bar{U}'_{lmpk} can be simply written as:

$$\bar{U}'_{2 \rightarrow n} = \sum_{l=2}^n \sum_{m=0}^l \sum_{p=0}^l \sum_{k=0}^{\lfloor \frac{|l-2p|}{2} \rfloor} \sum_{p'=0}^l \bar{U}'_{lmpkp'} \quad (6.30)$$

$$\bar{U}'_{lmpkp'} = K_{lm} T_{lpk} F_{lmp'}(i') F_{lmp}(i) I_{lpk}(e) \{ c_{lmp} \cos \psi_{lmp'} + s_{lmp} \sin \psi_{lmp'} \} \quad (6.31)$$

$$\text{with: } K_{lm} = \frac{\mu' n'^2 a^l}{a'^{l-2}} \left(\frac{a'}{r'} \right)^{l+1} \varepsilon_m \frac{(l-m)!}{(l+m)!} \quad (6.32)$$

6.2 EQUATIONS OF MOTION

To study the perturbations of the third body, the single-averaged disturbing function obtained in Eq. (6.23) is used in the Lagrangian Planetary Equations (LPEs), (Kaula, 1966):

$$\frac{da}{dt} = \frac{2}{na} \frac{\partial \bar{U}'}{\partial M} \quad (6.33)$$

$$\frac{de}{dt} = \frac{1-e^2}{na^2 e} \frac{\partial \bar{U}'}{\partial M} - \frac{\sqrt{1-e^2}}{na^2 e} \frac{\partial \bar{U}'}{\partial \omega} \quad (6.34)$$

$$\frac{d\omega}{dt} = -\frac{\cos i}{na^2 \sqrt{1-e^2} \sin i} \frac{\partial \bar{U}'}{\partial i} + \frac{\sqrt{1-e^2}}{na^2 e} \frac{\partial \bar{U}'}{\partial e} \quad (6.35)$$

$$\frac{di}{dt} = \frac{\cos i}{na^2 \sqrt{1-e^2} \sin i} \frac{\partial \bar{U}'}{\partial \omega} - \frac{1}{na^2 \sqrt{1-e^2} \sin i} \frac{\partial \bar{U}'}{\partial \Omega} \quad (6.36)$$

$$\frac{d\Omega}{dt} = \frac{1}{na^2 \sqrt{1-e^2} \sin i} \frac{\partial \bar{U}'}{\partial i} \quad (6.37)$$

$$\frac{dM}{dt} = -\frac{2}{na} \frac{\partial \bar{U}'}{\partial a} - \frac{1-e^2}{na^2 e} \frac{\partial \bar{U}'}{\partial e} \quad (6.38)$$

In our study, the Lagrangian Equation for the semi-major axis a is equal to zero since the mean anomaly, M , disappeared when the disturbing function was averaged over one satellite revolution in Eq. (6.13). To use the five remaining LPEs, the partial derivatives of the disturbing function with respect of the orbital elements e , ω , i , and Ω have to be computed:

$$\frac{\partial \bar{U}'}{\partial e} = \sum_{l=2}^n \sum_{m=0}^l \sum_{p=0}^l \left[\sum_{k=0}^{\lfloor \frac{|l-2p|}{2} \rfloor} \sum_{p'=0}^l \left[K_{lm} T_{lpk} F_{lmp'}(i') F_{lmp}(i) \frac{dI_{lpk}}{de} \cdot \left\{ c_{lmp} \cos \psi_{lmp'} + s_{lmp} \sin \psi_{lmp'} \right\} \right] \right] \quad (6.39)$$

$$\frac{\partial \bar{U}'}{\partial \omega} = \sum_{l=2}^n \sum_{m=0}^l \sum_{p=0}^l \left[\sum_{k=0}^{\lfloor \frac{|l-2p|}{2} \rfloor} \sum_{p'=0}^l \left[K_{lm} T_{lpk} F_{lmp'}(i') F_{lmp}(i) I_{lpk}(e) \cdot \left\{ (l-2p) \left\{ -s_{lmp} \cos \psi_{lmp'} + c_{lmp} \sin \psi_{lmp'} \right\} \right\} \right] \right] \quad (6.40)$$

$$\frac{\partial \bar{U}'}{\partial i} = \sum_{l=2}^n \sum_{m=0}^l \sum_{p=0}^l \sum_{k=0}^{\lfloor \frac{|l-2p|}{2} \rfloor} \sum_{p'=0}^l \left[K_{lm} T_{lpk} F_{lmp'}(i') \frac{dF_{lmp}}{di} I_{lpk}(e) \cdot \right. \\ \left. \{c_{lmp} \cos \psi_{lmp'} + s_{lmp} \sin \psi_{lmp'}\} \right] \quad (6.41)$$

$$\frac{\partial \bar{U}'}{\partial \Omega} = \sum_{l=2}^n \sum_{m=0}^l \sum_{p=0}^l \sum_{k=0}^{\lfloor \frac{|l-2p|}{2} \rfloor} \sum_{p'=0}^l \left[K_{lm} T_{lpk} F_{lmp'}(i') F_{lmp}(i) I_{lpk}(e) \cdot \right. \\ \left. m \{s_{lmp} \cos \psi_{lmp'} - c_{lmp} \sin \psi_{lmp'}\} \right] \quad (6.42)$$

Eq. (6.39) and Eq. (6.41) contains the derivatives of the eccentricity functions I_{lpk} and the derivatives of the inclination functions F_{lmp} respectively. The derivatives of the eccentricity functions I_{lpk} are defined as:

$$\text{if } k < \frac{|l-2p|}{2} : \\ \frac{dI_{lpk}}{de} = \frac{1}{2\pi} \int_0^{2\pi} (1 - e \cos E)^{2k+l-|l-2p|} (\cos E - e)^{|l-2p|-2k-1} \cdot \\ [(2k+l+1-|l-2p|)(e \cos E - \cos^2 E) + (|l-2p|-2k)(e \cos E - 1)] dE \quad (6.43)$$

$$\text{if } k = \frac{|l-2p|}{2} : \\ \frac{dI_{lpk}}{de} = -\frac{1}{2\pi} \int_0^{2\pi} (l+1)(1 - e \cos E)^l \cos E \, dE \quad (6.44)$$

The derivatives of the inclination functions F_{lmp} are defined as:

if $l = m$:

$$\frac{dF_{lmp}}{di} = \sum_{s=1}^m \sum_{c=Max\{0; p-m+s\}}^{Min\{s, p\}} (-1)^c \frac{2l!}{2^{2l} l!} \binom{m}{s} \binom{s}{c} \binom{m-s}{p-c} s \cdot \sin(i) \cos^{s-1}(i) \quad (6.45)$$

if $l - m$ even:

$$\begin{aligned} \frac{dF_{lmp}}{di} = & \sum_{t=0}^{Min\left\{p; \frac{l-m-1}{2}\right\}} \sum_{s=1}^m \sum_{c=Max\{0; p-t-m+s\}}^{Min\{l-m-2t+s, p-t\}} (-1)^{c-\frac{l-m}{2}} \frac{(2l-2t)!}{2^{2l-2t} t!(l-t)!(l-m-2t)!} \cdot \\ & \binom{m}{s} \binom{l-m-2t+s}{c} \binom{m-s}{p-t-c} \sin^{l-m-2t-1}(i) \cos^{s-1}(i) \{(l-m-2t)\cos^2(i) - s \sin^2(i)\} \end{aligned} \quad (6.46)$$

if $l - m$ odd:

$$\begin{aligned} \frac{dF_{lmp}}{di} = & \sum_{t=0}^{Min\left\{p; \frac{l-m-1}{2}\right\}} \sum_{s=1}^m \sum_{c=Max\{0; p-t-m+s\}}^{Min\{l-m-2t+s, p-t\}} (-1)^{c-\frac{l-m-1}{2}} \frac{(2l-2t)!}{2^{2l-2t} t!(l-t)!(l-m-2t)!} \cdot \\ & \binom{m}{s} \binom{l-m-2t+s}{c} \binom{m-s}{p-t-c} \sin^{l-m-2t-1}(i) \cos^{s-1}(i) \{(l-m-2t)\cos^2(i) - s \sin^2(i)\} \end{aligned} \quad (6.47)$$

$$\text{and } \binom{x}{y} \text{ represents the binomial coefficient : } \binom{x}{y} = \frac{x!}{y!(x-y)!} \quad (6.48)$$

Finally, substituting the partial derivatives into the LPEs, we obtain the following expressions for the time derivatives of the orbital elements due to the third body perturbing force only:

$$\frac{da}{dt} = 0 \quad (6.49)$$

$$\frac{de}{dt} = -\frac{\sqrt{1-e^2}}{na^2 e} \sum_{l=2}^n \sum_{m=0}^l \sum_{p=0}^l \sum_{k=0}^{\lfloor \frac{l-2p}{2} \rfloor} \sum_{p'=0}^l \left[K_{lm} T_{lpk} F_{lmp'}(i') F_{lmp}(i) I_{lpk}(e) \cdot \right. \\ \left. (l-2p) \{ -s_{lmp} \cos \psi_{lmp'} + c_{lmp} \sin \psi_{lmp'} \} \right] \quad (6.50)$$

$$\frac{d\omega}{dt} = \sum_{l=2}^n \sum_{m=0}^l \sum_{p=0}^l \sum_{k=0}^{\lfloor \frac{l-2p}{2} \rfloor} \sum_{p'=0}^l \left[K_{lm} T_{lpk} F_{lmp'}(i') \{ c_{lmp} \cos \psi_{lmp'} + s_{lmp} \sin \psi_{lmp'} \} \cdot \right. \\ \left. \left(\frac{\sqrt{1-e^2}}{na^2 e} F_{lmp}(i) \frac{dI_{lpk}}{de} - \frac{\cos i}{na^2 \sqrt{1-e^2} \sin i} \frac{dF_{lmp}}{di} I_{lpk}(e) \right) \right] \quad (6.51)$$

$$\frac{di}{dt} = \frac{1}{na^2 \sqrt{1-e^2} \sin i} \sum_{l=2}^n \sum_{m=0}^l \sum_{p=0}^l \sum_{k=0}^{\lfloor \frac{l-2p}{2} \rfloor} \sum_{p'=0}^l \left[K_{lm} T_{lpk} F_{lmp'}(i') F_{lmp}(i) I_{lpk}(e) \cdot \right. \\ \left. ((l-2p) \cos i + m) \{ -s_{lmp} \cos \psi_{lmp'} + c_{lmp} \sin \psi_{lmp'} \} \right] \quad (6.52)$$

$$\frac{d\Omega}{dt} = \frac{1}{na^2 \sqrt{1-e^2} \sin i} \sum_{l=2}^n \sum_{m=0}^l \sum_{p=0}^l \sum_{k=0}^{\lfloor \frac{l-2p}{2} \rfloor} \sum_{p'=0}^l \left[K_{lm} T_{lpk} F_{lmp'}(i') \frac{dF_{lmp}}{di} I_{lpk}(e) \cdot \right. \\ \left. \{ c_{lmp} \cos \psi_{lmp'} + s_{lmp} \sin \psi_{lmp'} \} \right] \quad (6.53)$$

$$\frac{dM}{dt} = -\frac{1-e^2}{na^2 e} \sum_{l=2}^n \sum_{m=0}^l \sum_{p=0}^l \sum_{k=0}^{\lfloor \frac{l-2p}{2} \rfloor} \sum_{p'=0}^l \left[K_{lm} T_{lpk} F_{lmp'}(i') F_{lmp}(i) \frac{dI_{lpk}}{de} \cdot \right. \\ \left. \{ c_{lmp} \cos \psi_{lmp'} + s_{lmp} \sin \psi_{lmp'} \} \right] \quad (6.54)$$

6.3 APPLICATION TO A SIMPLIFIED CASE

In this section, we apply the Lagrangian equations in Eq. (6.49) through Eq. (6.53) to the mean orbital elements of ICESat 91-day repeat groundtrack orbit in order to study the perturbations due to the Moon and to the Sun. For both the perturbations due to the Moon and the perturbations due to the Sun, the Earth is defined as the main body. In a first approach we simplify the 3-body configuration by assuming that the third body's motion, or its apparent motion in an Earth Centered Inertial frame (ECI), is a circular orbit in the equatorial plane of the Earth. The time rates of the third body's orbital elements are being neglected. Furthermore, in the case of a third body in a circular orbit, the third body's true anomaly, f' , is a linear function of time and can be easily propagated in time along with ICESat's mean orbital elements. Table (6.1) summarizes ICESat's initial mean orbital elements and the third body's orbital elements at the epoch t_0 for the propagation. To study the perturbations due to the Moon, the ICESat orbital elements are propagated over a 28 days time interval. In the case of the Sun, the propagation is performed over 365 days. Two propagations for both the Moon and the Sun were performed. The first propagation is performed the disturbing function truncated to the 2nd degree, i.e. $n = 2$ in Eq. (6.13). For the second propagation, the disturbing function is truncated to the 4th degree. Due to the complexity of Eq. (6.50) to Eq. (6.54), all the propagations of these equations were made using a very elementary fixed step integrator based on the Newton method (forward difference). The size of the step was manually adjusted to fit the steepest sections of the plot while keeping the process time reasonable.

Orbital elements and epochs	ICESat	Moon	Sun
Semi-major axis	6970.238 km	$3.844 \cdot 10^{-5}$ km	$1.496 \cdot 10^{-8}$ km
Eccentricity	0.0013	0	0
Inclination	94°	0°	0°
Argument of Perigee	90°	0°	0°
Line of Node	0°	0°	0°
True Anomaly	N/A	0°	0°
t_0	N/A	0 sec	0 sec
t_f	N/A	2432093.63 sec	31704077.63 sec

Table 6.1: Initial conditions for the propagation of ICESat's orbital elements in the simplified case of the third in the equatorial plane.

Fig. (6.1) through Fig (6.3) show the evolution of ICESat mean orbital elements ($e \cos \omega$, $e \sin \omega$, i , and Ω) under the 3rd body influence of the Sun and with a disturbing function expanded up to the 2nd degree. On Fig (6.1), the eccentricity vector exhibits a twice per year oscillation. The amplitude of the oscillations is equal to $6 \cdot 10^{-8}$ in the sine direction. The drift along the cosine direction is equal to $1.7 \cdot 10^{-6}$. On Fig (6.2), we observe that the inclination also exhibits oscillations with a period half the one of the Sun. The amplitude of the oscillations of the inclination is $8 \cdot 10^{-3}$ degree which corresponds to a groundtrack shift at the apex equal to 890 meters which exceeds the 800 meters tolerance for the groundtrack drift according to the ICESat mission requirements. Finally, Fig (6.3) shows the evolution of ICESat's argument of the node. The argument of the node increases linearly throughout the entire apparent revolution of the Sun. The

slope of the drift computed via a linear fitting of the data is about $9.6 \cdot 10^{-6}$ degree per day which leads to a groundtrack drift at the equator of 390 meters after a year.

Fig. (6.4) through Fig (6.6) show the difference between the 4th degree and 2nd degree computation in the evolutions of ICESat eccentricity vector, inclination and argument of the node with the Sun acting as the perturbing 3rd body. The correction brought to the eccentricity vector is in the order of 10^{-9} . The correction to the inclination oscillations is in the order of 10^{-10} degree. Finally the correction for the line of node is 10^{-9} degree. In the case of Sun, it is therefore reasonable to consider only the second degree of the disturbing function's expansion.

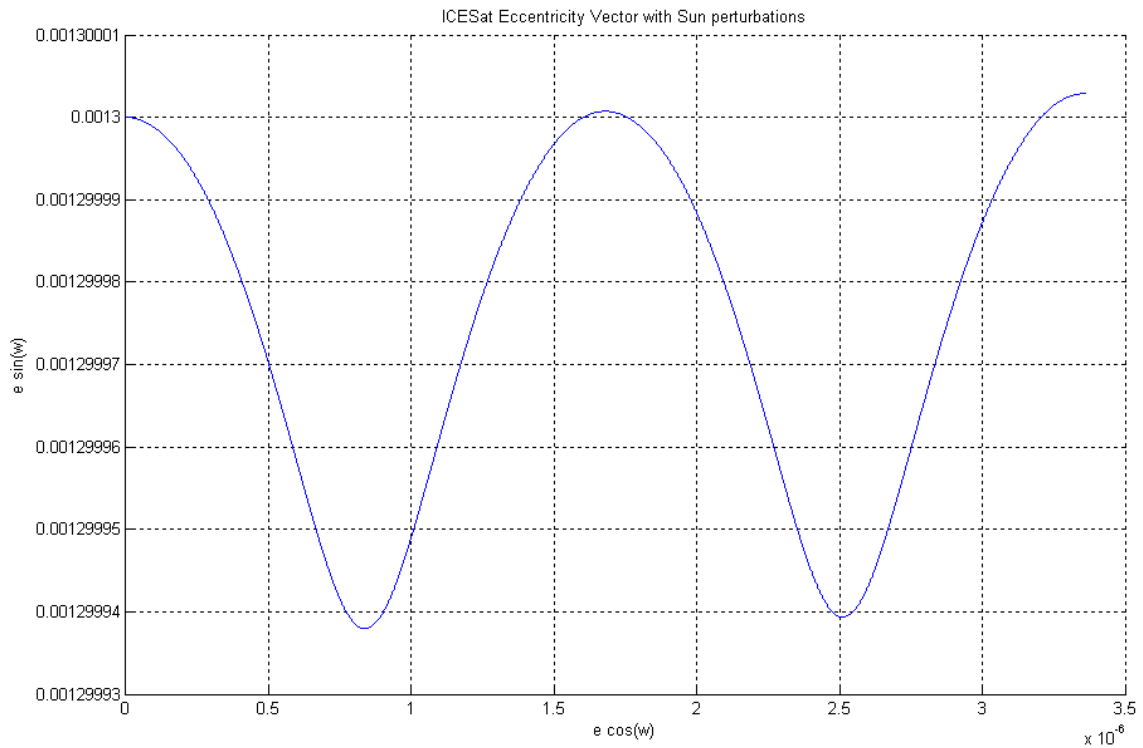


Figure 6.1: Perturbations of ICESat eccentricity vector due to the Sun propagated over 365 days with a disturbing function expanded to the 2nd degree.

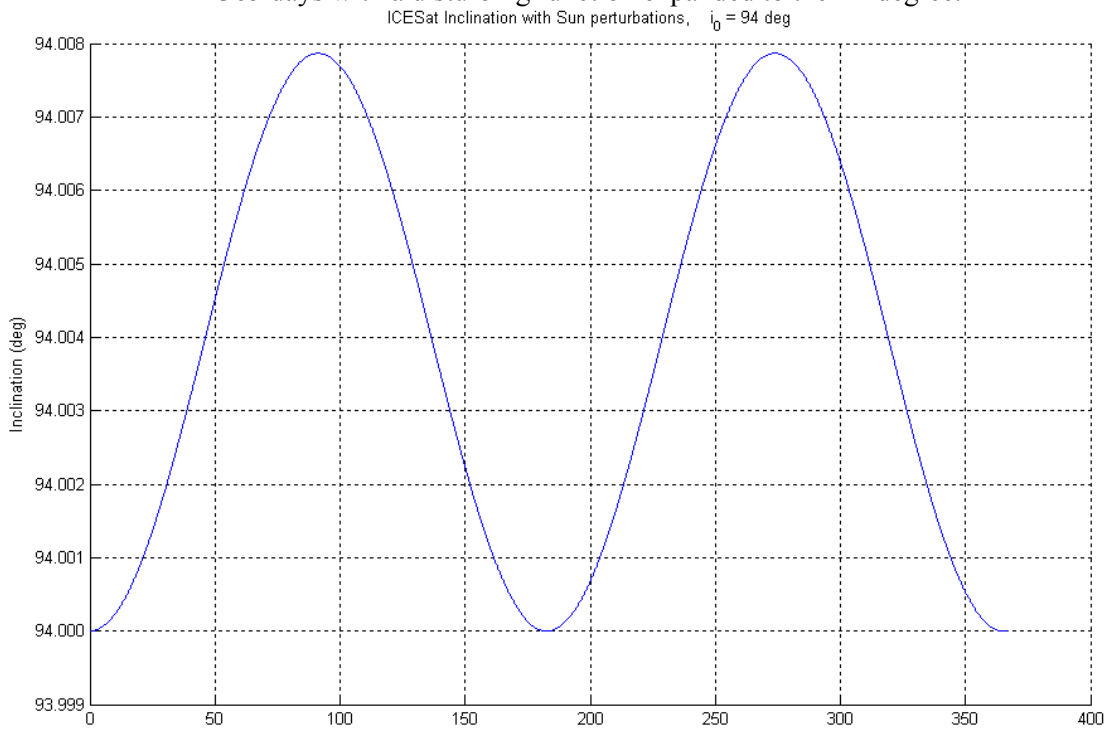


Figure 6.2: Perturbations of ICESat inclination due to the Sun propagated over 365 days with a disturbing function expanded to the 2nd degree.

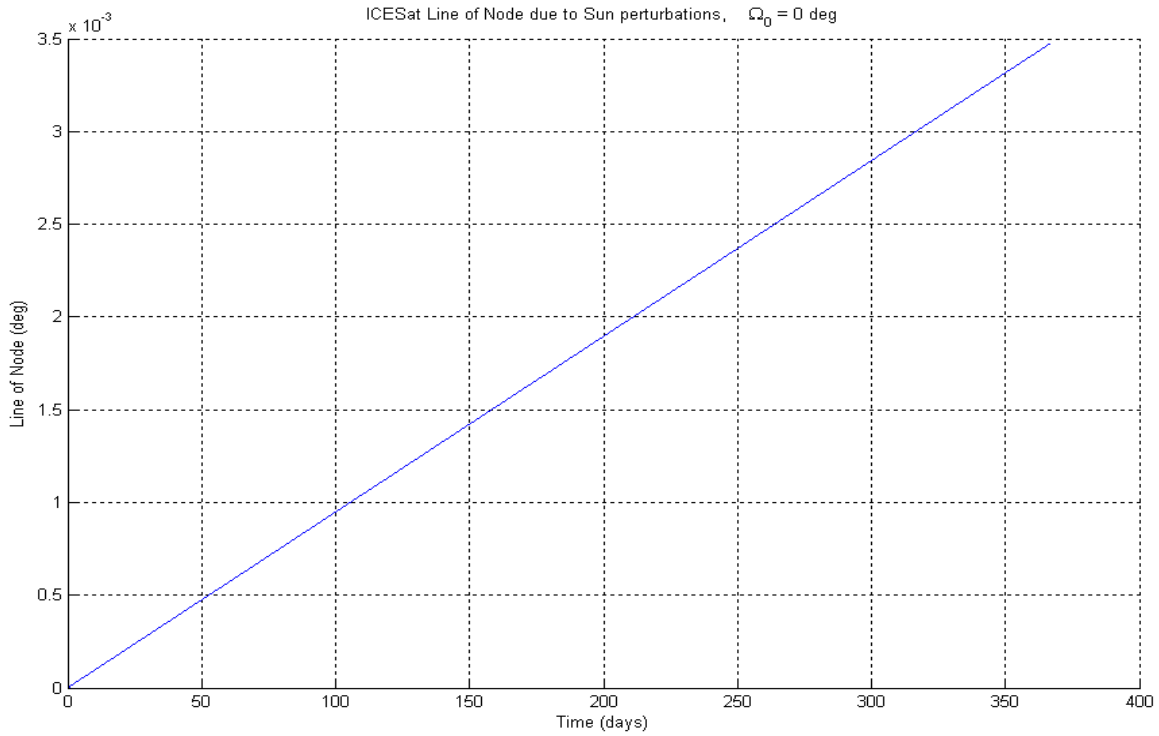


Figure 6.3: Perturbations of ICESat line of node due to the Sun propagated over 365 days with a disturbing function expanded to the 2nd degree.

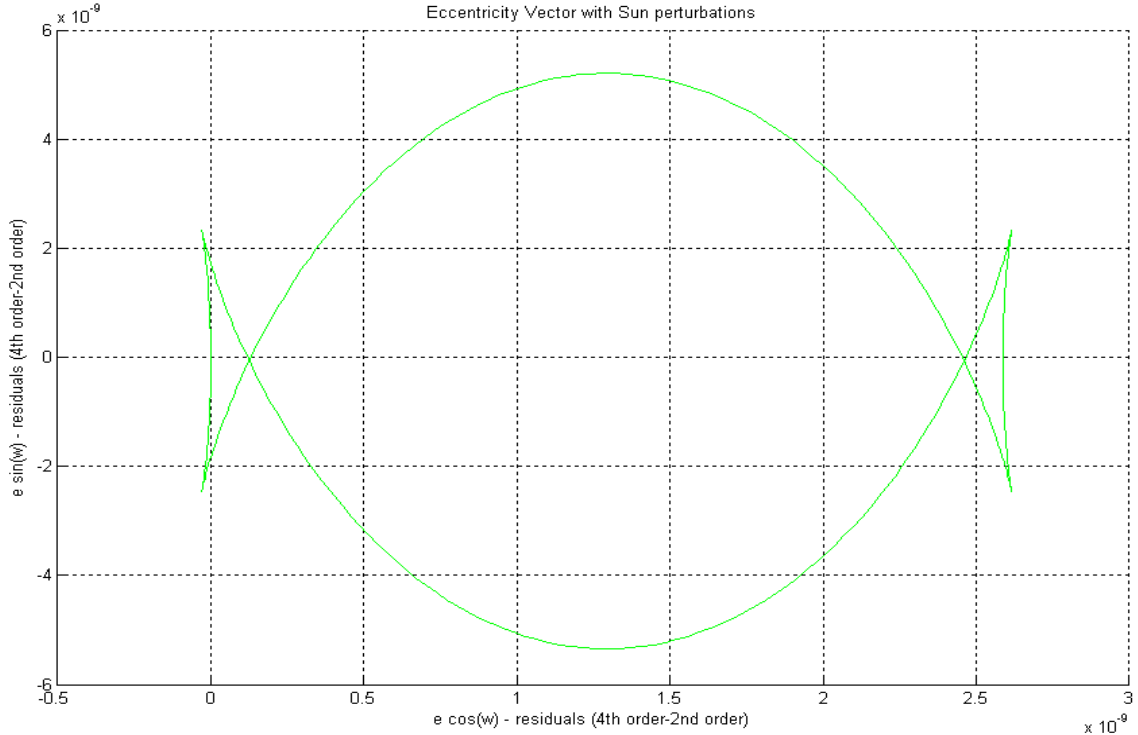


Figure 6.4: Perturbations of ICESat eccentricity vector due to the Sun propagated over 365 days: comparison between the 4th degree and 2nd degree.

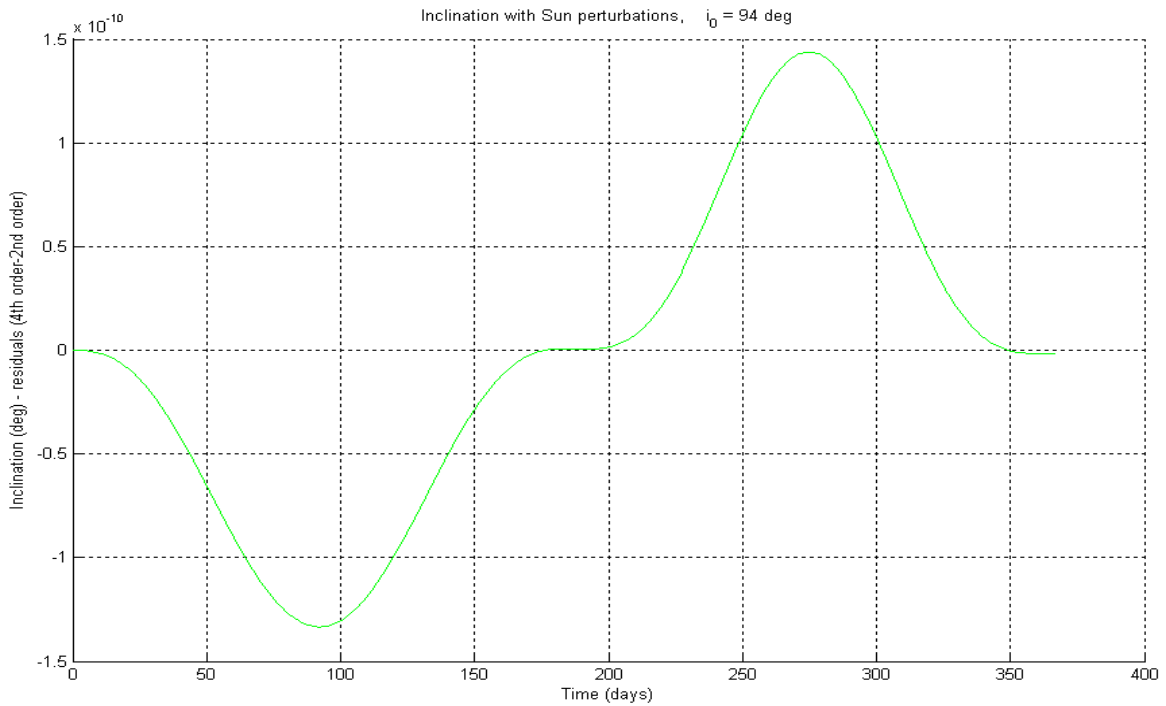


Figure 6.5: Perturbations of ICESat inclination due to the Sun propagated over 365 days: comparison between the 4th degree and 2nd degree.

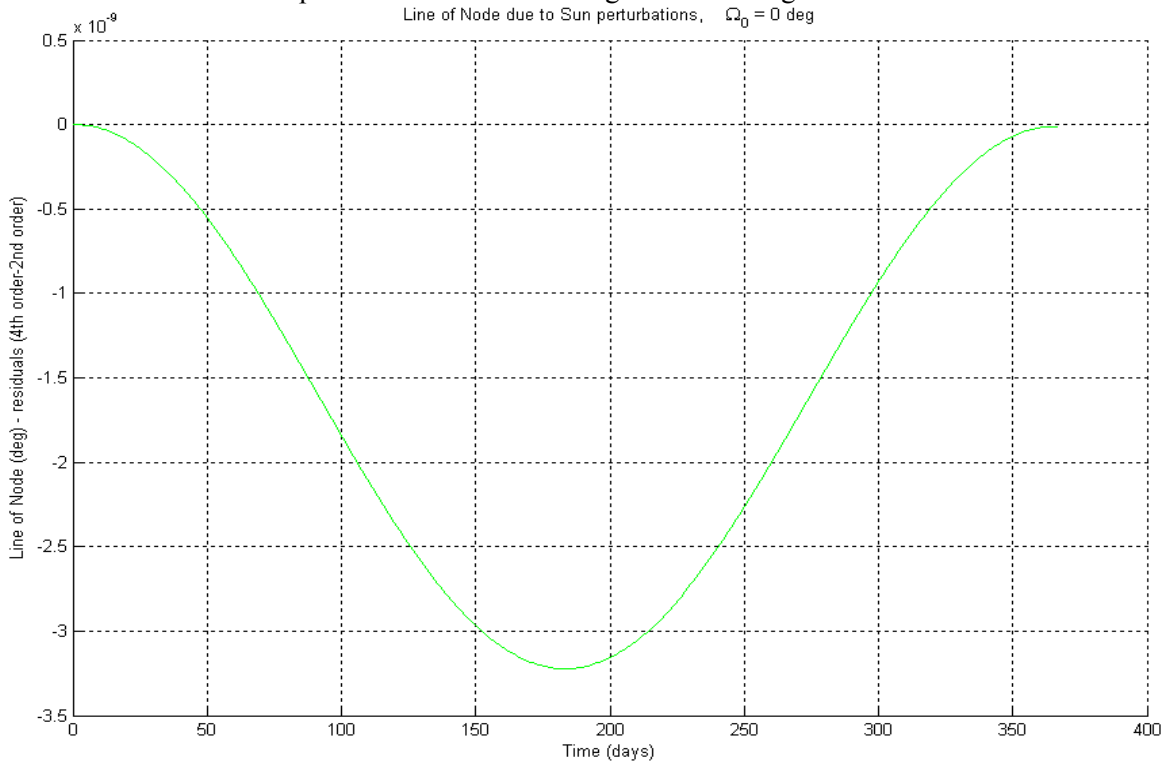


Figure 6.6: Perturbations of ICESat line of node due to the Sun propagated over 365 days: comparison between the 4th degree and 2nd degree.

Fig (6.7) through Fig (6.9) show the evolution of ICESat mean orbital elements ($e \cos \omega$, $e \sin \omega$, i , and Ω) under the 3rd body influence of the Moon and with a disturbing function expanded up to the 2nd degree. On Fig (6.10), the eccentricity vector exhibit the same general trend as in the case of the Sun. The period of the oscillations is half the one of the Moon. The amplitude of the oscillations in the cosine direction is equal to 10^{-8} and the drift along the sine direction is equal to $2.5 \cdot 10^{-7}$. On Fig (6.8), we observe that, like in the case of the Sun, the inclination values oscillate twice per revolution of the Moon. The amplitude of the oscillations of the inclination is $1.23 \cdot 10^{-3}$ degree which corresponds to a drift of the groundtrack at the apex equal to 137 meters. Finally Fig (6.9) shows the evolution of ICESat's argument of the node. Just like in the case of the Sun, the argument of the node increases linearly throughout the entire revolution of the Moon. The slope of the drift on Fig (6.9) is greater than the one observed on Fig (6.3). By performing a linear fitting of the argument of the node values, we find that the slope is about $2.0 \cdot 10^{-5}$ degree per day which is twice the value of the slope on Fig (6.3) for the case of the Sun.

Fig. (6.10) through Fig (6.12) show the difference between the 4th degree and 2nd degree computation in the evolutions of ICESat eccentricity vector, inclination and argument of the node with the Sun acting as the perturbing 3rd body. Contrary to the case of the Sun, the 4th degree expansion of the disturbing function for the Moon as the third body brings noticeable change in the evolution of the eccentricity vector. The correction brought to the eccentricity vector is in the order of $4 \cdot 10^{-7}$ in the sine direction and in the order of $1.6 \cdot 10^{-8}$ in the cosine direction. However, the amplitude of the oscillations

remains negligible compared to the mean value of the eccentricity. The correction to the inclination oscillations is in the order of 10^{-7} degree. Finally the correction for the line of node is $3 \cdot 10^{-7}$ degree. . Like in the case of the Sun, it is therefore reasonable to consider only the second degree in the expansion of the Moon's disturbing function.

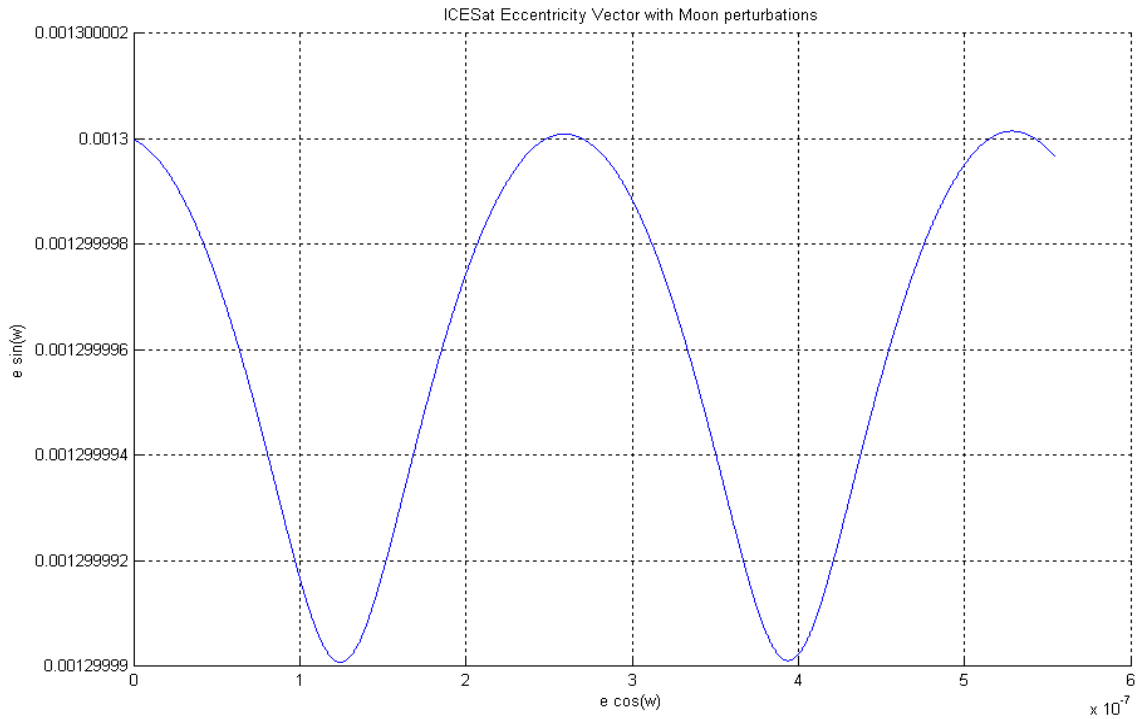


Figure 6.7: Perturbations of ICESat eccentricity vector due to the Moon propagated over 28 days with a disturbing function expanded to the 2nd degree.

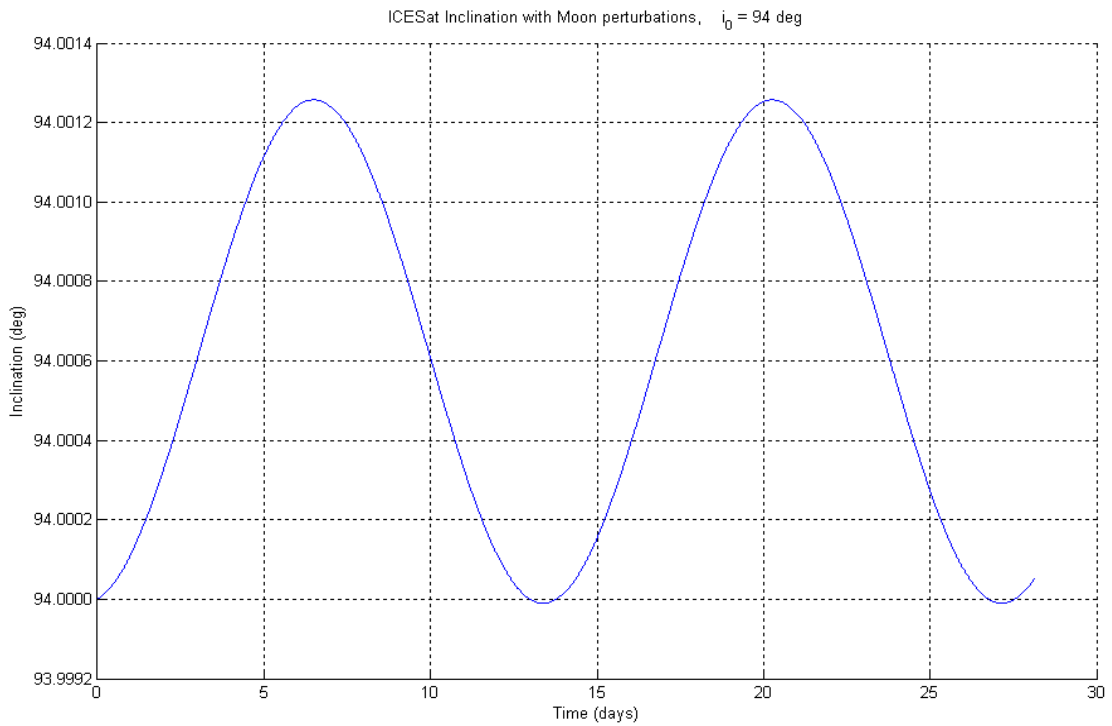


Figure 6.8: Perturbations of ICESat inclination due to the Moon propagated over 28 days with a disturbing function expanded to the 2nd degree.

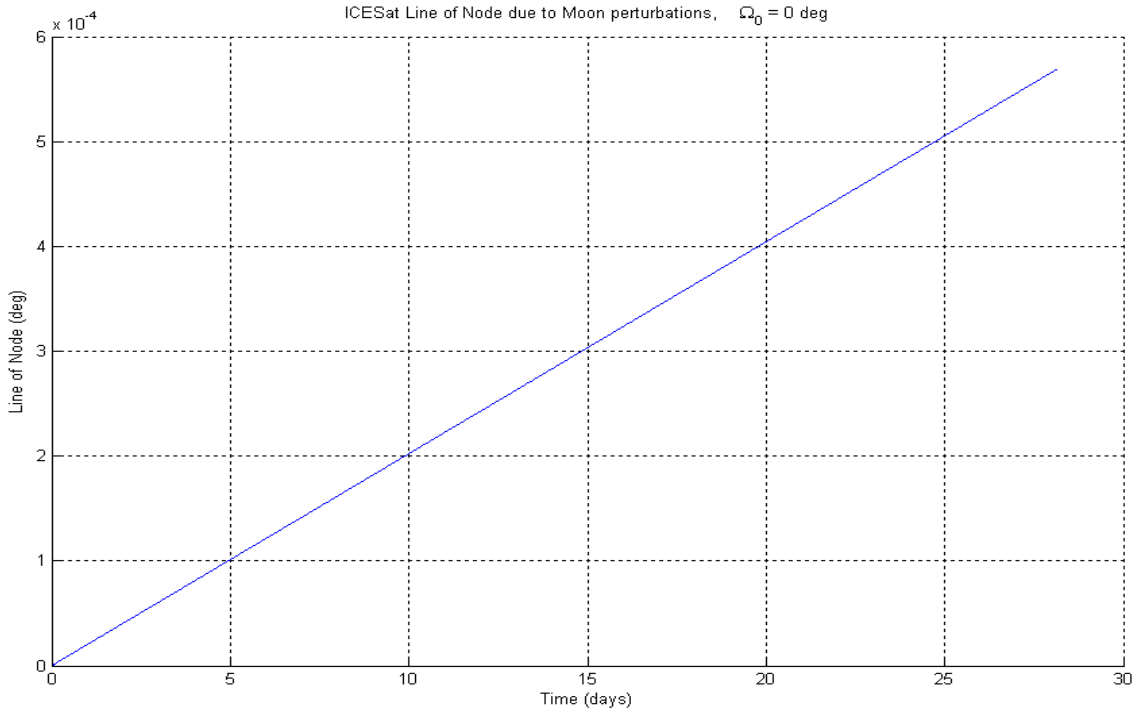


Figure 6.9: Perturbations of ICESat line of node due to the Moon propagated over 28 days with a disturbing function expanded to the 2nd degree.

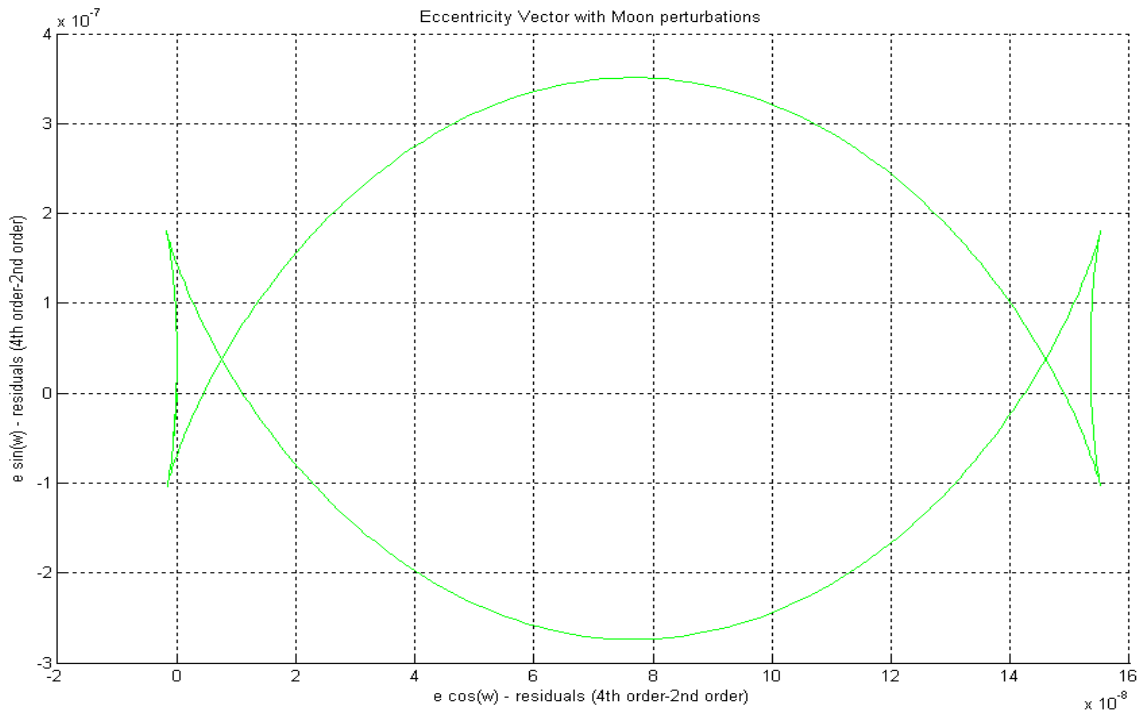


Figure 6.10: Perturbations of ICESat eccentricity vector due to the Moon propagated over 28 days: comparison between the 4th degree and 2nd degree.

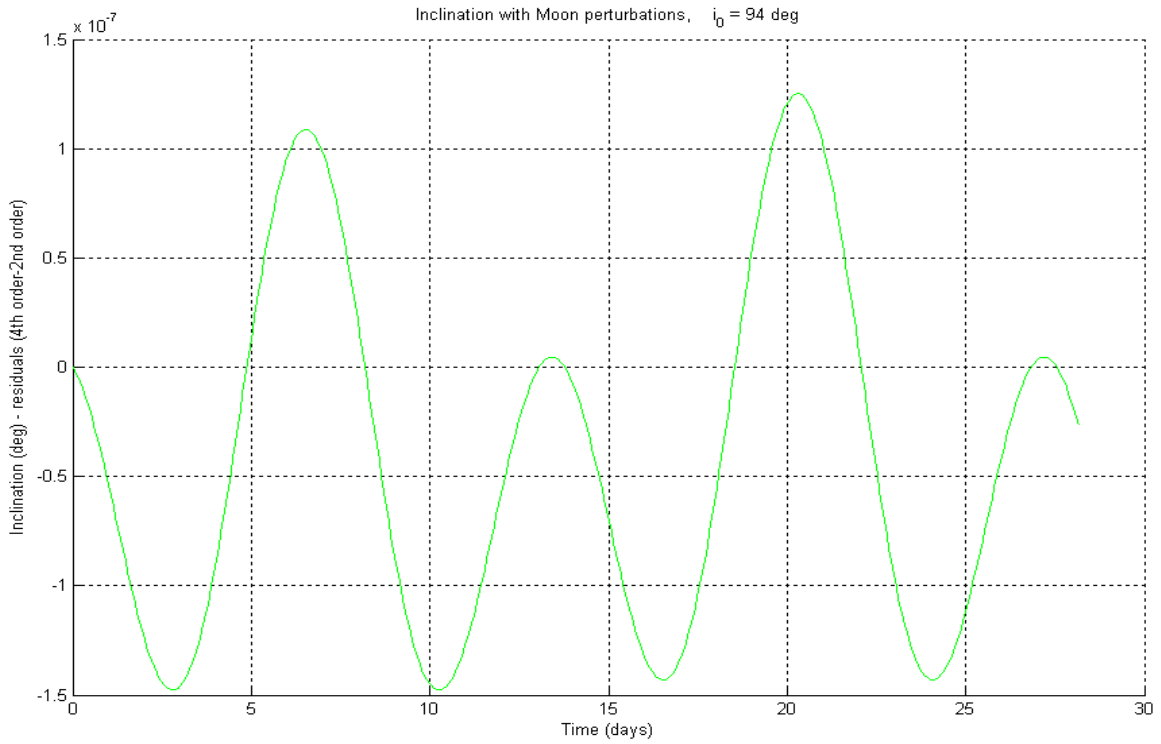


Figure 6.11: Perturbations of ICESat inclination due to the Moon propagated over 28 days: comparison between the 4th degree and 2nd degree.

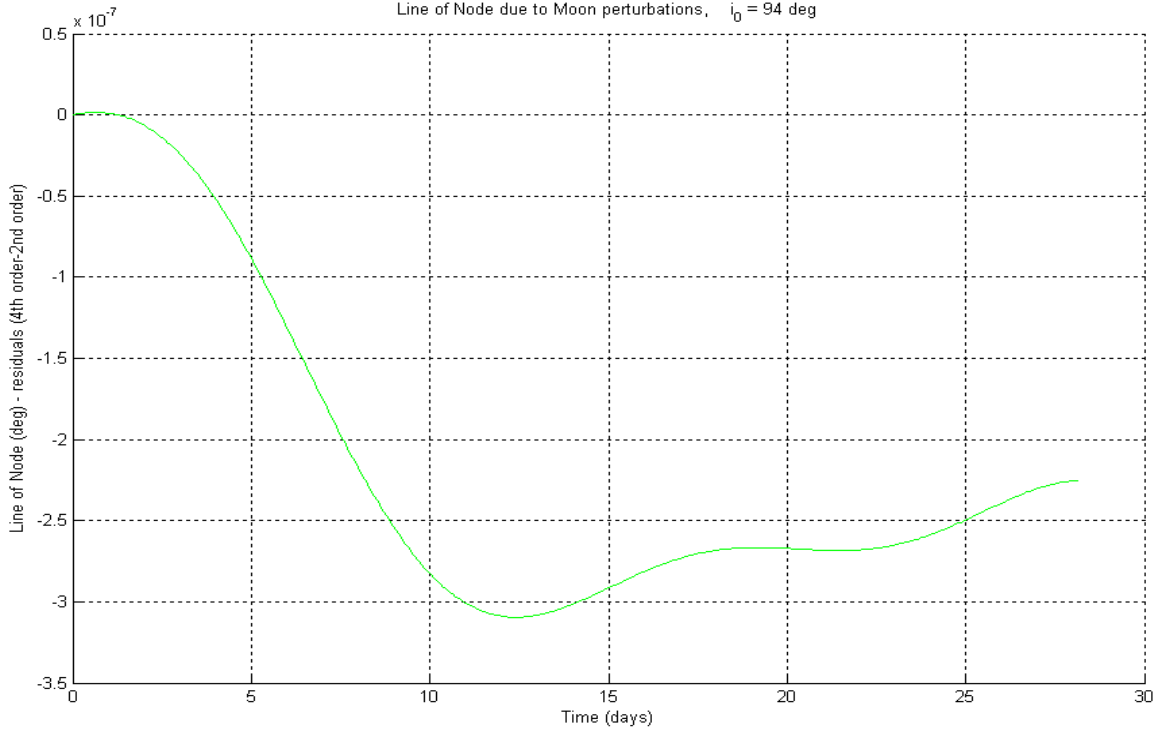


Figure 6.12: Perturbations of ICESat line of node due to the Moon propagated over 28 days: comparison between the 4th degree and 2nd degree.

6.4 DOUBLE-AVERAGE DISTURBING FUNCTION

In the section before, we have presented the evolution of the ICESat mean orbital elements that are affected by the third body effect according to the LPEs in Eq. (6.49) through Eq. (6.53). The disturbing potential was a single-average function since it was obtained after performing an average over one satellite revolution in Eq. (6.13). However, a double-average disturbing function is frequently used to study the third body perturbations (Broucke, 2003), (Prado, 2003), (Folta and Quinn, 2006). This double-average disturbing function is often given under the assumption that the third body is in a circular orbit around the main body in the XY-plane, where X and Y refer to two of three direction of an inertial frame centered on the main body. The spacecraft on the other hand is assumed to be in a 3-dimensional Keplerian orbit around the main body. This description of the problem is identical to the one given in our simplified example in the previous section. Under the previous assumptions, the double-average disturbing function truncated after the 2nd degree is equal to:

$$\overline{\overline{U}}_2 = \frac{1}{32} \mu' n'^2 a^2 \left[(1 + 3 \cos 2i)(2 + 3e^2) + 30e^2 \sin^2 i \cos 2\omega \right] \quad (6.55)$$

We use the potential in Eq. (6.55) to verify the results obtain in the previous section for the ICESat orbital elements under the influence of the Sun and the Moon. The new LPEs used to propagate the orbital elements are:

$$\frac{da}{dt} = 0 \quad (6.56)$$

$$\frac{de}{dt} = \frac{15}{8} \mu' \frac{n'^2}{n} e \sqrt{1-e^2} \sin^2 i \sin 2\omega \quad (6.57)$$

$$\frac{d\omega}{dt} = \frac{3}{16} \mu' \frac{n'^2}{n} \frac{1}{\sqrt{1-e^2}} \left[(3 + 2e^2 + 5 \cos i) + 5(1 - 2e^2 - \cos 2i) \cos 2\omega \right] \quad (6.58)$$

$$\frac{di}{dt} = -\frac{15}{16} \mu' \frac{n'^2}{n} \frac{e^2}{\sqrt{1-e^2}} \sin 2i \sin 2\omega \quad (6.59)$$

$$\frac{d\Omega}{dt} = \frac{3}{8} \mu' \frac{n'^2}{n} \frac{1}{\sqrt{1-e^2}} (5e^2 \cos 2\omega - 3e^2 - 2) \cos i \quad (6.60)$$

The results obtained with this double-average disturbing function, for both the Sun and the Moon, are shown on Fig. (6.13) through Fig. (6.18). To get a better understanding of the evolution of the mean orbital elements of a satellite under the influence of a third body disturbance, we look at the long-term effect of the Sun and the Moon (separately) on ICESat's 91-day repeat orbit. The propagation is performed over 21552 years in the case of the Sun and 10091 years for the Moon using the MATLAB built-in Runge-Kutta 45 integrator. Though these durations are not relevant in the context of a satellite mission, the propagation of the orbital elements over these long time intervals give valuable insight of their behaviors over a shorter time interval by giving them a more global context. The plots obtained for the inclination and eccentricity in the equatorial cases are consistent with the ones obtained by Prado (2003), Broucke (2003) or Solórzano and Prado (2004).

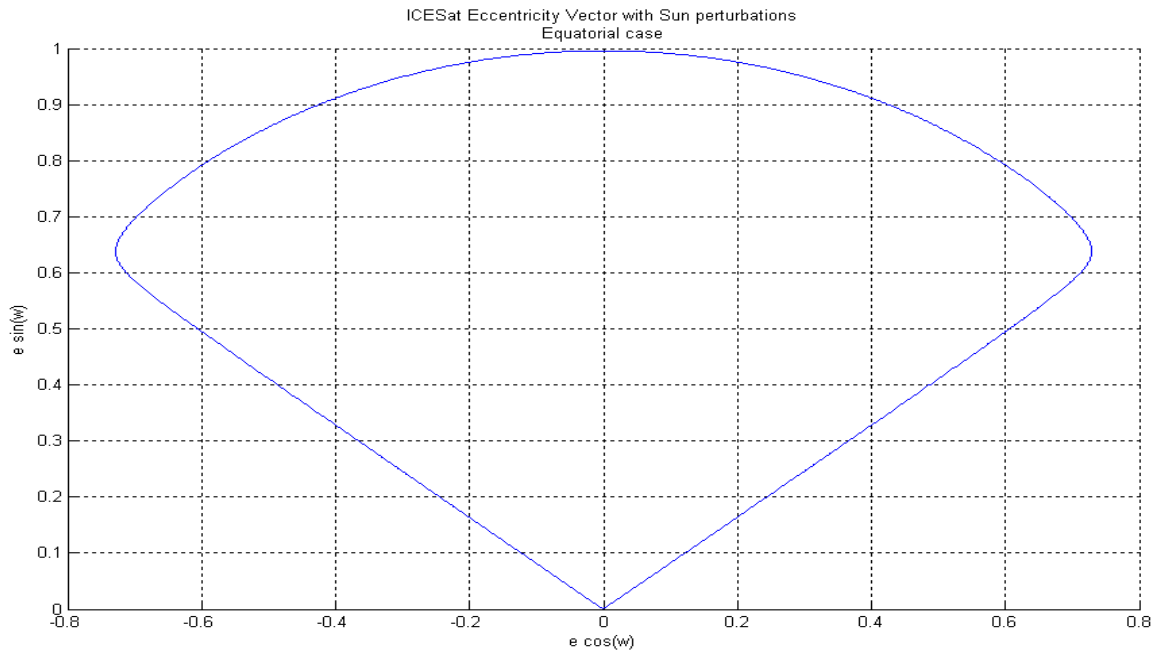


Figure 6.13: ICESat eccentricity vector due to the Sun over 21552 years in the hypothetical case of the Sun in the equatorial plane. The eccentricity describes the above cycle three times over.

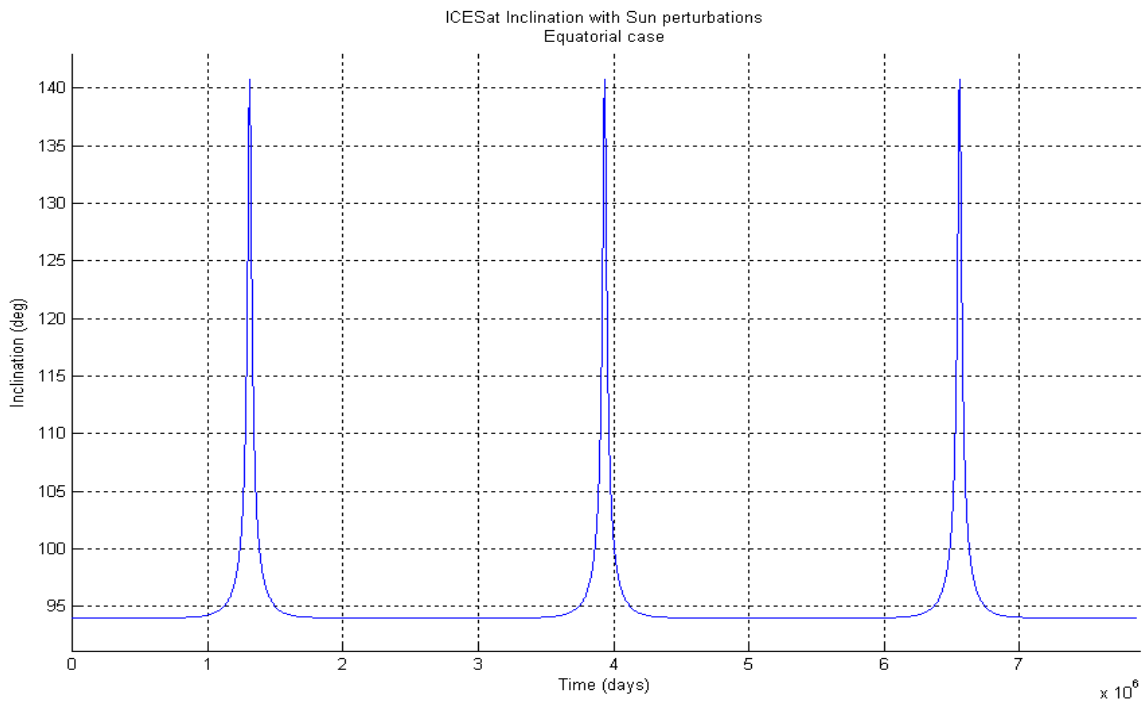


Figure 6.14: ICESat inclination due to the Sun over 21552 years in the hypothetical case of the Sun in the equatorial plane.

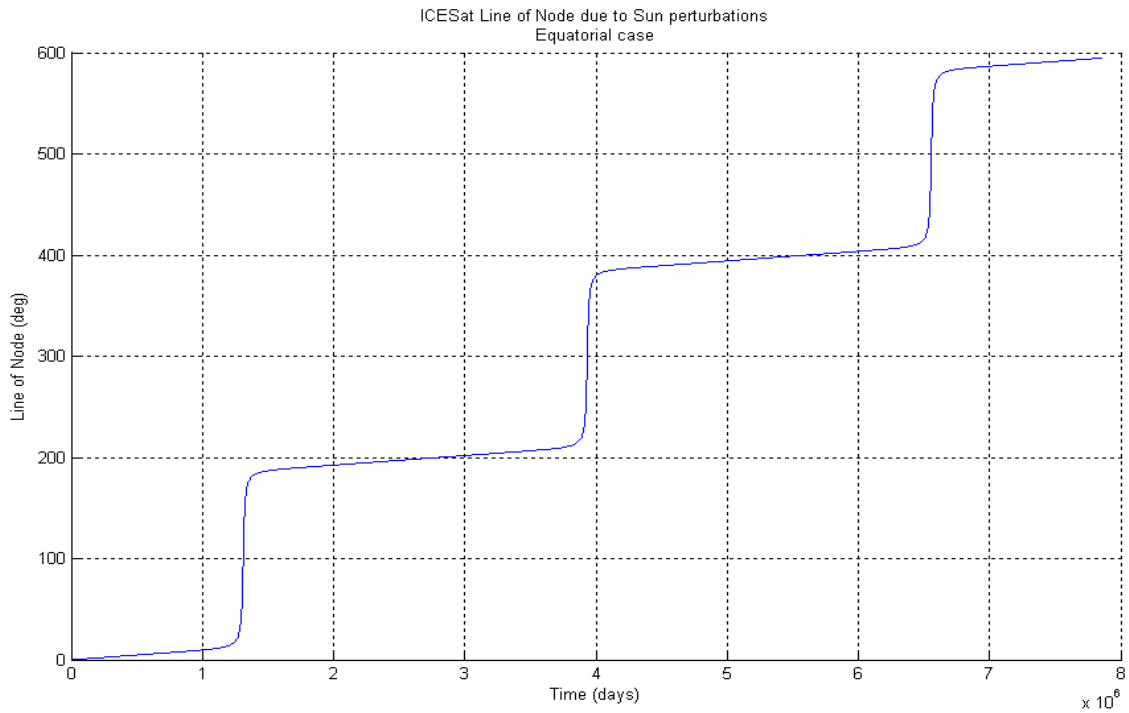


Figure 6.15: ICESat line of node due to the Sun over 21552 years in the hypothetical case of the Sun in the equatorial plan

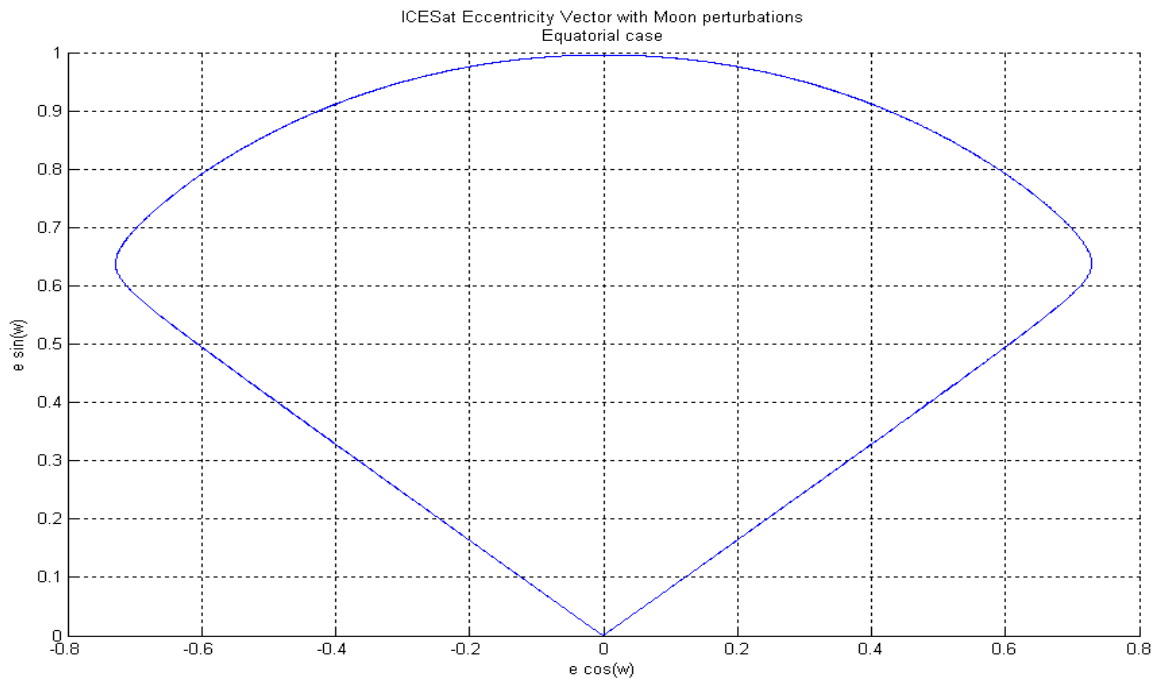


Figure 6.16: ICESat eccentricity vector due to the Moon over 10091 years in the hypothetical case of the Moon in the equatorial plane. The eccentricity describes the above cycle three times over.

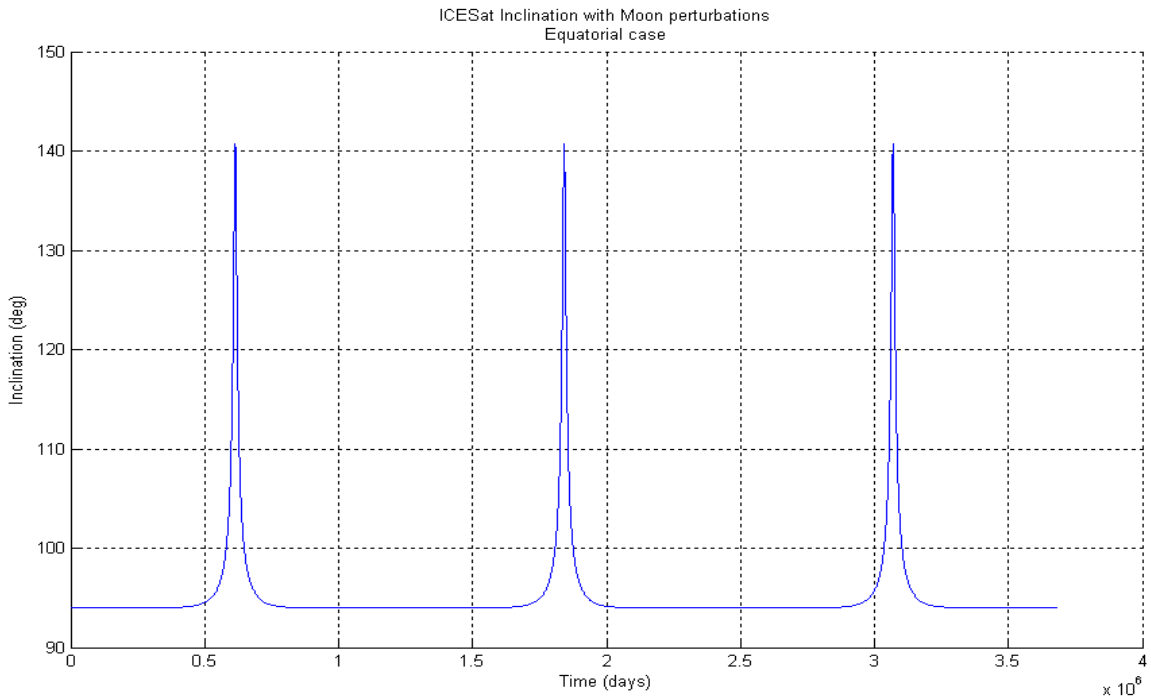


Figure 6.17: ICESat inclination due to the Moon over 10091 years in the hypothetical case of the Moon in the equatorial plane.

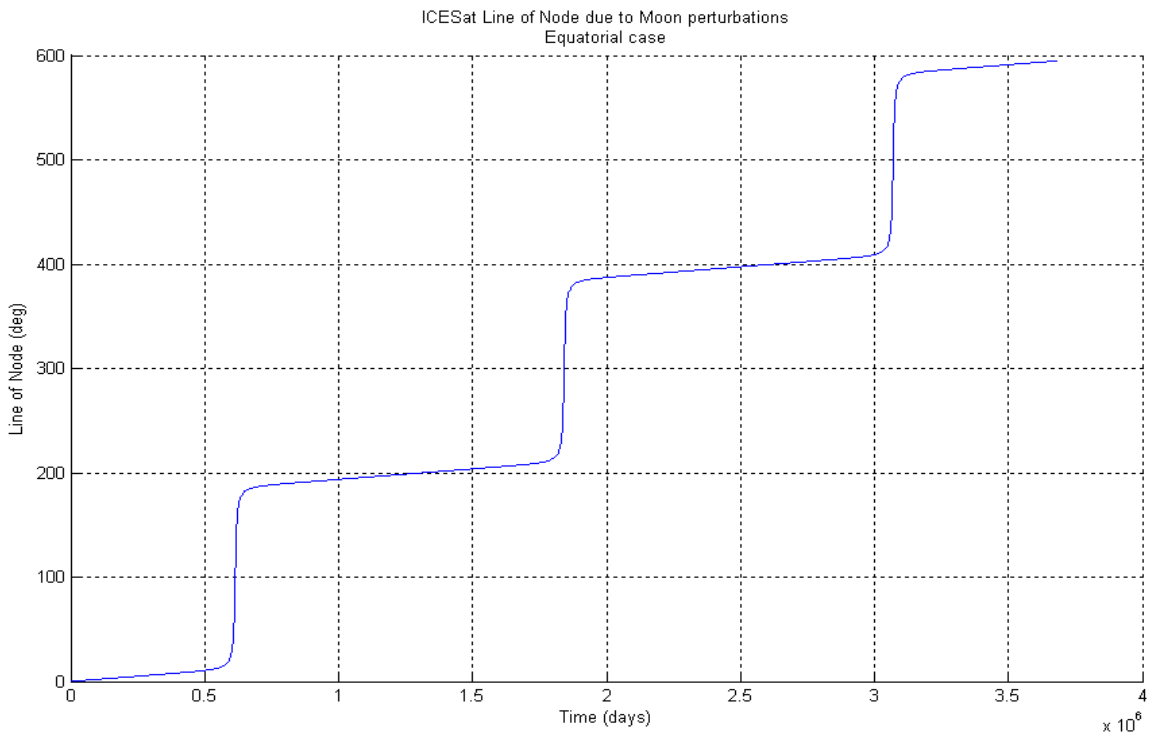


Figure 6.18: ICESat line of node due to the Moon over 10091 years in the hypothetical case of the Moon in the equatorial plane.

6.5 THIRD BODY IN INCLINED ORBITAL PLANE

In the two previous sections, it was assumed that the motion of the third body was in the Earth equatorial plane. We now look at the effect of the inclination of third body on the evolution of ICESat mean orbital elements e , ω , i , and Ω . To do so, the disturbing function in Eq. (6.30) is averaged over one complete revolution of the third body. The third body is still considered to be in a circular motion around the Earth. Therefore, its semi-major axis is constant, its eccentricity is set to 0 and the average is performed by integration over its mean anomaly M' , with $M' = \omega' + f'$ in the case of a circular orbit: The double-average disturbing function in this case is:

$$\overline{\overline{U}}' = \sum_{l=2}^{\infty} \sum_{m=0}^l \sum_{p=0}^l \sum_{k=0}^{\lfloor \frac{|l-2p|}{2} \rfloor} \sum_{p'=0}^l \overline{\overline{U}}'_{lmpkp'} \quad (6.61)$$

$$\overline{\overline{U}}'_{lmpkp'} = K_{lm} T_{lpk} F_{lmp'}(i') F_{lmp}(i) I_{lpk}(e) \cdot \text{sinc}((l-2p')\pi) \{c_{lmp} \cos((l-2p')\pi + m\Omega') + s_{lmp} \sin((l-2p')\pi + m\Omega')\} \quad (6.62)$$

where $\text{sinc}(x) = \frac{\sin(x)}{x}$ if $x \neq 0$, and $\text{sinc}(0) = 1$

As in the previous section, the propagation of the orbital elements is performed over 21552 years in the case of the Sun and 10091 years for the Moon. For numerical efficiency purposes, the propagations of ICESat's orbital elements over these extended time interval are performed using the expansion truncated after the 2nd degree of the double average disturbing given in Eq. (6.61).

The inclination of the Sun is assumed to be constant and equal to the ecliptic value $23^{\circ}26'$. The inclination of the Moon was approximated to the ecliptic. The Moon orbit plane actually oscillates with an amplitude of $\pm 5^{\circ}$ about the ecliptic plane with a period of 18.04 years (Saros Cycle).

In the previous section, it was shown that for both the Sun and the Moon cases, the long term evolutions of the orbital elements are periodic when the perturbing third body is in the equatorial plane (with a periodic additional offset in the case of the argument of perigee). The long-term periodicity disappears completely for the eccentricity and the inclination when the third body is assumed to be orbiting in an inclined plane (namely the ecliptic plane in our case). The argument of node is also modified, but it retains its pseudo-periodic characteristic.

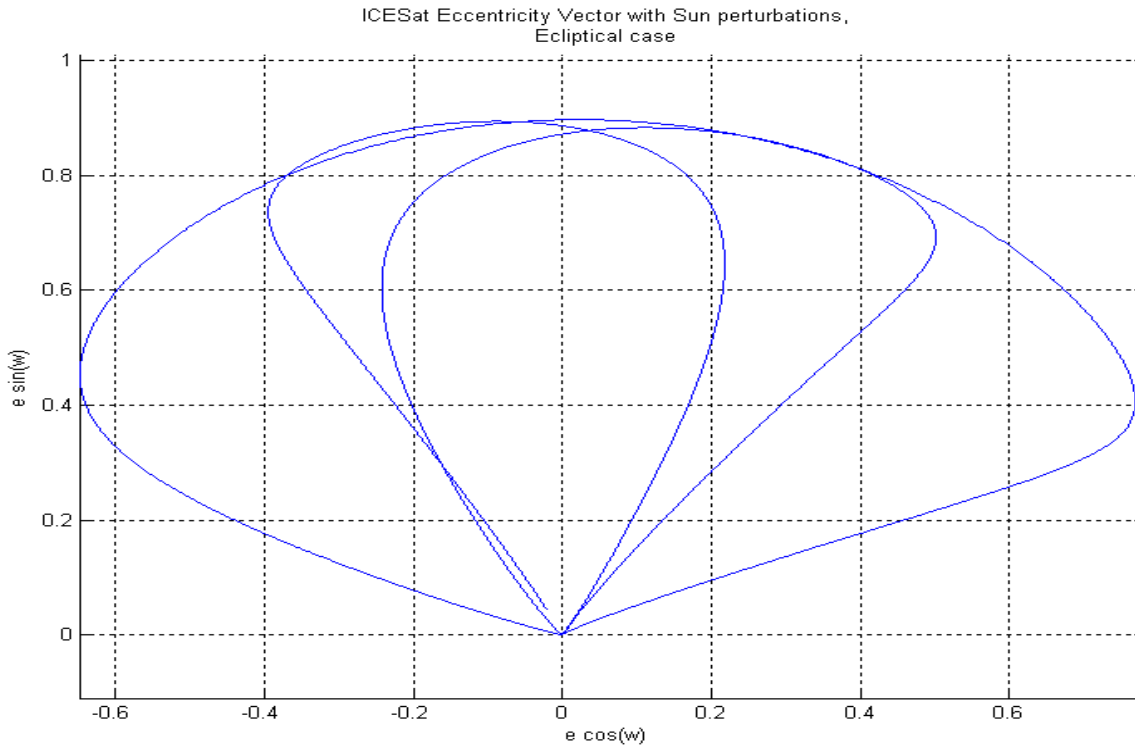


Figure 6.19: ICESat eccentricity vector due to the Sun over 2152 years with the Sun in the ecliptic plane.

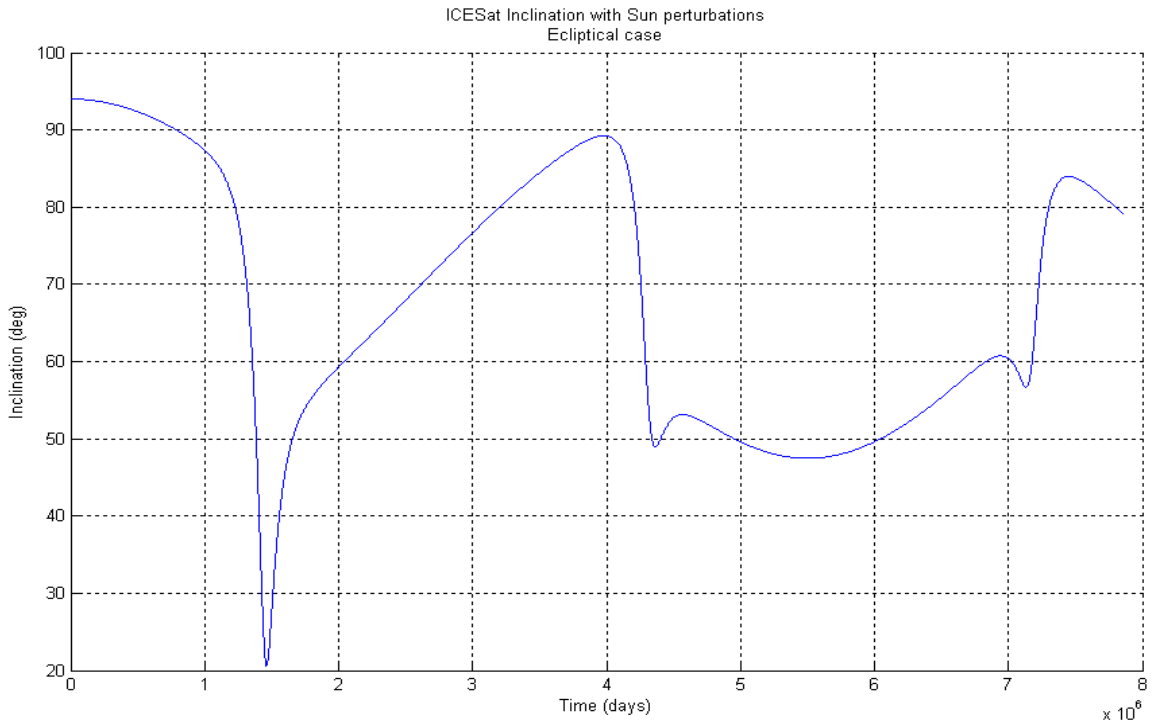


Figure 6.20: ICESat inclination due to the Sun over 2152 years with the Sun in the ecliptic plane.

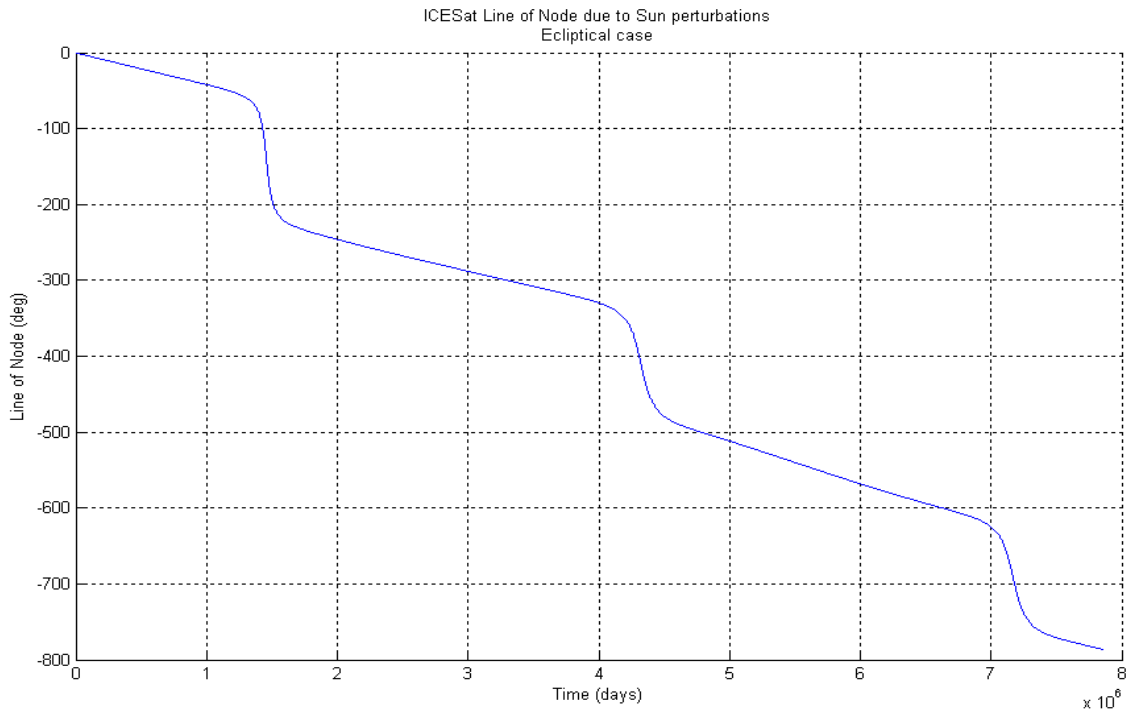


Figure 6.21: ICESat line of node due to the Sun over 21552 years with the Sun in the ecliptic plane.

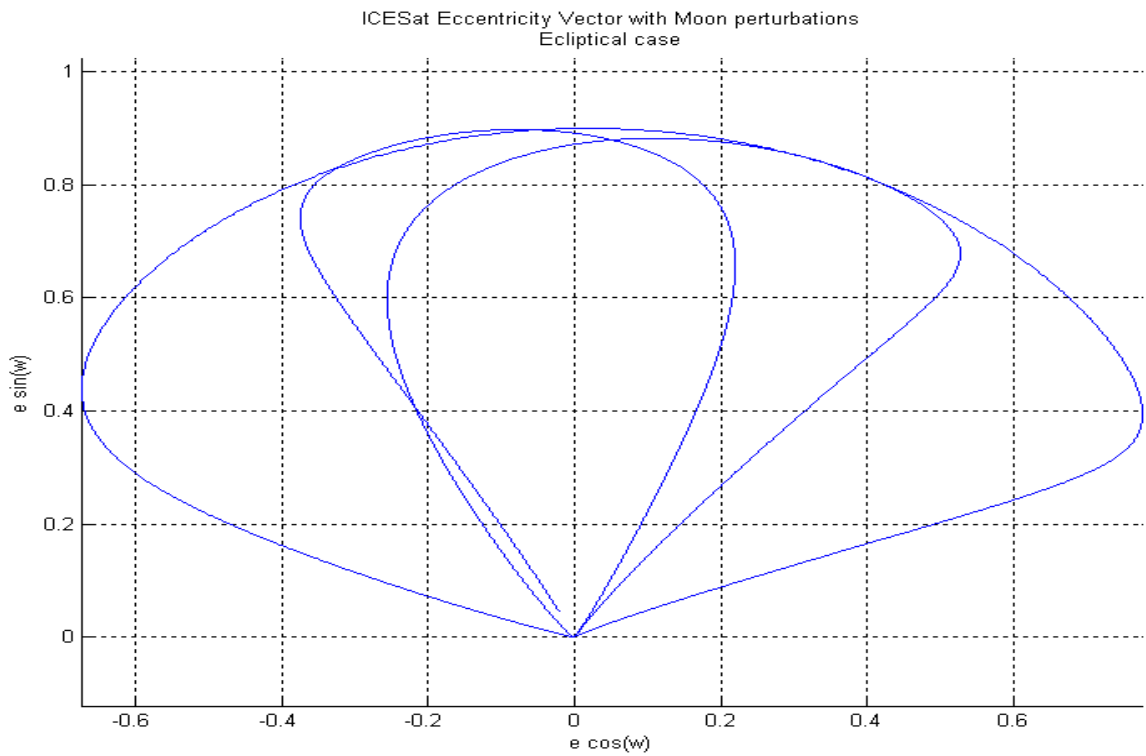


Figure 6.22: ICESat eccentricity vector due to the Moon over 10091 years with the Moon in the ecliptic plane.

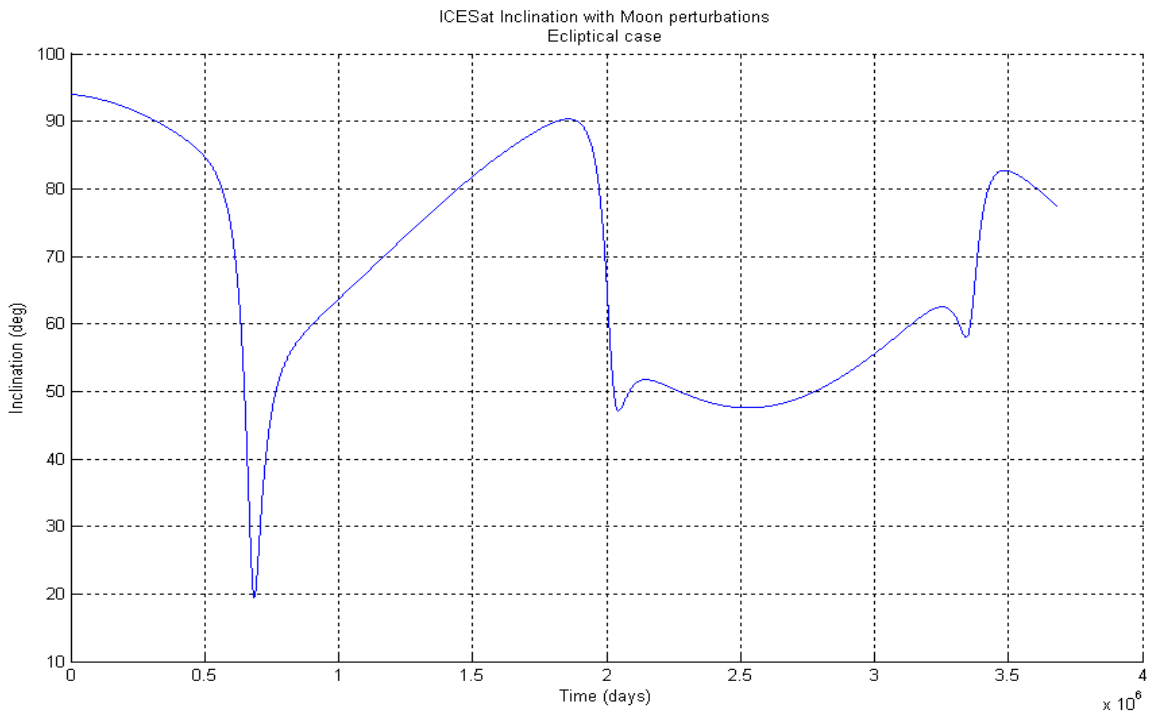


Figure 6.23: ICESat inclination due to the Moon over 10091 years with the Moon in the ecliptic plane.

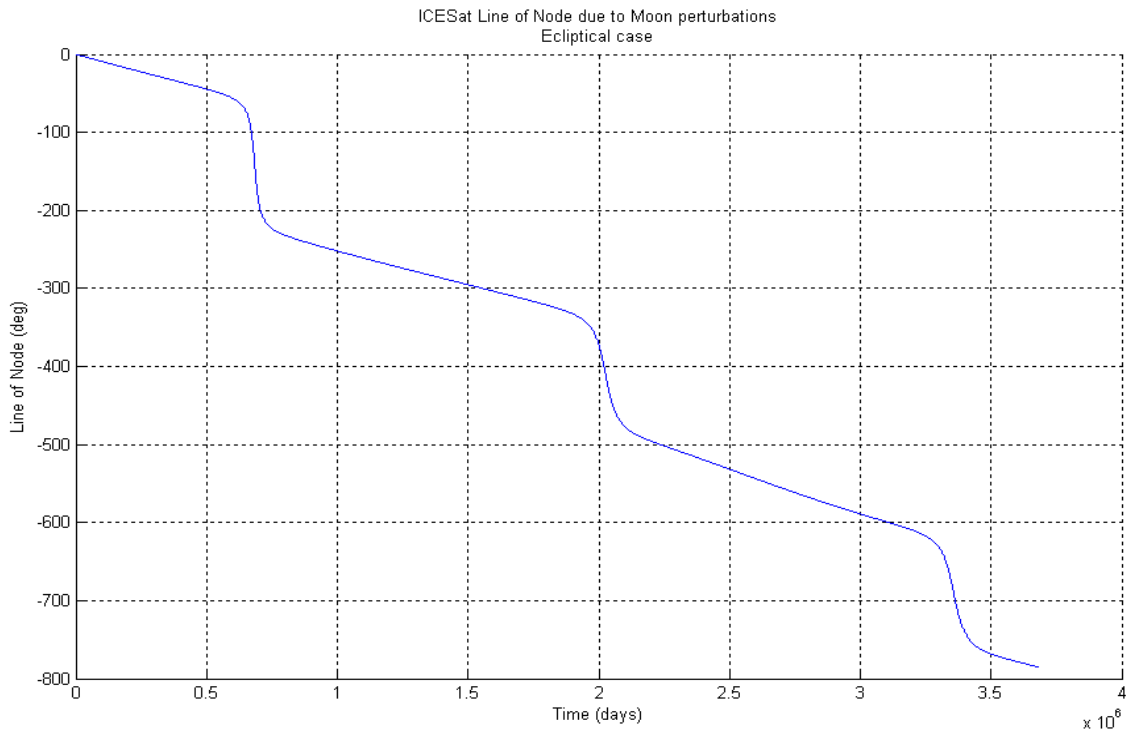


Figure 6.24: ICESat line of node due to the Moon over 10091 years with the Moon in the ecliptic plane.

For the purpose of the ICESat mission, it is necessary to look at the effect of the Sun and the Moon on the ICESat orbit for the real case of the third body orbiting (or apparently orbiting) in an inclined plane with respect to the Earth's equatorial plane using the single-average potential. We however maintain the other assumption that the third body motion, or apparent motion, around the Earth is circular. The propagation of ICESat's orbital elements is performed using the expansion to the 2nd degree of the single average disturbing function from Eq. (6.30). For each case, Sun and Moon, the propagation is performed twice: a first propagation over one period of the third body (365 days in the case of the Sun and 28 days in the case of the Moon); a second propagation over a longer time interval (5 years for the Sun and 365 days for the Moon) to demonstrate the more general trend of the evolution of the orbital elements. The initial conditions for the propagation are summarized in Table 6.2. The results of the longer propagations are compared to the ones obtained using the double-averaged potential given by Eq. (6.61). It can be observed that the eccentricity vector and the inclination still exhibit oscillations with period equal to half the period of the third body. The amplitude of the eccentricity vector is in the order of $3 \cdot 10^{-4}$ in the case of the Sun and in the order of $4 \cdot 10^{-8}$ in the case of the Moon. The drifts of the eccentricity vectors along the cosine direction are comparable to the ones obtained for the case the third body in the equatorial plane. The amplitudes of the oscillations for the inclinations are also comparable to the case of the third body in the equatorial plane. Therefore the amplitude of the inclination oscillations due to the Sun results in a groundtrack shift at the apex larger than the 800 meters tolerance. Furthermore in the case of the Moon, the inclination exhibits what

Orbital elements and epochs	ICESat	Moon	Sun
Semi-major axis	6970.238 km	$3.844 \cdot 10^{-5}$ km	$1.496 \cdot 10^{-8}$ km
Eccentricity	0.0013	0	0
Inclination	94°	23.45°	23.45°
Argument of Perigee	90°	0°	0°
Line of Node	0°	5.145°	0°
True Anomaly	N/A	0°	0°
t_0	N/A	0 sec	0 sec
t_{f1}	N/A	2432093.63 sec	31704077.63 sec
t_{f2}	N/A	31704077.63 sec	158520388.15 sec

Table 6.2: Initial conditions for the propagation of ICESat's orbital elements in the case of the third in an inclined plane.

appears to be a secular drift of $3.4 \cdot 10^{-6}$ degrees/day which leads to a secular groundtrack drift of 140 meters/year. Actually, by looking at Fig. (6.23) we see that it is not a secular drift but the long term effect of the third body in the inclined plane. Finally, the argument of the node also exhibits some small oscillations about a secular drift. Like the other orbital elements, the period of the oscillations of the node is equal to half the period of the third body. In addition, the slope of the drift in the case of the Moon is once again twice the slope of the drift in the case of the Sun: $-4.3 \cdot 10^{-5}$ degree/day for the Sun and $-8.9 \cdot 10^{-5}$ degree/day for the Moon. These drifts of the node correspond to groundtrack shifts at the equator of 1.75 km/year in the case of the Sun and 3.62 km/year in the case of the Moon.

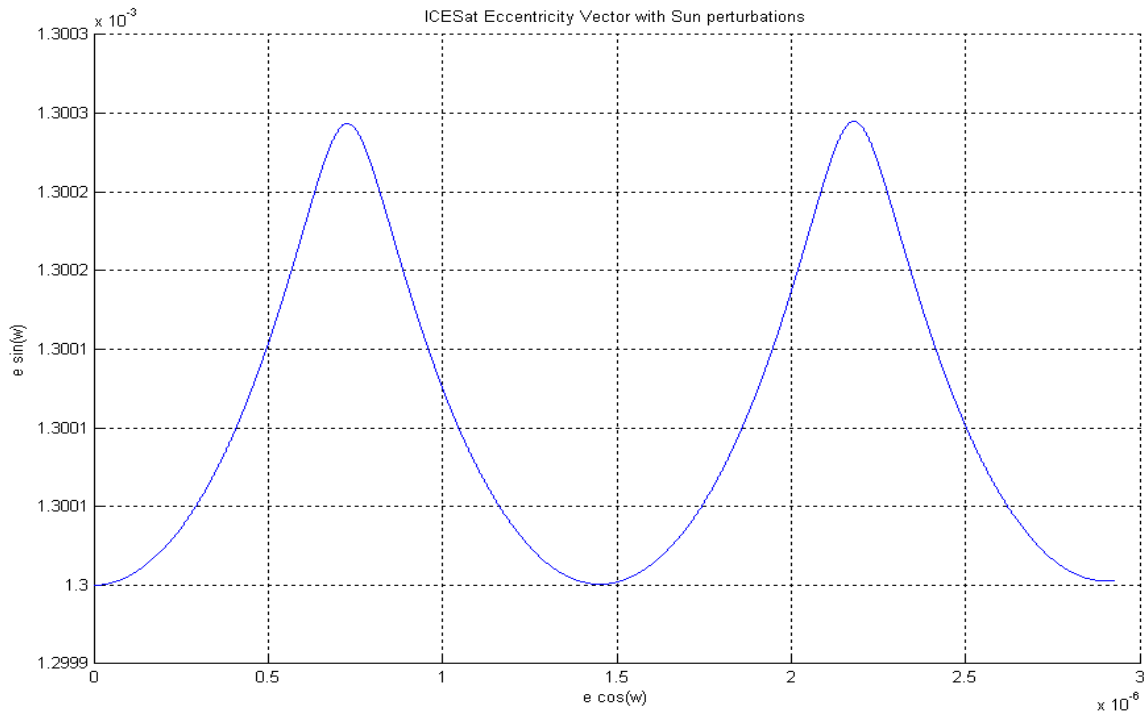


Figure 6.25: Perturbations of ICESat eccentricity vector due to the Sun over 365 days with the Sun in the ecliptic plane.

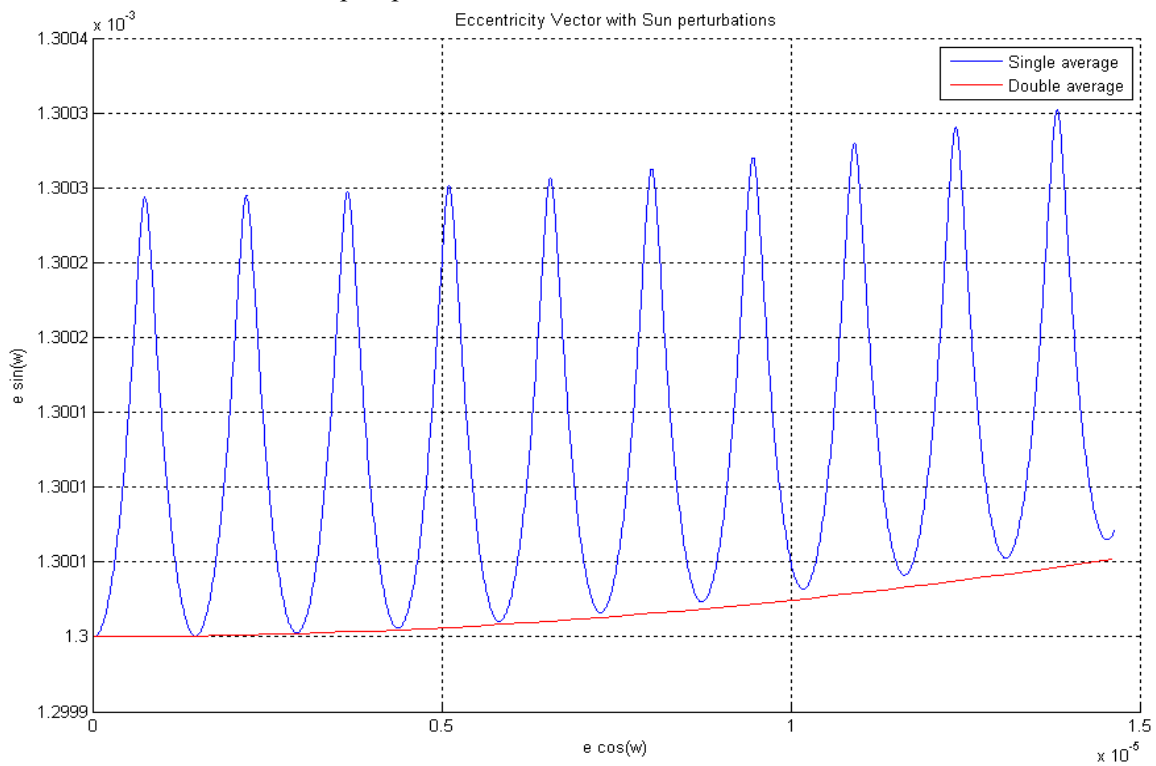


Figure 6.26: Perturbations of ICESat eccentricity vector due to the Sun over 5 years with the Sun in the ecliptic plane: comparison between single- and double-average potential.

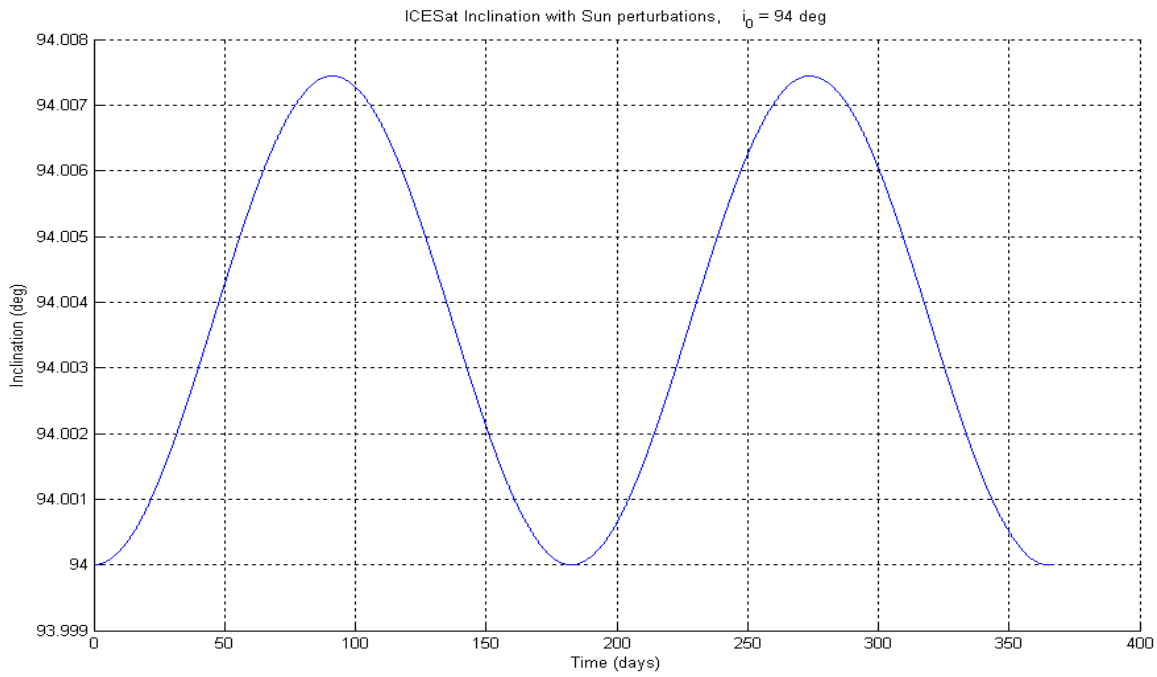


Figure 6.27: Perturbations of ICESat Inclination due to the Sun over 365 days with days with the Sun in the ecliptic plane.

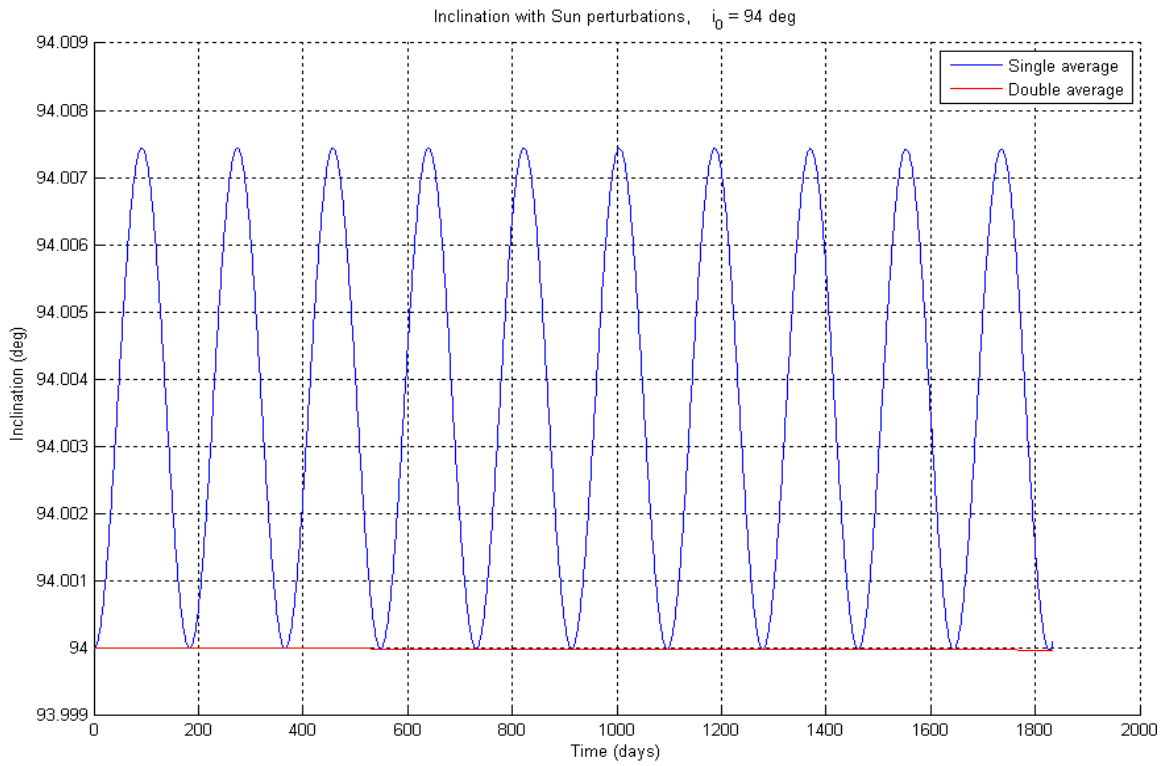


Figure 6.28: Perturbations of ICESat inclination due to the Sun over 5 years with the Sun in the ecliptic plane: comparison between single- and double-average potential.

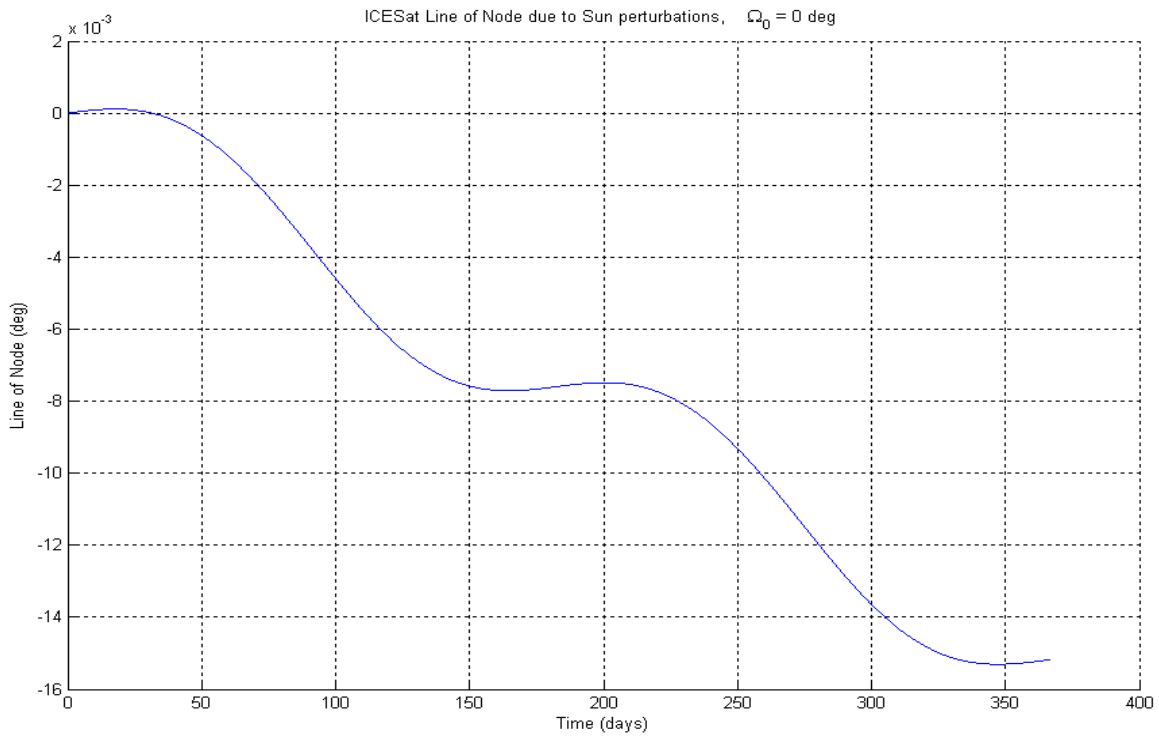


Figure 6.29: Perturbations of ICESat line of node due to the Sun over 365 days with the Sun in the ecliptic plane.

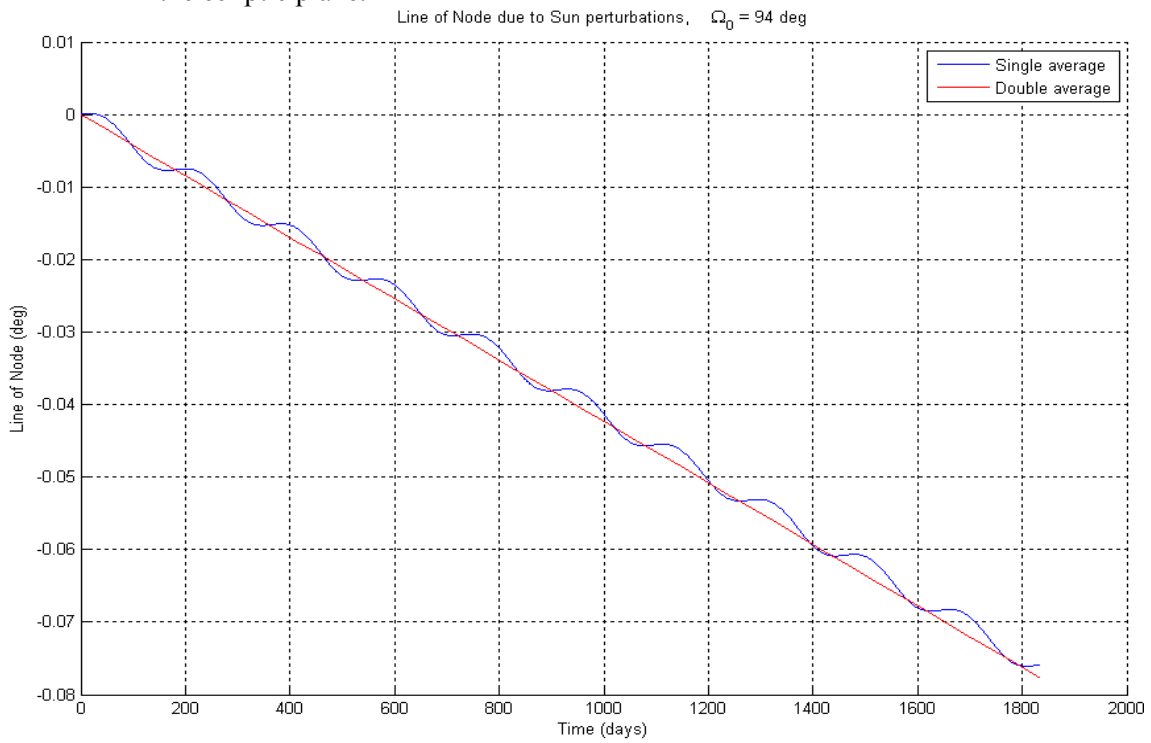


Figure 6.30: Perturbations of ICESat line of node due to the Sun over 5 years with the Sun in the ecliptic plane: comparison between single- and double-average potential.

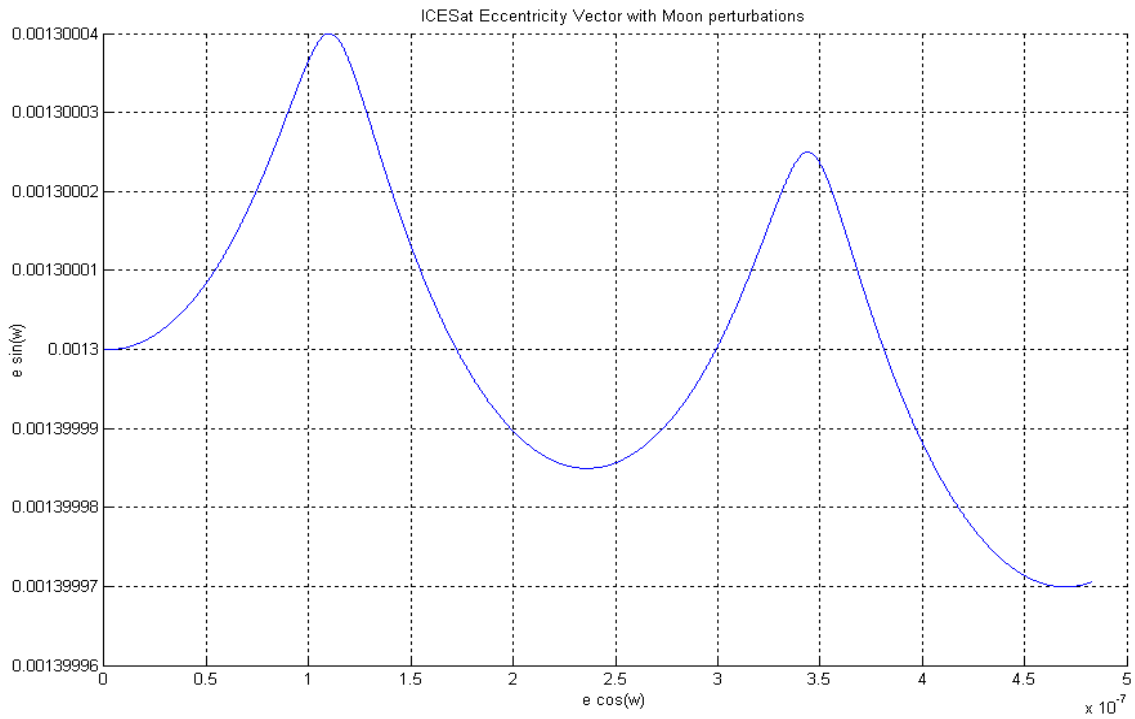


Figure 6.31: Perturbations of ICESat eccentricity vector due to the Moon over 28 days with the Moon in the ecliptic plane.

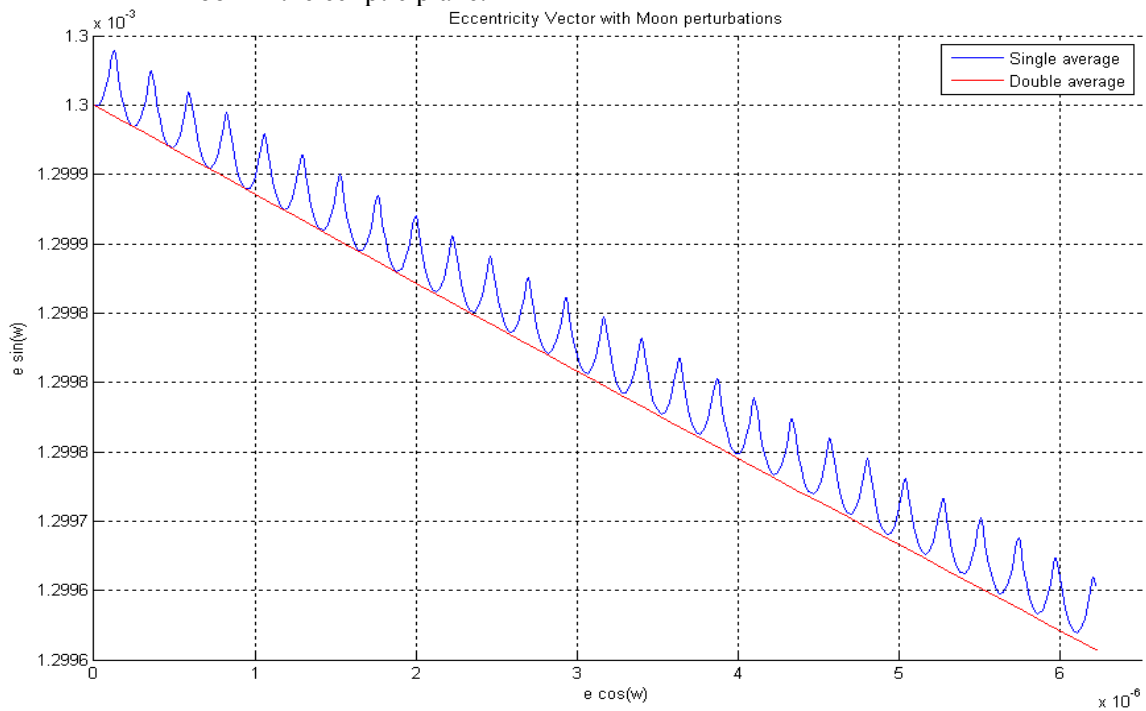


Figure 6.32: Perturbations of ICESat eccentricity vector due to the Moon over 365 days with the Moon in the ecliptic plane: comparison between single- and double-average potential.

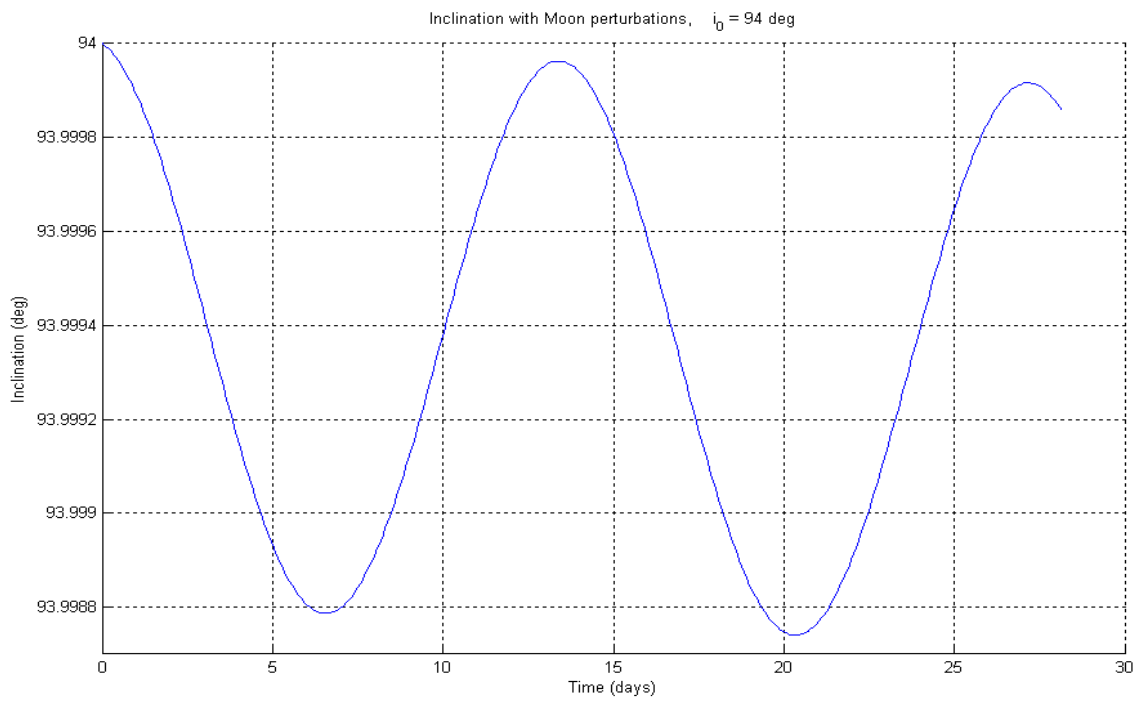


Figure 6.33: Perturbations of ICESat inclination due to the Moon over 28 days with days with the Moon in the ecliptic plane.

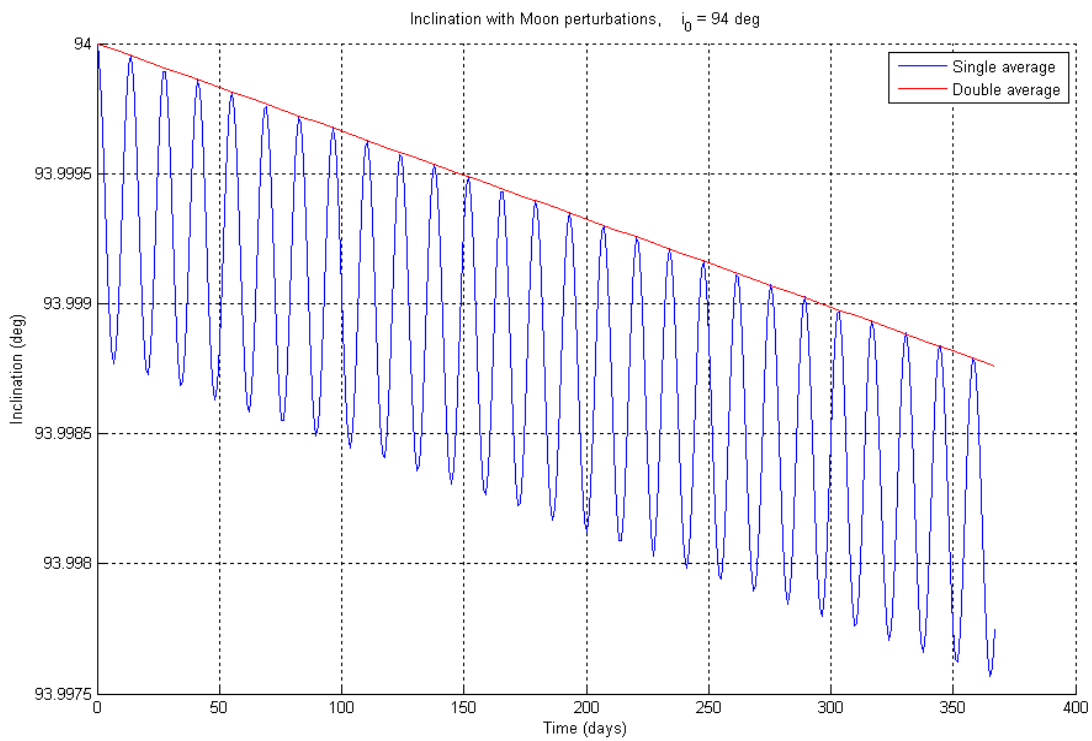


Figure 6.34: Perturbations of ICESat inclination due to the Moon over 365 days with the Moon in the ecliptic plane: comparison between single- and double-average potential.

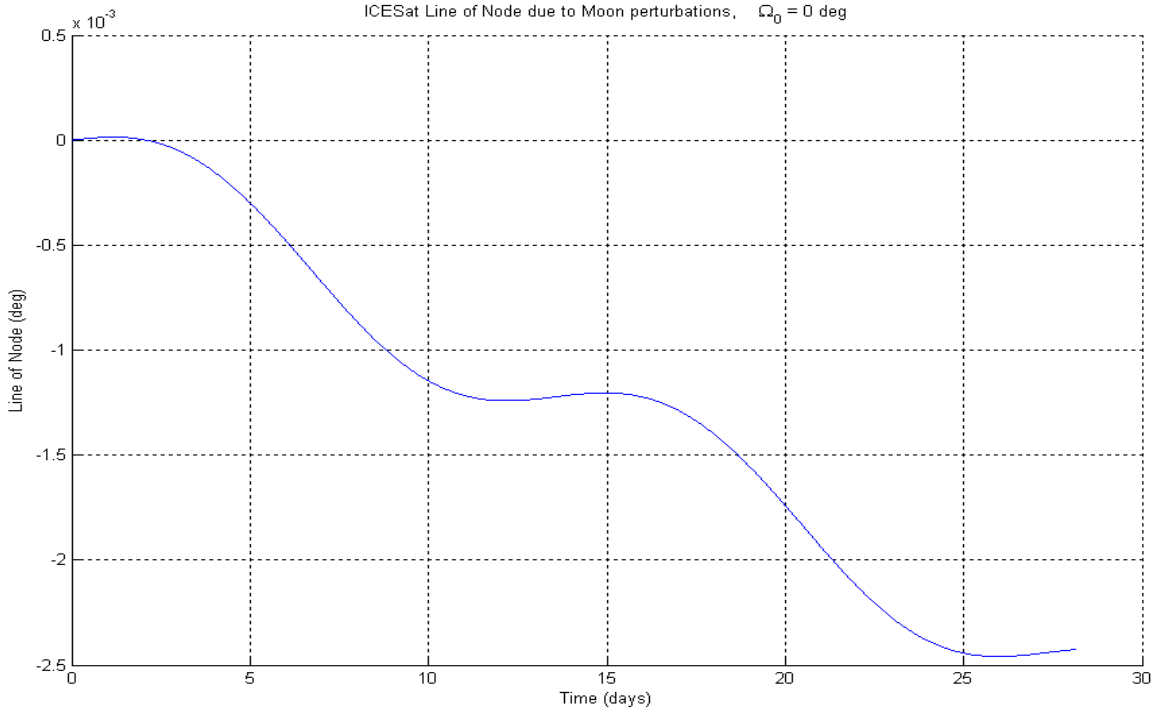


Figure 6.35: Perturbations of ICESat line of node due to the Moon over 28 days with the Moon in the ecliptic plane.

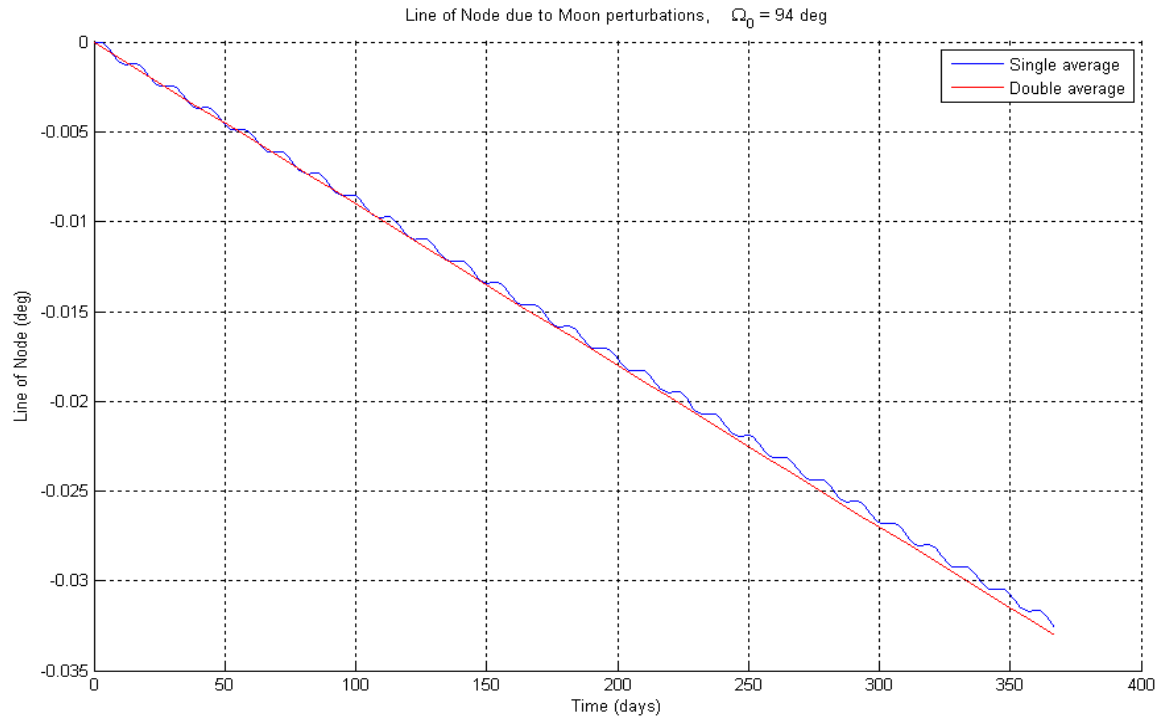


Figure 6.36: Perturbations of ICESat line of node due to the Moon over 365 days with the Moon in the ecliptic plane: comparison between single- and double-average potential.

6.6 APPLICATION TO REPEAT GROUNDTRACK ORBITS

In Chapter 2, we presented the method used at the Center for Space Research to design repeat groundtrack orbits. The repeat orbits generated for the ICESat mission are frozen in the average sense and therefore satisfy Eq. (2.9) to Eq.(2.11):

$$\dot{e} = 0 \quad (2.9)$$

$$\dot{\omega} = 0 \quad (2.10)$$

$$D \cdot \dot{M} + N \cdot (\dot{\Omega} - \omega_{\oplus}) = 0 \quad (2.11)$$

However, as we mentioned in Chapter 2, the force model used in the design of ICESat's repeat orbits is the geopotential expanded to degree 70 and order 70 (JGM3 for the 8-day and 183-day orbits, and GGM01 for the 91-day orbit). To avoid corrective orbital maneuvers on the ICESat satellite to compensate for the perturbation of the luni-solar effect, it would be interesting to include the single-average, or at least the double-average, third body disturbing function described in Eq. (6.30) and Eq. (6.61) in the methodology presented in the section 2.3.2 of Chapter 2. By including the third body effect, Eq. (2.9) to Eq. (2.11) become:

$$\dot{e}_{\bar{U}} + \dot{e}_{\bar{U}_s} + \dot{e}_{\bar{U}_M} = 0 \quad (6.63)$$

$$\dot{\omega}_{\bar{U}} + \dot{\omega}_{\bar{U}_s} + \dot{\omega}_{\bar{U}_M} = 0 \quad (6.64)$$

$$D \cdot (\dot{M}_{\bar{U}} + \dot{M}_{\bar{U}_s} + \dot{M}_{\bar{U}_M}) + N \cdot (\dot{\Omega}_{\bar{U}} + \dot{\Omega}_{\bar{U}_s} + \dot{\Omega}_{\bar{U}_M} - \omega_{\oplus}) = 0 \quad (6.65)$$

where the subscripts \bar{U} refer to the time rates given for the geopotential in Eq. (2.12) to Eq. (2.15), \bar{U}_S' to the time rate given for the double-average third body disturbing function corresponding to the Sun and subscripts \bar{U}_M' refer to the time rate given for the double-average third body disturbing function corresponding to the Moon.

Since the J_2+J_3 terms of the geopotential perturbations are dominant over the rest of the geopotential expansion and the third body perturbations, the argument of perigee value can be kept equal to $+\pi/2$ or $-\pi/2$ as it is done when only the geopotential is included in the force model. This value for the argument of perigee nullifies Eq. (2.21) from Chapter 2:

$$\dot{e} = \frac{3}{2} n \left(\frac{R_{\oplus}}{a} \right)^3 \frac{J_3}{(1-e^2)^2} \sin i \cos \omega \left(\frac{5}{4} \sin^2 i - 1 \right) \quad (2.21)$$

and by doing so, Eq. (6.63) is consider nullified also. The solutions for Eq. (6.64) and Eq. (6.65) can be obtained by a numerical iteration procedure similar to the one described in Chapter in Eq. (2.24), with the same initial for the eccentricity and the semi-major axis:

$$\begin{bmatrix} a \\ e \end{bmatrix}_{new} = \begin{bmatrix} a \\ e \end{bmatrix} - \left[\begin{array}{cc} \frac{\partial \dot{\omega}}{\partial a} & \frac{\partial \dot{\omega}}{\partial e} \\ D \frac{\partial \dot{M}}{\partial a} + N \frac{\partial \dot{\Omega}}{\partial a} & D \frac{\partial \dot{M}}{\partial e} + N \frac{\partial \dot{\Omega}}{\partial e} \end{array} \right]^{-1} \begin{bmatrix} \dot{\omega} \\ D \cdot \dot{M} + N \cdot (\dot{\Omega} - \omega_{\oplus}) \end{bmatrix} \quad (2.24)$$

To implement this procedure, it is necessary to develop the partial derivatives appearing in the Jacobian matrix:

$$\begin{aligned} \frac{\partial \dot{\omega}}{\partial a} = & \sum_{l=3}^{\infty} \sum_{m=0}^l \sum_{p=0}^l \sum_{k=0}^{\lfloor \frac{|l-2p|}{2} \rfloor} \sum_{p'=0}^l \left[K_{lm} T_{lpk} F_{lmp'}(i') \{c_{lmp} \cos \psi_{lmp'} + s_{lmp} \sin \psi_{lmp'}\} \cdot \right. \\ & \left. (l-2) \cdot \left(\frac{\sqrt{1-e^2}}{na^3 e} F_{lmp}(i) \frac{dI_{lpk}}{de} - \frac{\cos i}{na^3 \sqrt{1-e^2} \sin i} \frac{dF_{lmp}}{di} I_{lpk}(e) \right) \right] \end{aligned} \quad (6.66)$$

$$\begin{aligned} \frac{\partial \dot{\omega}}{\partial e} = & \sum_{l=2}^{\infty} \sum_{m=0}^l \sum_{p=0}^l \sum_{k=0}^{\lfloor \frac{|l-2p|}{2} \rfloor} \sum_{p'=0}^l \left[K_{lm} T_{lpk} F_{lmp'}(i') \{c_{lmp} \cos \psi_{lmp'} + s_{lmp} \sin \psi_{lmp'}\} \cdot \right. \\ & \frac{1}{na^2} \left((F_{lmp}(i)) \cdot \left(\frac{\sqrt{1-e^2}}{e} \frac{d^2 I_{lpk}}{de^2} - \frac{e^2 + \sqrt{1-e^2}}{e^2 \sqrt{1-e^2}} \frac{dI_{lpk}}{de} \right) \right. \\ & \left. \left. \frac{dF_{lmp}}{di} \cot i \cdot \left(-\frac{e}{(1-e^2)^{3/2}} I_{lpk}(e) - \frac{1}{\sqrt{1-e^2}} \frac{dI_{lpk}}{de} \right) \right) \right] \end{aligned} \quad (6.67)$$

$$\begin{aligned} \frac{\partial \dot{\Omega}}{\partial a} = & \frac{1}{na^3 \sqrt{1-e^2} \sin i} \sum_{l=3}^{\infty} \sum_{m=0}^l \sum_{p=0}^l \sum_{k=0}^{\lfloor \frac{|l-2p|}{2} \rfloor} \sum_{p'=0}^l \left[K_{lm} T_{lpk} F_{lmp'}(i') \frac{dF_{lmp}}{di} I_{lpk}(e) \cdot \right. \\ & \left. \{c_{lmp} \cos \psi_{lmp'} + s_{lmp} \sin \psi_{lmp'}\} \right] \end{aligned} \quad (6.68)$$

$$\begin{aligned} \frac{\partial \dot{\Omega}}{\partial e} = & \frac{1}{na^2 \sin i} \sum_{l=2}^{\infty} \sum_{m=0}^l \sum_{p=0}^l \sum_{k=0}^{\lfloor \frac{|l-2p|}{2} \rfloor} \sum_{p'=0}^l \left[K_{lm} T_{lpk} F_{lmp'}(i') \frac{dF_{lmp}}{di} \cdot \right. \\ & \left. \left(\sqrt{1-e^2} \frac{dI_{lpk}}{de} - \frac{e}{\sqrt{1-e^2}} I_{lpk}(e) \right) \cdot \{c_{lmp} \cos \psi_{lmp'} + s_{lmp} \sin \psi_{lmp'}\} \right] \end{aligned} \quad (6.69)$$

$$\frac{\partial \dot{M}}{\partial a} = -\frac{1-e^2}{na^3 e} \sum_{l=3}^{\infty} \sum_{m=0}^l \sum_{p=0}^l \sum_{k=0}^{\lfloor \frac{|l-2p|}{2} \rfloor} \sum_{p'=0}^l \left[K_{lm} T_{lpk} F_{lmp'}(i') F_{lmp}(i) \frac{dI_{lpk}}{de} \cdot \left\{ c_{lmp} \cos \psi_{lmp'} + s_{lmp} \sin \psi_{lmp'} \right\} \right] \quad (6.70)$$

$$\frac{\partial \dot{M}}{\partial e} = \frac{1}{na^2} \sum_{l=2}^{\infty} \sum_{m=0}^l \sum_{p=0}^l \sum_{k=0}^{\lfloor \frac{|l-2p|}{2} \rfloor} \sum_{p'=0}^l \left[K_{lm} T_{lpk} F_{lmp'}(i') F_{lmp}(i) \cdot \left(\frac{1+e^2}{e^2} \frac{dI_{lpk}}{de} - \frac{1-e^2}{e} \frac{d^2 I_{lpk}}{de^2} \right) \cdot \left\{ c_{lmp} \cos \psi_{lmp'} + s_{lmp} \sin \psi_{lmp'} \right\} \right] \quad (6.71)$$

At this point, all the terms necessary to modified the procedure established by Lim (1995) in order to include the third body effect in the design of repeat groundtrack orbits are in place. At the end of the iteration described in Eq. (2.24), the values obtained for the orbital elements are the mean values that satisfy the frozen condition in the average sense and the repeat groundtrack condition simultaneously. As described in Chapter 2, the next step consists of getting the initial osculating orbital elements by including the short period oscillations of the non-averaged potential. For the third body effect however, the short period oscillations that disappear during the averaging can still be neglected. Consequently, the second part of Lim's procedure to get the osculating orbital elements remains unchanged.

CHAPTER 7

CONCLUSIONS

Tough the ICESat mission is not the not the first satellite mission to make use of repeat groundtrack orbits to achieve its mission purposes, ICESat increased the understanding of the repeat groundtrack orbits dynamics and characteristics. From the generation of the repeat orbits in a 70x70 geopotential using state of the art Grace Gravity Model to the intensive use of the ICESat orbit's subcycles as a partial remedy to the initial in flight laser failure, the ICESat mission has provided valuable insights on a type of orbits commonly chosen for Earth observation satellite mission. The high agility of the ICESat satellite enables the off-nadir pointing to close-by tracks, whether they belong to ICESat own repeat groundtrack or the repeat groundtrack from another orbit with different inclination and semi-major axis. ICESat off-nadir capacity prompted a thorough analysis of crossover locations between two distinct repeat groundtrack orbits.

7.1 SUBCYCLES

Based on the framework developed by Lim (1995) and the concept of near-repeat track, a general definition of repeat track subcycles was given and illustrated with the three repeat orbits designed for the ICESat mission. The chart of subcycles was introduced as a tool to visualize the entire range of subcycles for one specific orbit, giving information on both the duration and the groundtrack offset for each subcycle. The geometrical properties of these charts were used to explain the decomposition of the ICESat repeat cycle into the sequence of three main subcycles of 25, 33 and 25 nodal days. The Bezout theorem was presented to explain the underlying mathematical concept behind the distribution pattern of the subcycles on the chart. The charts of subcycle along with the Bezout theorem are presented as a valuable tool for the design of repeat groundtrack orbits.

7.2 PHASING

The concept of a phasing maneuver as it was developed for the ICESat mission was presented along with its correlation with the ICESat's subcycle. The design of the phasing maneuvers which, in the case of ICESat, consist in transferring back and forth between 91-day repeat orbit and the 8-day repeat orbit relies on two key elements: the transition orbits and the transition opportunities. The direct link between the possible transition orbits and the subcycle of the 91-day repeat orbit was illustrated by comparing the resonance map of repeat orbits to the chart of subcycle. Furthermore, the number of

transition opportunities for any possible transition repeat orbit was shown to be related to the groundtrack offset of the corresponding subcycle. The phasing maneuver proves to be a fuel efficient approach to reposition the ICESat satellite above a different segment of the 91-day repeat groundtrack.

7.3 CROSSOVERS

The off-nadir pointing capacity of the ICESat satellite make it a very attractive cross-validation option for other mission flying in repeat groundtrack orbits with near polar inclination. A numerical procedure to find the location of crossovers was developed based on the geometry of two tracks belonging to two distinct Keplerian orbits. This procedure was applied to the case of ICESat vs. CryoSat in order to find the crossover locations between the two repeat groundtrack at latitude 70°N . The same procedure was applied to find the crossover locations between ICESat and ENVISAT with latitudes in the vicinity of 70°N . Through the example of ICESat vs. ICESat-II, in the hypothetical case of ICESat-II being placed into a 91-day repeat orbit with 1376 satellite revolution, it was shown that the off-nadir pointing around crossover location was not a suitable approach for cross-validation between two orbits with close orbital period and identical inclination. In that case, an approach similar to the Targets Of Opportunities (TOO) should be preferred.

7.4 THIRD BODY PERTUBATIONS

The perturbations due to the third, whether it is the Moon or the Sun, affect the orbital elements of the ICESat satellite, and more specifically the argument of the node. The perturbations on the node have a direct effect on the repeat characteristic of the ICESat groundtrack. Therefore, it would be interesting to include the third body perturbation in the force model used in the design of the repeat groundtrack orbits. As a preliminary work towards this goal, the close-forms of the orbital elements time derivatives, which accounts for the third body perturbations, are given. Starting from the expansion of the third body disturbing function expansion using the Legendre polynomials, a new close form of the single-average potential was presented using the Chebychev polynomials. This single-average disturbing function was used in the Lagrangian Planetary Equations to illustrate the effect of the Sun and the Moon separately on ICESat orbital elements. A comparison between hypothetical equatorial cases (with the third body orbiting in the Earth's equatorial plane) and the ecliptic case showed the non-negligible effect of the ecliptic on the evolution of the orbital elements. Finally, the close form derivatives necessary to include the third body effect in the frozen repeat groundtrack orbit analysis were established using the single-average disturbing function. The numerical results obtained with this new expansion of the potential were successfully compared the double-average disturbing function more commonly found in the literature. However, the equation of motions and their applications to ICESat require a thorough validation.

7.5 FUTURE WORK

Though the phasing orbit concept and its direct link to the repeat orbit subcycle seems well-understood in the light of our study, more theoretical work would be necessary to completely validate our findings beyond any doubt. A theoretical framework could possibly provide numerical tools to convert directly the well-known resonance map (Klokočník, 2003) for repeat orbits into chart of subcycles.

The crossover study is based on the geometry of Keplerian orbits. A much needed improvement to the study would be to work with more realistic orbits. Also in order to improve the reliability of the results a method to check for the total number of existing crossover location at inside a specific latitude range should be implemented.

Finally, the study on the third body effect was presented as a preliminary work towards the improvement of the repeat groundtrack orbit design. A future effort should be made to validate the numerical results presented for the case of ICESat. Upon validation, the procedure developed by Lim (1995) should be modified to include the new terms due to the third body effect. The ultimate goal will be to obtain a new set of initial osculating orbital elements for a new design of ICESat repeat orbit that would include the third body effect into the force model.

Bibliography

- [1] ALBEE, A., ARVIDSON, R., PALLUCONI, F., THORPE, T. “Overview of the Mars Global Surveyor Mission,” *Journal of Geophysical Research*, Vol.106, No. E10, pp.23291-23316.
- [2] BENVENISTE, J, “Strategy for ENVISAT Radar Altimetry Cross-Calibration and Validation”, Geoscience and Remote Sensing Symposium Proceedings (IGARSS), Vol. 6, pp. 2730-2732, 2000.
- [3] BHAT, R. S., et al., “TOPEX/POSEIDON Orbit Maintenance Maneuver Design”, *Advances in Astronautical Sciences*, Vol. 71, Pt. 1, pp 645-670, 1989
- [4] BORN, G. H., et al., “GEOSAT-ERM – Mission Design”, *The Journal of the Astronautical Sciences*, Vol.35, no. 2, pp 119-134, April-June 1987.
- [5] BORN, G. H., et al., “Orbit Analysis for the GEOSAT-ERM”, *The Journal of the Astronautical Sciences*, Vol.36, no. 4, pp 425-446, October-December 1988.
- [6] BROUCKE, R. A., “Long-Term Third-Body Effects via Double Averaging”, *Journal of Guidance, Control, and Dynamics*, Vol. 26, no. 1, January-February 2003.
- [7] COFFEY, S., DEPRIT, A. and DEPRIT, E. “Frozen Orbits for Satellites Close to an Earth-like Planet,” *Celestial Mechanics and Dynamical Astronomy*, Vol. 59, No. 1, pp. 37-72, 1994.
- [8] CryoSat Mission Overview, ESA document, BR-199, April 2003.
- [9] CUTTING, E., et al., “Orbit Analysis for SEASAT-A”, *The Journal of the Astronautical Sciences*, Vol.26, no. 4, pp 315-342, October-December 1978.
- [10] DELHAISE, F., “The Effects of Luni-Solar Gravitation and solar Radiation Pressure on the Molniya and Tundra Orbits”, European Space Operations Center – Mission Analysis Section, MAS Working Paper no. 295, March 1989.
- [11] EVEREST, G. and WARD, T. *An Introduction to Number Theory*, Springer-Verlag, London Limited, 2005.

- [12] FARLESS, D. L., "The Application of Periodic Orbits to TOPEX Mission Design," *Advances in the Astronautical Sciences*, Vol. 58, No. 1, pp. 13-36, AAS85-301.
- [13] FOLTA, D. and QUINN, D., "Lunar Frozen Orbits", AAS/AIAA Astrodynamics Specialist Conference, Keystone, CO, AIAA 2006-6749, 2006.
- [14] GIACAGLIA, G. E. O., "The Equations of Motion of an Artificial Satellite in Non-Singular Variables", *Celestial Mechanics*, Vol. 15, pp 191-215, 1977.
- [15] GIACAGLIA, G. E. O. and PRADO, A. F. B. A., *Third Body Perturbations on Satellites*, São José dos Campos: INPE, 2003.
- [16] KAULA, W. M., "Development of the Lunar and Solar Disturbing Function for a Close Satellite", *Astronomical Journal*, Vol. 67, no. 2, pp 300-303, June 1962.
- [17] KAULA, W. M., *Theory of Satellite Geodesy: applications of satellites to geodesy*, Dover ed, 1966.
- [18] KIM, M. C., "Theory of Satellite Ground-Track Crossovers", *Journal of Geodesy*, Vol. 71, 1997.
- [19] KING, J. C. "Quantization and Symmetry in Periodic Coverage Patterns with Applications to Earth Observation," *Journal of the Astronautical Sciences*, Vol. 24, No. 4, pp. 347-363, Oct-Dec 1976.
- [20] KLOKOCNIK, J., et al., "On Fine Selection for Particular Geodetic and Oceanographic Missions Involving Passage Through Resonances", *Journal of Geodesy*, Vol. 77, pp 30-40, 2003.
- [21] LARA, M. "On Periodic Polar Orbits of the Artificial Satellite Problem," *Journal of the Astronautical Sciences*, Vol. 45, No. 3, pp. 321-328, 1997.
- [22] LARA, M., *SADSaM: a Software Assistant for Designing Satellite Missions*, Report for the C.N.E.S., April 1999.
- [23] LARA, M., "Searching for Repeating Ground Track Orbits: A Systematic Approach," *Journal of the Astronautical Sciences*, Vol. 47, pp. 177-188, 1999.
- [24] LIM, S., *Orbit Analysis and Maneuver design for the Geoscience Laser Altimeter System*, Ph.D. dissertation, The University of Texas at Austin, December 1995.
- [25] LIM, S. and SCHUTZ, B. E., "Repeat Ground Track Analysis for the Geoscience Laser Altimeter System," *AAS/AIAA Spaceflight Mechanics Meeting*, AAS96-205, Austin, Texas, February 1996.

- [26] MORANDO, B., “Etude des Perturbations Luni-Solaires sur un Satellite de 24 Heures”, *Bulletin Astronomique*, 1966, pp 257–264.
- [27] PRADO, A. F. B. A., “Third-Body Perturbation in Orbits Around Natural Satellites”, *Journal of Guidance, Control, and Dynamics*, Vol. 26, no. 1, January-February 2003.
- [28] REES, W. G., “Orbital Subcycles for Earth Remote Sensing satellites”, *International Journal of Remote Sensing*, Vol.13, no. 5, pp 825-833, 1992.
- [29] “Report from the ICESat-II Workshop”, Linthicum Maryland, sponsored by NASA, June 27-29, 2007.
- [30] RIM, H. J.,SCHUTZ, B. E.,WEBB, C. E. and DEMAREST, P., “Repeat Orbit Characteristics and Maneuver Strategy for a Synthetic Aperture Radar satellite,” *Journal of Spacecraft and Rockets*, Vol. 37, No. 5, pp. 638-644, Sept.-Oct. 2000.
- [31] ROSBOROUGH, G. W. and OCAMPO, C. A., “Influence of Higher Degree Zonals on the Frozen Orbit Geometry,” *AAS/AIAA Spaceflight Mechanics Meeting*, AAS91-428, 1991.
- [32] SCHUTZ, B. E., et al., “Overview of the ICESat Mission”, *Geophysical Research Letters*, Vol. 32, L21S01, 2005.
- [33] SOLORZANO, C. R. and PRADO, A. F. B. A., “Third-Body Perturbation Using a Single Averaged Model”, *Advances in Space Dynamics 4: Celestial Mechanics and Astronautics*, pp 47-56, 2004
- [34] UPHOFF, C. and REDDEN, G., “Orbit Selection for the Radarsat Exact Repeat Groundtrack,” *Advances in the Astronautical Sciences*, Vol. 79, No. 2, pp. 765-782, AAS92-142, 1992.
- [35] VALLADO, D. A., *Fundamentals of Astrodynamics and Applications*, 1997.
- [36] WEBB, C. personal communication.
- [37] WEBB, C. E., et al., “ICESat Off-Nadir Laser targeting: Theory and Practice”, *Advances in the Astronautical Sciences*, Vol. 123, Pt. 1., pp 155-174, 2006.
- [38] WINGHAM, D. J., et al., “CryoSat: A mission to determine the fluctuations in Earth’s land and marine ice fields”, *Advances in Space Research*, Vol. 37, no. 4, pp 841-871, 2006.

Vita

Nadège Pie was born in Bruxelles, Belgium on July 21, 1977, daughter of Monique Nurenberg-Pie and Bertrand Pie. After graduating from the *Lycée S^t Marc* (Lyon, France) in June 1995, she entered the *Classes Préparatoires Aux Grandes Ecoles: Aux Lazaristes* (Lyon, France) in September 1995. After passing the nationwide admission exam *Concours Aux Grandes Ecoles* in May-July 1998 she entered the prestigious *Ecole Centrale de Lille* (Lille, France) in September 1998 from which she graduated with a *Diplôme d'Ingénieur*. In August 2000 she entered the University of Texas at Austin and obtained her Master of Science in Aerospace Engineering in May 2002 working on orbital maneuvers for the GRACE mission under the supervision of Dr. Byron D. Tapley . In January 2003, she started working with Dr. Bob E. Schutz towards the completion of her Ph.D. in Aerospace Engineering.

Permanent Address: 63 rue de l'Abondance
69003 Lyon
FRANCE

This dissertation was typed by the author.